Hall A Status Report - 2006

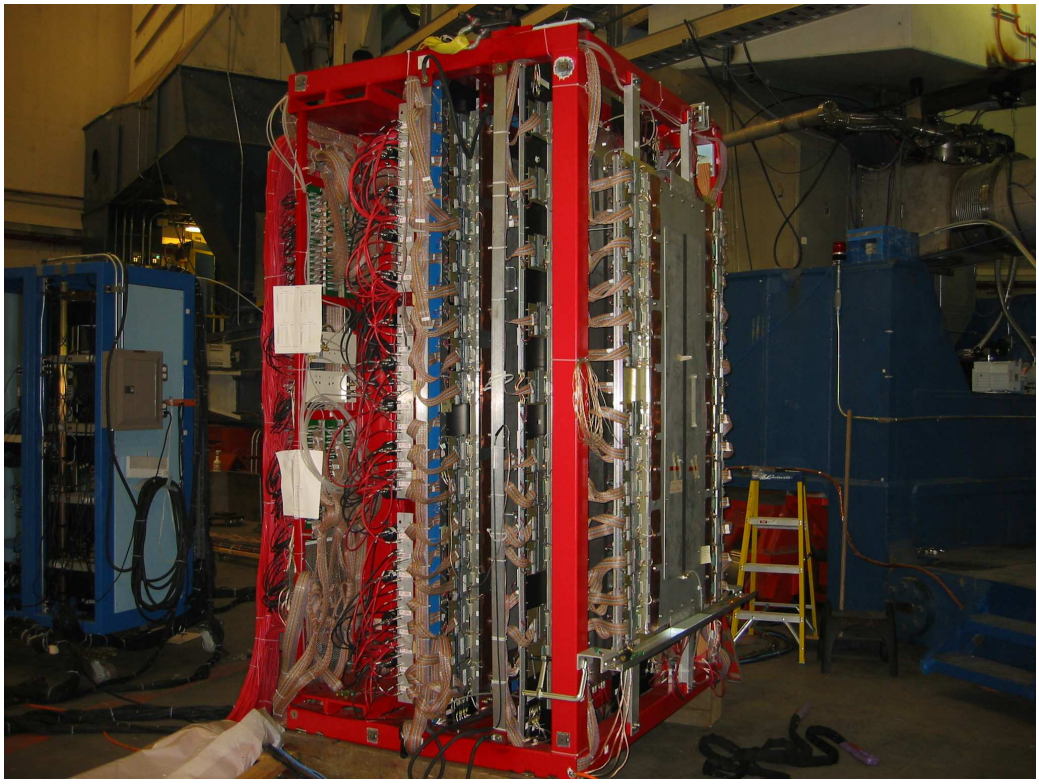

Edited by John Arrington, Kees de Jager and Xiaodong Jiang

February 2007

Contents

1 Introduction **8**
1.1 Introduction . . . 8

2 Standard Hall A Facilities **10**
2.1 The Hall A Compton Polarimeter . . . 10
2.1.1 Overview . . . 10
2.1.2 Recent Data . . . 10
2.1.3 Green Laser Upgrade . . . 10
2.1.4 Fabry-Perot Cavity . . . 12
2.1.5 Detector Upgrade . . . 13
2.2 Large wire chambers for the BigBite spectrometer . . . 16
2.2.1 Introduction . . . 16
2.2.2 Chamber operation . . . 18
2.3 Beam Calorimeter . . . 22
2.4 Data Analysis . . . 24

3 Summaries of Experimental Activities **26**
3.1 E94-107 . . . 26
3.1.1 Present status and outlook . . . 26
3.1.2 High-Resolution Spectroscopy of ${}^{12}_{\Lambda}$B by Electroproduction 26
3.1.3 ^{16}O$(e,\, e'$K$^+)^{16}_{\Lambda}$N and H$(e, e' K^+)\Lambda$ reactions . . . 28
3.1.4 RICH detector upgrade . . . 30
3.1.5 Conclusion . . . 31
3.2 E97-110 . . . 33
3.2.1 The experiment . . . 33
3.2.2 Present state and outlook . . . 33
3.3 E99-114 . . . 36
3.3.1 Introduction . . . 36
3.3.2 Experiment . . . 36
3.3.3 Analysis . . . 37
3.3.4 Results . . . 39
3.4 E99-115 and E00-114 . . . 43
3.4.1 Introduction . . . 43
3.4.2 Motivation . . . 43
3.4.3 Experimental Issues and Progress . . . 44
3.4.4 Results for G_E^s and G_M^s . . . 45
3.4.5 Summary and Outlook . . . 48
3.5 E00-007 . . . 49
3.6 E00-102 . . . 52
3.7 E00-110 . . . 57
3.7.1 Deeply Virtual Compton Scattering Experiment . . . 57

3.7.2 GPDs and the DVCS Cross Sections 59
3.7.3 Simulation and Analysis 60
3.7.4 DVCS Results 60
3.7.5 Deeply Virtual π^0 Production 62
3.8 E01-012 63
3.9 E01-015 67
3.10 E02-013 69
3.10.1 Introduction 69
3.10.2 Experiment overview 70
3.10.3 Experimental run 74
3.10.4 Current status of data analysis 75
3.11 E03-104 81
3.12 E03-106 85
3.13 E04-012 88
3.13.1 Introduction 88
3.13.2 Experiment 88
3.13.3 Analysis 90
3.14 E05-004 and E05-103 95

4 References **98**

5 Hall A Collaboration Member List **102**

6 Publications **109**

7 Theses **110**

List of Figures

1 Schematic layout of the Hall A Compton polarimeter. 10
2 Preliminary beam polarization data taken for the G_E^n (E02-013) experiment 11
3 Optics table of the green Compton polarimeter. 12
4 Green Fabry-Perot cavity under test in the Compton Polarimetry Lab. 13
5 Characteristic signals of the new cavity: reflected power, PDH Error signal, and transmitted power trace. 14
6 The new electron detector housing and vacuum chamber design completed by LPC-Clermont. 15
7 A large BigBite wire chamber in the clean room at UVa. 17
8 The electrode configuration of the front and the back chambers. . . 18
9 The detector package with the three MWDCs in Hall A is shown ready for installation in the BigBite spectrometer. 19
10 The wire-hit histograms for the front and the middle chambers in a typical run during the G_E^n experiment. 20
11 Residual histograms for the X1 plane indicating a per-plane position resolution of $\sigma \approx 300$ μm. 21
12 Mechanical drawing of the beam calorimeter. 22
13 E94-107: ${}^{12}_{\Lambda}$B excitation-energy spectrum after PID cuts 27
14 E94-107: ${}^{12}_{\Lambda}$B excitation-energy spectrum with fits and theoretical curves for the bound states 28
15 E94-107: Preliminary data for the ${}^{16}_{\Lambda}$N missing-energy spectrum. . 29
16 E94-107: Preliminary data for the $p(e, e'\mathrm{K}^+)\Lambda$ measured on the waterfall target. 30
17 E94-107: Upgraded RICH simulated event and expected performance 31
18 E94-107: Upgraded RICH simulated performance 32
19 E97-110: Preliminary Carbon elastic cross section. In red: simulation. black symbols: experimental data 34
20 E97-110: Preliminary inelastic asymmetries for 9° scattering angle and beam energy of 2.23 GeV 35
21 E99-114: Schematic layout of the RCS experiment. 37
22 E99-114: Kinematic correlations of the photon-proton events for the kinematics $s = 6.79$, $-t = 3.04$ GeV^2. 38
23 E99-114: Distribution of δx, with a coplanarity cut $\mid \delta y \mid \leq 15$ cm, with the RCS and ep events indicated. 39
24 E99-114: Energy distribution in the calorimeter for events with $|\delta y| \leq 15$ cm and $\mid \delta x \mid \leq 8$ cm. 40
25 E99-114: Cross section of the RCS process vs. transferred momentum t at three values of s. 41
26 E99-114: Scaling of the RCS cross section at fixed θ_{cm}. 42

27 E99-114: Extracted RCS form factor R_V. 42
28 E99-115: "Parity quality" beam. 46
29 E99-115: HAPPEx constraints on strangeness form factors. 47
30 E00-007: Angular distributions for all three recoil proton polarization components in deuteron photodisintegration. 49
31 E00-102: Projected A_{LT} data compared to E89-003 results and calculations of Udias *et al.* 53
32 E00-102: E00-102 kinematics. 53
33 E00-102: E00-102 waterfall target 54
34 E00-102: Coincidence-time spectra from the Root/C++ analyzer before and after the construction of the specialized E00-012 coincidence timing code. 55
35 E00-102: Selected results from the Lund/Madrid MCEEP simulations. 56
36 E00-110: Lowest-order QED diagrams for the process $ep \to ep\gamma$, including the DVCS and Bethe-Heitler (BH) amplitudes 58
37 E00-110: Missing mass squared for $\mathrm{H}(e, e'\gamma)X$ events 58
38 E00-110: Data and fit to $d^4\Sigma/dQ^2dx_{\mathrm{Bj}}dtd\phi_{\gamma\gamma}$, and $d^4\sigma/(dQ^2dx_{\mathrm{Bj}}dtd\phi_{\gamma\gamma})$, as a function of $\phi_{\gamma\gamma}$. 61
39 E00-110: Q^2 dependence of $\Im$m parts of (twist-2) $\mathcal{C}^{\mathcal{I}}(\mathcal{F})$ and (twist-3) $\mathcal{C}^{\mathcal{I}}(\mathcal{F}^{\mathrm{eff}})$ angular harmonics, averaged over t 62
40 E01-012: The spin structure function $g_1^{^3\mathrm{He}}$ in the resonance region at Q^2 of 1.2, 1.9, 2.6 and 3.3 GeV^2. 64
41 E01-012: $\tilde{\Gamma}_1^{^3\mathrm{He}}$: test of spin duality on ^{3}He. 65
42 E01-012: Same as in Fig. 41 but for $\tilde{\Gamma}_1^n$. 65
43 E01-012: $A_1^{^3\mathrm{He}}$ in the resonance region. 66
44 E01-015: Computer-aided design (CAD) drawing of the SRC experimental setup. 67
45 E01-015: Measured and extrapolated ratios of yields for the $^{12}\mathrm{C}(e, e'pp)$ and the $^{12}\mathrm{C}(e.e'p)$ reactions. 68
46 E02-013: A schematic view of the E02-013 experiment. 71
47 E02-013: Top view on the BigBite spectrometer and the downstream part of the target. 72
48 E02-013: A view of the BigHAND detector during preparation for moving it to the next kinematic point. 73
49 E02-013: Target polarization during the E02-013 experiment. . . . 74
50 E02-013: Selected world data on G_E^n with the values of Q^2 in E02-013 and expected accuracy of Hall A results. 75
51 E02-013: The target coordinate reconstruction for the optics target. 76
52 E02-013: The electron momentum vs. scattering angle in BigBite. 77
53 E02-013: The energy in the shower detector vs. electron momentum. 78
54 E02-013: The energy deposition in the pre-shower layer showing a clear separation between the pion peak and the electron peak. . . . 78

55 E02-013: The raw time spectra between trigger signals of two arms. 79
56 E02-013: The time-of-flight spectra for electron-neutron events. The peak located 4 ns left of the neutron peak is due to prompt photons. 79
57 E02-013: Distribution of the electron-proton and electron-neutron events for the W vs. the missing momentum parallel to the momentum transfer 80
58 E02-013: Distribution of the electron-neutron events for W vs. the missing momentum perpendicular to the momentum transfer and the P_{per} distributions for the selected intervals of W with the level of accidental events 80
59 E03-104: Existing data from Mainz and JLab along with anticipated uncertainties from experiment E03-104. 82
60 E03-104: The ratio $\mu_P G_{E_p}/G_{M_p}$ from previous recoil-polarimeter experiments including E93-049 and E03-104 data. 83
61 E03-106: Global squared missing-mass spectra of the $\mathrm{n}(e, e'\pi^-)$ reaction on a LD_2 target. 85
62 E03-106: t dependence of the neutron moments compared to different VGG expectations. 86
63 E03-106: t dependence of the deuteron moments. 87
64 E04-012: The acceptance-weighted, combined missing-mass spectra obtained for the three reaction channels, after accidental coincidence background subtraction 91
65 E04-012: The upper and lower limit [top (blue) and bottom (red) solid lines at 90% confidence level for the production of the Σ_5^0 in the reaction $\gamma^* p \to K^+ \Sigma_5^0$ 93
66 E04-012: The 90% confidence level limits for the production of the N_5^0 in the reaction $\gamma^* p \to \pi^+ \mathrm{N}_5^0$. 93
67 E04-012: The 90% confidence level for the production of the Θ^{++} in the reaction $\gamma^* p \to K^- \Theta^{++}$. 94
68 E05-004: Angular distributions for recoil proton polarizations in deuteron photodisintegration, for $E_\gamma = 280 \pm 10$ MeV. 97

List of Tables

1 Main design parameters of the green Compton polarimeter upgrade, compared to the present infra-red system. 12

2 E94-107: (π^+, K^+) (KEK) and $(e, e'K^+)$ (JLab E94-107) production on ^{12}C, compared with theoretical predictions. 29

3 E94-107: (π^+, K^+) (KEK) and $(e, e'K^+)$ (JLab PRELIMINARY) production on ^{16}O, compared with theoretical predictions 30

4 E00-110: Experimental $ep \to ep\gamma$ kinematics 57

5 E03-104: Number of collected events on the hydrogen and helium targets 83

6 E04-012: Upper limits on the photoproduction cross section of the Σ_5^0, N_5^0 and Θ^{++} 92

1 Introduction

1.1 Introduction

Contributed by Kees de Jager

At the start of 2006 Hall A was in the middle of the largest installation since the HRS spectrometers were installed in 1995. Experiment E02-013 (Gordon Cates, Nilanga Liyanage, Bogdan Wojtsekhowski) required a polarized ^{3}He target, the BigBite spectrometer and the BigHAND neutron array. It was the first experiment to run in Hall A that used neither of the HRS spectrometers, but there were many more novelties. The polarized ^{3}He target used hybrid optical pumping with a specially designed holding field and compensating magnet. An optical fiber system was installed to transport the high-power laser light from the laser lab adjacent to the counting house, thus eliminating the need for the concrete laser hut close to the target. The BIGHAND neutron array was, with its 80 tons and sensitive area of 8 m^2 the largest dedicated neutron detector ever built. Finally, the BigBite spectrometer detector array was augmented to include three drift chambers and a lead glass shower counter. Thanks to the dedicated efforts of the technical support and design staff and the collaboration members, the installation was successfully completed only a couple of days late of the three months total of installation time scheduled. After a rough commissioning start, the experiment ran smoothly for over 10 weeks, accumulating accurate data at four Q^2-values, 1.4, 1.8, 2.2 and 3.4 GeV^2, more than doubling the Q^2-range for which G_n^E data were previously available.

After the successful completion of E02-013 the accelerator was tuned to 362 MeV for the low-energy backward-angle G0 run. Two experiments had been approved to run in parallel with G0 in Hall A, E05-103, deuteron photodisintegration at low energies (Ron Gilman, Adam Sarty, Steffen Strauch), and the first half of E05-004, a measurement of the deuteron elastic form factor A(Q) at low Q^2-values (Ron Gilman, Doug Higinbotham, Xiaodong Jiang). In order to accurately measure the beam current at the small values used in E05-004 a tungsten calorimeter had been designed and constructed by the Accelerator Division. Both experiments ran smoothly and accumulated the data requested with the quality required.

In September the accelerator was re-tuned to 687 MeV for the second backward-angle G0 run. First, the second half of E05-004 was successfully completed, followed by E03-104 (Rolf Ent, Ron Ransome, Steffen Strauch, Paul Ulmer), polarization transfer in the ^{4}He$(\vec{e}, e'\vec{p})$ reaction. Thanks to the fact that the Focal Plane Polarimeter had already been calibrated during E05-103 and to the excellent quality of the beam, E03-104 succeeded in collecting the very high statistics aimed at and will in parallel provide high-quality data on the charge form factor of the free proton and on the performance of the Focal Plane Polarimeter.

In the second half of November the target configuration was changed in preparation for E04-018, a measurement of the elastic form factors of ^{3,4}He up to large

Q^2-values (Javier Gomez, Mina Katramatou, Makis Petratos). After dedicating a number of days of beam to commission the HRS detector packages, the experiment ran very smoothly at high beam currents, accumulating most of the required forward-angle data on ^{3}He.

In February of 2006 a group of Hall A users and JLab staff, coordinated by Jian-ping Chen, completed a design report on the MAD spectrometer, updated in response to the findings of the Spectrometer Mini-Review of January 2004. All the concerns and issues raised in that review have been addressed in the updated design. To my deep regret the new design could not be comparatively reviewed with the Super-HMS design because of concerns that such a review could have a negative impact on the progress of the series of Critical Decision Reviews for the 12 GeV Upgrade. I can only express my appreciation for the hard work put into the design report by that group. On a positive note, the efforts to initiate two programs of parity-violating electron scattering in Hall A to be carried out with the 12 GeV Upgrade, one to study Møller scattering, the other Deep Inelastic Scattering, were strongly encouraged during two workshops in December, attended by leading experts.

Finally, I want to strongly encourage the completion of a number of long overdue archival papers. For major experiments it is essential that the details of the data taking, the analysis and the interpretation are widely accessible through publications in refereed journals.

2 Standard Hall A Facilities

2.1 The Hall A Compton Polarimeter

Contributed by Sirish Nanda

2.1.1 Overview

The Hall A Compton Polarimeter provides electron beam polarization measurements in a continuous and non-invasive manner via Compton scattering of polarized electrons from polarized photons trapped in a Fabry-Perot cavity. A schematic layout of the Compton polarimeter is shown in Fig. 1. The electron beam is transported through a vertical magnetic chicane consisting of four dipole magnets. A high-finesse Fabry-Perot cavity, injected with a 240 mW, 1064 nm infrared laser, serves as the photon target. Intra-cavity power remains stable at about 500 W. The Compton back-scattered photons are detected in an electromagnetic calorimeter consisting of lead tungstate crystals. The recoil electrons, separated from the primary beam by the fourth dipole of the chicane are detected in a silicon microstrip detector. The electron beam polarization is deduced from the counting rate asymmetries of the detected particles.

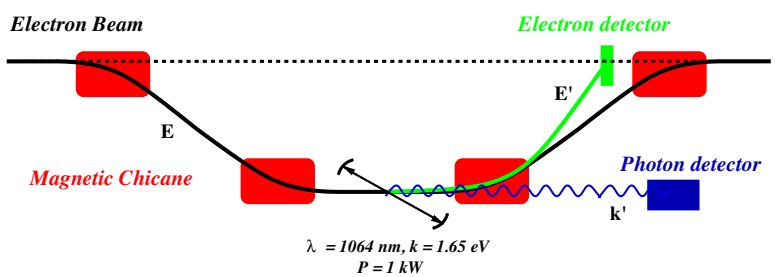

Figure 1: Schematic layout of the Hall A Compton polarimeter.

2.1.2 Recent Data

During 2006, the Compton polarimeter was utilized by the G_E^n (E02-013) experiment. Beam polarization data for the G_E^n experiment at 3.2 GeV obtained with on-line electron event analysis are shown in Fig. 2. Error bars represent statistical uncertainties only. We hope to achieve about 2% overall uncertainties after off-line analysis.

2.1.3 Green Laser Upgrade

The upgrade of the Compton polarimeter is motivated by upcoming high-accuracy experiments with a very demanding requirement on the beam polarimetry. Defin-

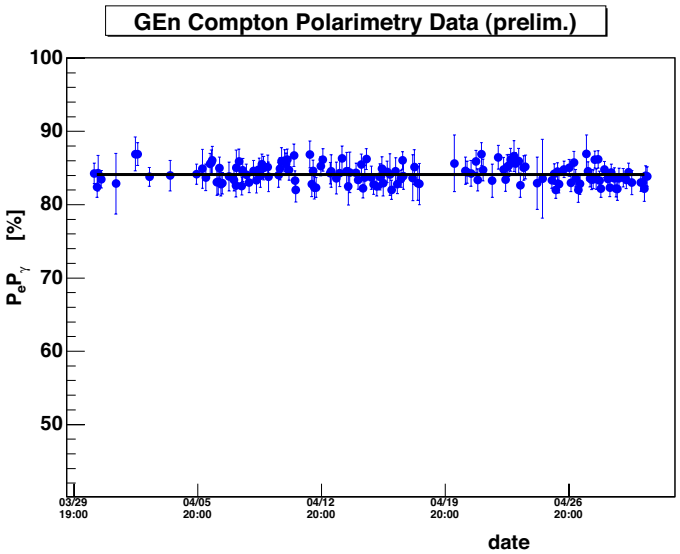

Figure 2: Preliminary beam polarization data taken for the G_E^n (E02-013) experiment during 2006 at 3.2 GeV beam energy. Error bars represent statistical uncertainties only.

ing k as the photon energy and E as the electron beam energy, the Figure Of Merit (F.O.M.) of a Compton measurement scales with $k^2 \times E^2$, making high-accuracy polarimetry a real challenge at low energy. The proposed upgrades are thus driven by the requirement of the Lead Parity experiment of 1% relative accuracy at 850 MeV. The present infra-red system, while capable of achieving such accuracies at higher energy ($\geq$ 6 GeV), falls far short at lower energies. We plan to upgrade the existing Fabry-Perot cavity operating at 1064 nm (IR) with about 1.5 kW power to a 532 nm (green) cavity with similar power. The figure of merit will increase 4 times compared to the IR system. In addition, improvements to the electron detector and photon calorimeter combined with the development of a new integrating method show promise of absolute accuracies approaching 1% at 0.85 GeV beam energy. The main parameters of the green Compton upgrade are shown in Table 1.

The conceptual design [1] of the green Compton polarimeter utilizes much of the design philosophy and the existing infrastructure of the present Compton polarimeter. A schematic layout of the optical setup for the upgrade is shown in Fig. 3. The heart of the upgrade plan is to replace the infrared cavity with a 532 nm green cavity fed by the new laser. Recent advances in the manufacturing of high-reflectivity and low-loss dielectric mirrors as well as availability of narrow line width green lasers meet our design goal. High gain cavities at 532 nm have been successfully constructed by the PVLAS [2] group that have a geometry and

Parameter	Present	Upgrade
Wavelength [nm]	1064	532
Cavity Power [W]	1500	1500
Cavity Q	1.0×10^{11}	1.8×10^{11}
FOM [σ.A^2] @0.85GeV	0.57	2.2
Energy Range [GeV]	2 - 6	0.8 - 6
$\delta P_e/P_e$ @0.85GeV	-	1%

Table 1: Main design parameters of the green Compton polarimeter upgrade, compared to the present infra-red system.

gain comparable to our proposed design here.

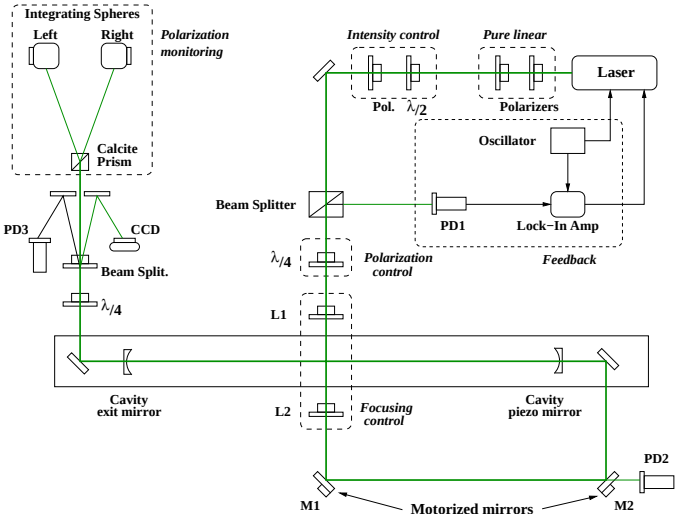

Figure 3: Optics table of the green Compton polarimeter.

2.1.4 Fabry-Perot Cavity

During the year, substantial progress has been achieved in the development of the green cavity. The design was completed for the production version of the prototype cavity tested last year. The cavity was fabricated and subsequently installed in the new Compton Polarimetry Lab in the ARC building during Summer of 2006. Illustrated in Fig. 4 is the fully assembled cavity under test in the lab.

The Prometheus green laser has been commissioned in full power (Class IIIb) mode in the the new Compton Polarimetry Lab. Full characterization of the laser beam profile and dynamic range has been completed. However, the laser showed

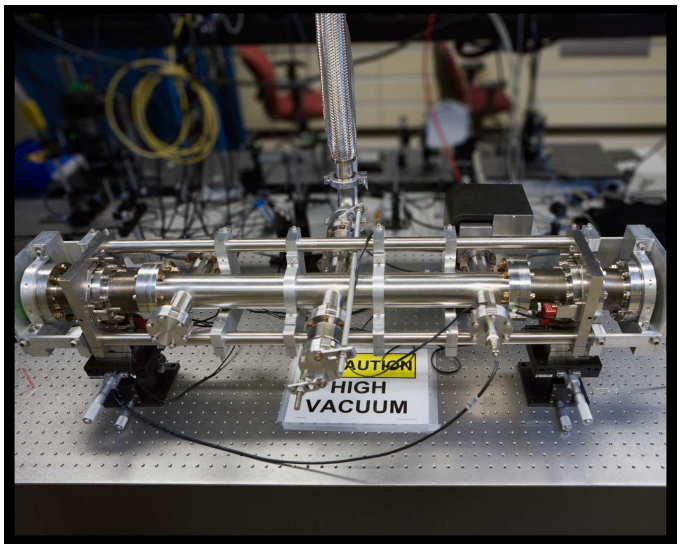

Figure 4: Green Fabry-Perot cavity under test in the Compton Polarimetry Lab.

significant power loss and intensity fluctuations. In September 2006, it was sent back to the Innolight factory for repairs. The two main pump diodes were replaced and a intensity noise-suppression system was installed. The laser was back in the lab in full operation in November.

Alignment of the cavity mirrors has been implemented via remotely-controlled high-resolution picomotors from New Focus Corp. The mirrors are aligned by collimating reflections from a red HeNe laser. The cavity shows excellent mechanical stability in retaining alignment. Furthermore, the cavity has been successfully vacuum tested to 10^{-7} Torr. We have been successful in obtaining clear photodiode signals of the transmitted and reflected power from the cavity while scanning the frequency of the laser. We have also carried out modulation studies with the laser beam using the internal PZT of the laser as well as and external electro-optic modulators and successfully generated frequency sidebands in the range of 100 to 1000 kHz. Using a lock-in amplifier, we have also generated noise-free PDH error signals essential for locking to the cavity. Illustrated in Fig. 5 are the reflected and transmitted power and the PDH error signals.

2.1.5 Detector Upgrade

As part of the upgrade, both the electron and the photon detectors will be replaced with higher performance detectors. The electron detector upgrade is being carried out by Laboratoire de Physique Corpusculaire IN2P3/Université Blaise Pascal, Clermont-Ferrand. The new detector has 4 planes of 192 silicon micro-strip with 240 μm pitch. The expected resolution is about 100 μm. In addition, to improve

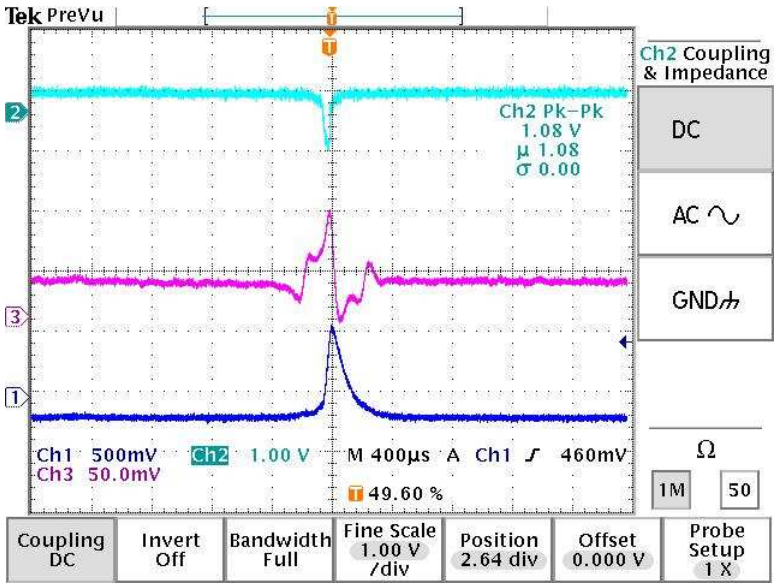

Figure 5: Characteristic signals of the new cavity: reflected power (top trace), PDH Error signal (middle trace), and transmitted power (bottom) trace.

the resolution, the electron detector will be configured to move in a vertical plane so as to facilitate covering the recoil electrons corresponding to the Compton edge over a broad range of energies.

The new silicon microstrip detectors have been ordered from Canberra systems and delivery is expected to be completed in early 2007. The final design of the detector support structures and vacuum chamber has been completed at LPC-Clermont. Illustrated in Fig. 6 are drawings and a CAD model of the design. A high-precision vertical motion of 120 mm for the detector has been incorporated in the design.

A new photon calorimeter with a single crystal, 75x75x250 mm^3 lead tungstate, coupled to a 3" PMT will replace the present multi-crystal array. The project is now in its conceptual design phase. This October, we carried out beam tests of the integrating DAQ with a Flash ADC at 2.6 GeV using the signal from the existing calorimeter. The data are being analyzed. We have requested further beam test time during Summer of 2007 to test the integrating photon DAQ.

We had the privilege of having two summer students, Alex Jousse, University of Grenoble, France and David Jacobs, Ohio State University, participate in the upgrade project. In addition, Prof. Ying Wu along with graduate student Botao Jia of Duke University have joined the efforts of the Compton Upgrade project starting last November.

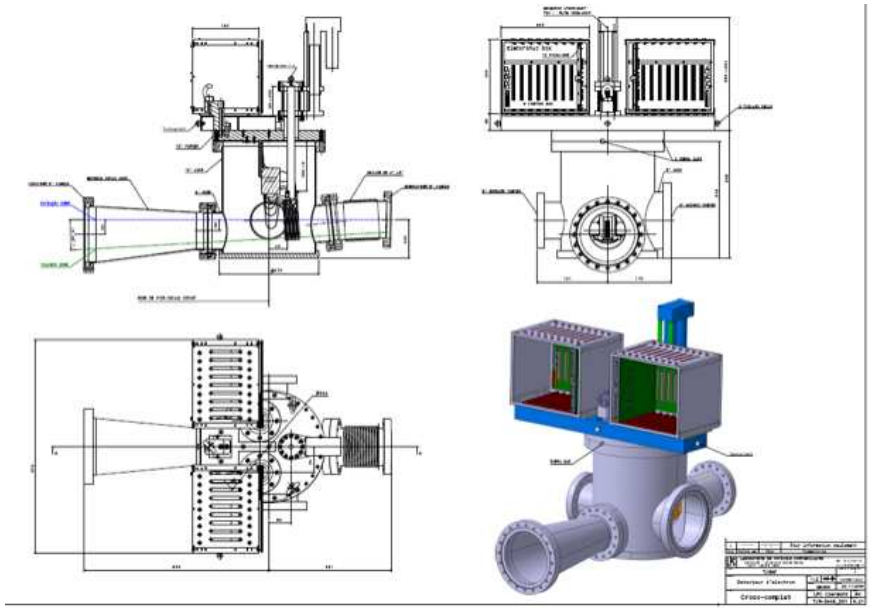

Figure 6: The new electron detector housing and vacuum chamber design completed by LPC-Clermont.

2.2 Large wire chambers for the BigBite spectrometer

Contributed by B. Wojtsekhowski, R. Lindgren and N. Liyanage.

2.2.1 Introduction

The BigBite spectrometer, that is only recently become operational, is already having a large impact on the Hall A research program. It has been requested by a large set of experiments accounting for more than 100 days of approved beam time at 6 GeV. The first PAC considering 12 GeV proposals, PAC30, has already approved one BigBite-based experiment, E12-06-122, and at least three others are being considered for PAC32. The BigBite spectrometer was first designed and constructed at NIKHEF [3] for the internal target facility at the storage ring AmPS using polarized atomic targets and a luminosity of the order of 10^{32} Hz/cm^2. This luminosity allowed a significant simplification of the read-out electronics and the wire chamber configuration. All applications of the BigBite spectrometer in Hall A require operation at a luminosity which is four to five orders of magnitude higher than it was at NIKHEF. An entirely new detector package was required to operate BigBite at these higher luminosity conditions in Hall A. The construction of a new set of wire chambers for BigBite became possible when a NSF Major Research Instrumentation (MRI) Grant was awarded to the University of Virginia (R. Lindgren and N. Liyanage) and with the dedicated efforts of the Hall A collaboration in preparation for the E02-013 experiment.

The key considerations for the parameters of new tracking detector were:

- multi-track capability;
- high spatial resolution;
- high counting-rate capability;
- minimum multiple scattering.

These general requirements led to a design with the wires oriented in three directions (U, V, X), three separate wire chambers with a total depth of the package approximately 0.7-1.0 m, a short drift distance, and very thin film-based cathode planes. In August 2002 we presented several options for the wire chamber design to the BigBite collaboration, which selected the one which was very successful in Hall C for the SOS spectrometer [4]. The University of Virginia organized a group which focused on the construction of the required large wire chambers and carried out this work over a period of the next three years. As an example, Fig. 7 shows one of the large wire chambers in the clean room at UVa. UVa research scientist V. Nelyubin with several graduate and undergraduate students developed a reliable construction method together with quality control techniques that resulted

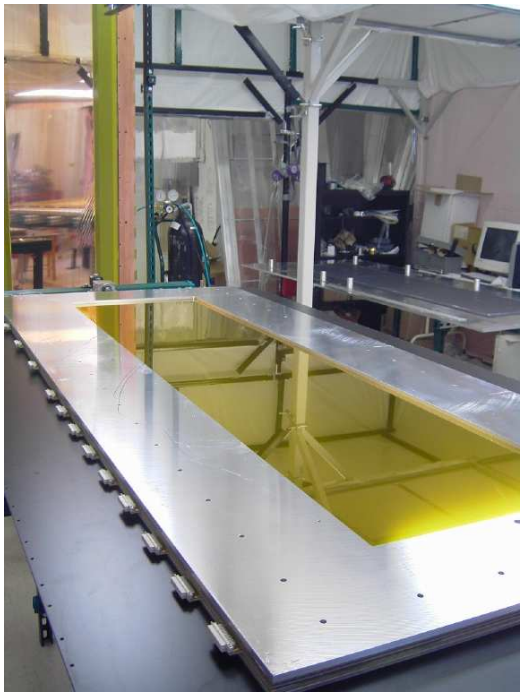

Figure 7: A large BigBite wire chamber in the clean room at UVa.

in excellent chambers for BigBite that operate with great stability and reliability.

Three large Multi-Wire Drift Chambers (MWDC) were constructed; each chamber with three pairs of planes with wires oriented at +60° (U), -60° (V), and 90° (X) with respect to the dispersive direction of the BigBite magnetic field. Each pair consists of two wire planes with a relative shift of the wires by 5 mm. This configuration of wires allows resolving the right-left ambiguity of the drift and an unambiguous hit assignment in multiple-hit events. Furthermore, the middle chamber dramatically improves track finding capability by just requiring a straight track through three chambers. The active area of the first chamber is 35 cm $\times$ 140 cm, while the active area of the second and third chambers is 50 cm $\times$ 200 cm. A wire plane consists of alternating sense and field wires. Figure 8 presents the arrangement of the wires and the cathode planes in a cross-sectional view of the chamber. The finished wire chambers were installed in the BigBite detector frame and were fully commissioned in the Test Lab before being moved to Hall A for the experiment. Figure 9 shows the BigBite detector in Hall A ready for installation behind the magnet.

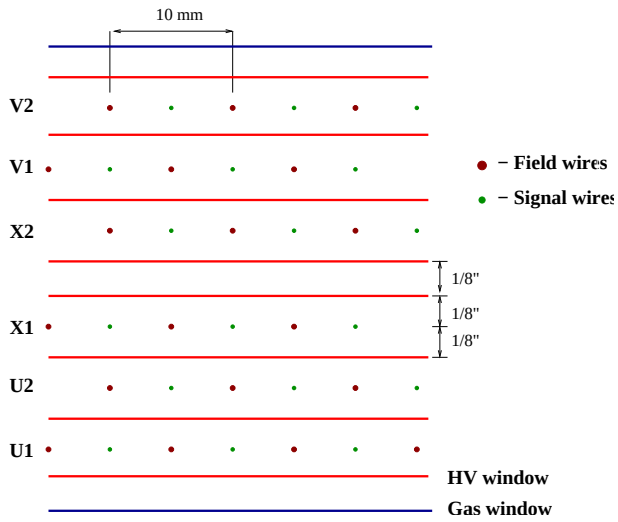

Figure 8: The electrode configuration of the front and the back chambers. The sense wires shown by smaller green dots are 20 μm Au-plated Tungsten wire, while the field wires shown by larger brown dots are 90 μm Cu-Be wire. The **X** wires are perpendicular to the dispersive direction while **U** and **V** wires are at +60° and -60° with respect to the dispersive direction. The high voltage is applied to 12 μm thick double-sided Cu-plated mylar films, indicated by the red lines. Each Cu layer is 0.12 μm thick. The gas windows shown by the blue lines are 24 μm thick Al-plated sheets of Kapton. The middle chamber consists of just one set of **X**, **U**, and **V** planes.

2.2.2 Chamber operation

The chambers were operated with a gas mixture of 65% Ar + 35% Ethane which flows through alcohol at 0°C and kept just above atmospheric pressure in the chamber. The gas flow was about 4-5 l/hour per chamber. The readout of the middle and the back chambers was based on Nanometric amplifier-discriminator cards N277C at a threshold voltage of 3.0 V. The first chamber was read out using new amplifier-discriminator cards especially designed at JLab after the test run in July 2005 had indicated a possibility of a very large background rate in the chamber at the conditions of the G_E^n experiment [5]. These low-noise cards use the new CAEN chip called MAD. The cards operated at a threshold 5-10 times lower than the N277C allowed a reduction of the high voltage on the front chamber by approximately 200 V. The operating high voltage for the front chamber was 1600 V, for the middle and back chambers 1750 V and 1800 V, respectively. For the nominal luminosity during the experiment, the counting rates were at the level of 20 MHz/plane (for the front chamber) and the leakage currents were around 100 μA/plane.

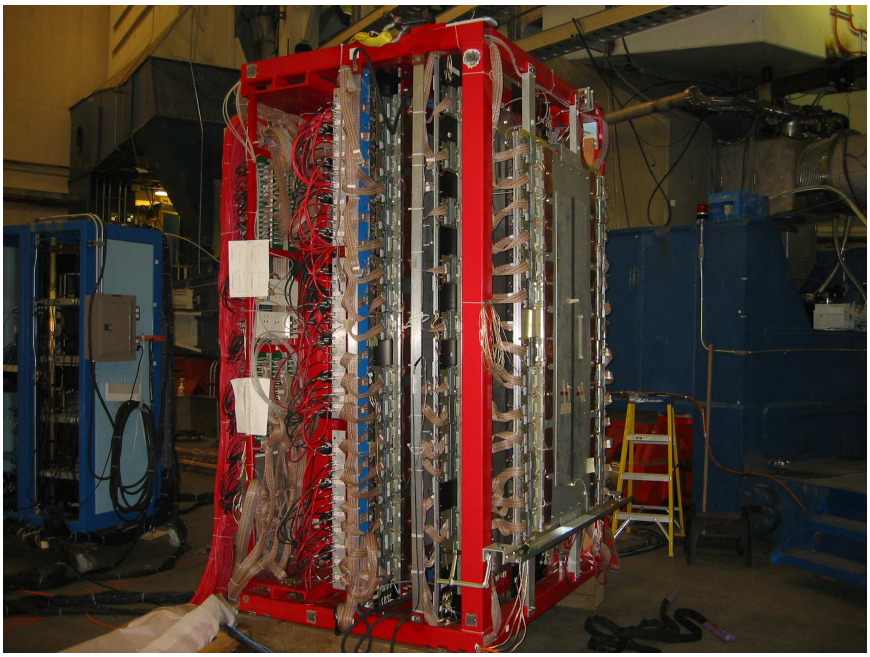

Figure 9: The detector package with the three MWDCs in Hall A is shown ready for installation in the BigBite spectrometer.

During the experiment, the chambers performed very well with all 2600 wires operational through the 2.5 month long run. Figure 10 shows the wire-hit histograms for a typical run during the experiment. The chamber resolution obtained from the analysis was approximately 300 μm, this is expected to improve to about 200 μm after further studies. Figure 11 shows the residual histograms for the X1 plane indicating a per-plane position resolution of $\sim$300 μm.

We are grateful to Dr. Liguang Tang for providing us with first-hand information and details on the design, construction technique, and contacts to the designer and suppliers for the Hall C SOS wire chambers; and to Mr. R. Sutter of BNL for his careful work in adapting the SOS chamber design to fit the proposed dimensions and wire-plane orientations of the BigBite chambers. We would like to thank the G_E^n collaborators, especially V. Nelyubin, B. Craver, A. Shahinyan, and I. Rachek, for their contributions to the BigBite wire-chambers project.

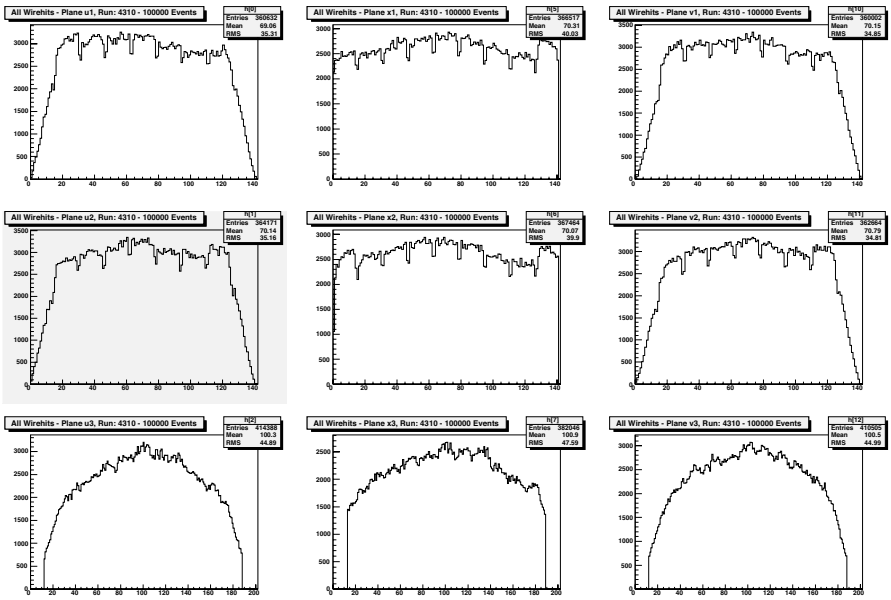

Figure 10: The wire-hit histograms for the front and the middle chambers in a typical run during the G_E^n experiment.

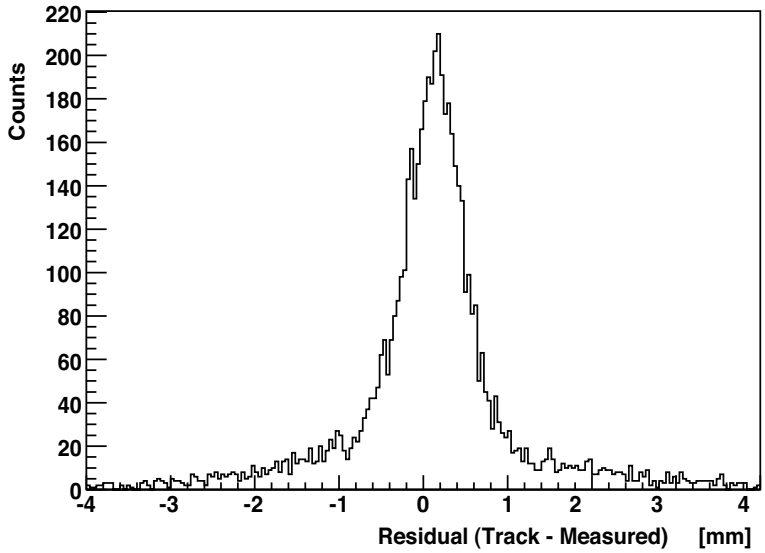

Figure 11: Residual histograms for the X1 plane indicating a per-plane position resolution of $\sigma \approx 300$ μm.

2.3 Beam Calorimeter

Contributed by Ron Gilman

The beam calorimeter was developed for precise current calibrations at low beam currents, needed for experiment E05-004, $A(Q)$ at Low Q in *ed* Elastic Scattering. Mike Bevins deserves primary credit for the design of the device. Arne Freyberger deserves primary credit for the overall implementation of the system. Pavel Degtiarenko and Eugene Chudakov simulated the device to determine the hadronic and electromagnetic energy losses.

The experimental goal of E05-004 is to measure precisely the cross section over a wide range of momentum transfers. At forward angles, corresponding to small momentum transfer, a few microamp current leads to tens of kHz of triggers in the HRS spectrometers, so it is important to have $\sim$1% current calibrations even at μA currents. The standard Hall A BCM system cross-calibrates the beam current monitors (BCMs) to an Unser monitor, which has a noise level of a few tenths of a μA. Thus, the system can only achieve $\sim$1% precision for currents above about 20 μA. The calorimeter was designed to allow 1% calibrations for currents as low as a few tenths of 1 μA.

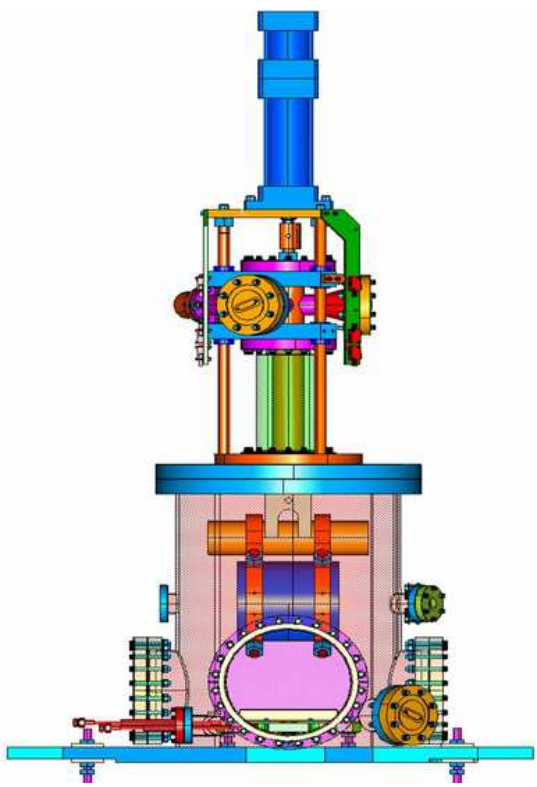

Figure 12: Mechanical drawing of the calorimeter. See text for details.

Figure 12 shows the design of the calorimeter, with the calorimeter slug (shown colored blue) in a position to intercept the beam. When the exposure is finished, the calorimeter can be moved down towards the cooling plate (yellow). The slug is about 16 cm diameter and 16 cm long, with the bottom flattened for better thermal contact with the cooling plate. With the slug just above or on the cooling plate, the beam passes through a hollow support tube (orange) above the slug.

For a calibration, the cylindrical tungsten-copper slug is moved up so that the beam enters along its axis. The slug absorbs the full energy of the beam, except for $\sim$0.5% electromagnetic and hadronic energy loss. Backsplash is minimized through a small entry well. The temperature rise of the slug is determined through a set of 6 temperature sensors. The total energy absorbed is then determined using the measured slug heat capacity, which was determined through a precision power supply feeding energy into the slug, with the temperature rise measured by the same thermometry system. The total charge of the beam is calculated from the energy deposited, corrected for losses, divided by the beam energy. As a cross check, the calorimeter is also instrumented as a Faraday cup, but no detailed estimates has been done of the charge losses.

After exposure, the calorimeter can be moved out of the beam, but off the cooling plate, so that the experiment can continue while the heat diffuses through the calorimeter and the temperature stabilizes; monitoring is typically done for several minutes. The cooling plate can be used to lower the temperature so that calibrations can be redone within about 30 minutes; otherwise it takes about a day for the calorimeter slug to cool.

The calorimeter is designed to operate at powers of up to 2.5 kW, with the total energy deposited limited to 150 kJ, corresponding to a temperature rise of about 20 K. These limits protect the calorimeter from damage, and ensure that it is operated in the range in which it was calibrated. Uncertainty estimates for the system indicate that $\sim$0.5% precision might be achievable. There are several uncertainties all at the level of 0.1 – 0.2%, including uncertainties for the heat capacity, thermometry, and hadronic and electromagnetic energy losses, beam energy, and radiative and conductive heat losses.

Calorimeter calibrations were done about a dozen times during the July - September, 2006, running of the two low-energy deuteron experiments, with currents ranging from about 0.1 – 6 μA. The main difficulty encountered was with the chiller. Although the controls were shielded in a concrete hut about 5 m upstream of the target, high-luminosity running apparently led to radiation damage. Preliminary data analysis indicates that the beam current calibrations are good to $\sim$1%; however the analysis of the data, including the reproducibility of the measurements, is not complete. Preliminary results from the Faraday cup analysis are systematically below the calorimetry measurement by slightly under 1%.

More details about the calorimeter design can be found in two conference proceedings [6,7].

2.4 Data Analysis

Podd — C++/ROOT Analysis Software

Contributed by J.-O. Hansen

A maintenance release, version 1.4, of the Hall A data analysis package Podd appeared in 2006. It includes various corrections and smaller improvements that had accumulated since the release of version 1.3 in June 2004. As was already reported in part last year, the following features were added:

- Improved support for split CODA input files;
- Improved support for split ROOT output files;
- Support for writing arbitrary ROOT objects to the ROOT output file (e.g. TLorentzVector);
- Support for writing the non-event data from analysis objects (detectors, apparatuses, physics modules) to the ROOT output file, for example to document calibration and geometry parameters used for the analysis;
- Support for G0 helicity scheme; improved handling of helicity data;
- Improved scaler package with more functionality (see the online scaler documentation);
- The χ^2 of the cluster track fitting in the HRS VDCs is calculated;
- More calculated kinematics variables available as global variables from kinematics physics modules;
- Support for new prescale event type;
- Fix for incorrectly calculated HRS VDC plane spacings; this may require re-optimization of matrix elements since it affects the calculated V-slopes;
- Support for gcc4 and 64-bit environments;
- Support for ROOT 5.

The new version is source-compatible with prior versions with one small exception that affected the RICH detector plugin and has been patched in the RICH CVS repository.

The main structural improvement in the new Podd version is the decoder. The decoder interface is now an abstract base class, and the actual implementation can be chosen by the user. A standard CODA file decoder is provided as the default, and an alternative front-end interface to simulation data (VDCsim) is available in a separate package. The simulation front-end was already described in last year's report.

All production experiments that ran in 2006 used Podd for their online and offline data analysis. The largest development of user code during 2006 was clearly

the AGEN library for the G_E^n experiment. This library includes support for both the G_E^n neutron detector and the full BigBite spectrometer; in particular, the tracking code for the BigBite wire chambers is now available. This major development illustrates the power of the new object-oriented approach to data analysis: the G_E^n collaboration required very little time to "integrate" the G_E^n-specific analysis code into the overall system, but instead was able to focus on the actual analysis problems. This ability simply to "plug in" a major analysis library for an experiment with non-standard equipment was exactly the goal of the development of Podd. Preliminary results from the G_E^n run, in particular details on the performance of the tracking code, as well as the other 2006 experiments can be found in the respective experiment sections in this report.

Currently, we are working on a number of significant enhancements that will be included in the upcoming version 1.5 in early 2007. The helicity analysis class has been greatly improved and is currently available as a separate plugin module; it is planned to integrate this code into the Podd core, replacing the old helicity routines. In addition, the database system has been reworked to use a generic programming interface (API) that allows the use of plain-text database files, an SQL database, or any other database back-end without rewriting any of the core Podd code or user plugins. With this update, the work of retrieving database elements will be done by the database package instead of individual detector classes. Finally, the speed of the ROOT file output package will be improved as it is often the bottleneck in the analysis flow.

The work reported here was carried out in collaboration with Rob Feuerbach, who coordinated the G_E^n software effort, wrote most of the neutron detector code and made many of the smaller improvements, and Bob Michaels, who created all the helicity code. Seamus Riordan realized the BigBite tracking code almost single-handedly. Sincere thanks to everyone who helped making the Hall A software a success.

3 Summaries of Experimental Activities

3.1 E94-107

High-resolution hypernuclear $1p$-shell spectroscopy

F. Garibaldi, S. Frullani, J. LeRose and T. Saito, spokespersons,
and
the Hall A Collaboration

3.1.1 Present status and outlook

Experiment E94-107 at Jefferson Lab was designed to perform high-resolution hypernuclear spectroscopy by electroproduction of strangeness on $1p$-shell targets: ^{12}C, ^{9}Be, ^{16}O. The first part of the experiment on ^{12}C and ^{9}Be targets was performed in January and April-May 2004 in Hall A. The second part of the experiment on ^{16}O was carried out in June 2005. The physics motivation, the experimental challenges and the improvements of the Hall A apparatus (septum magnets, optics, aerogel detectors, RICH detectors, waterfall target) were described in previous Hall A status reports. The status of analysis and the further improvement on RICH detector are presented here.

3.1.2 High-Resolution Spectroscopy of $^{12}_{\Lambda}$B by Electroproduction

In Fig. 13 the excitation energy spectrum of $^{12}_{\Lambda}$B is shown for the full range of energy acceptance. The filled histogram shows the level of (e, e'), (e, K^+) random coincidence background. The ^{12}C results show that a high-quality, background-free $^{12}_{\Lambda}$B hypernuclear spectrum with unprecedented energy resolution ($\sim$640 keV) has been obtained.

Figure 14 shows the six-fold differential cross section expressed in nb/sr^2/GeV MeV. The background has been evaluated by fitting the data obtained for random coincidences in a large timing window and subtracted. No residual background in the negative range of E_x is present after subtraction.

The solid line represents the best fit to the data. The dashed line is the result of a theoretical model which shows very good overall agreement with the data without any normalization factor. Publication of these results is imminent.

One essential ingredient of any hypernuclear cross-section calculation is the model for the elementary cross section of K^+–Λ electroproduction on the proton. Since counting rates for hypernuclear electroproduction decrease dramatically with increasing Q^2 and $\theta_{\gamma K}$, these experiments at electron beam facilities are always carried out at very low Q^2 and with kaon detection at forward angles. As will be discussed in the following, this is exactly the region where there is a lack of precision data for the $p(e, e'K^+)\Lambda$ reaction and where the existing data show

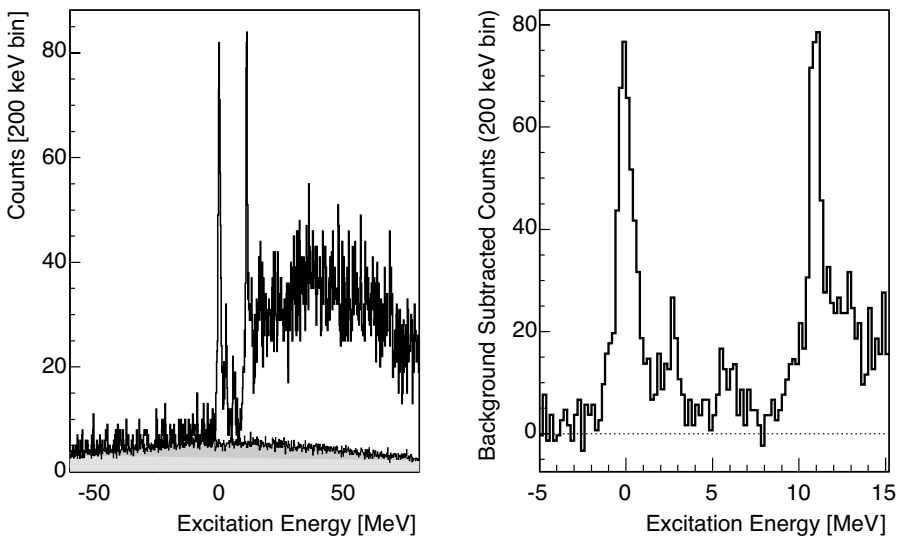

Figure 13: Left panel: ${}^{12}_{\Lambda}$B excitation-energy spectrum as obtained after kaon selection with aerogel detectors and RICH without background subtraction. The electron-kaon random coincidence contribution evaluated in a large timing widow and normalized is superimposed on the spectrum. The unique feature of an almost background-free experiment can be observed. Right panel: exploded view of the hypernuclear bound-state region with background subtracted.

large discrepancies and also where models show a very different behavior with huge differences in cross-section predictions.

The model that has been used to compare our data with theory (dashed line in the figure) is obtained in the framework of the Distorted Wave Impulse Approximation (DWIA) [8] using the Saclay-Lyon (SLA) model [9] for the elementary $p(e, e'K^+)\Lambda$ reaction. Shell-model wave functions for ^{11}B and ${}^{12}_{\Lambda}$B were obtained using fitted p-shell interactions and a parametrization of the ΛN interaction that fits the precise γ-ray spectra of ${}^{7}_{\Lambda}$Li [10].

The very good agreement of the data with the predicted cross section is a first, though indirect, indication that the SLA model gives a good description of the elementary cross section at Q^2 as low as 0.07 GeV^2 and at forward-angle kaon detection.

For the first time a measurable strength with good energy resolution has been observed in the core-excited part of the spectrum. The s_Λ part of the spectrum is well reproduced by the theory. The distribution of strength within several MeV on either side of the strong p_Λ peak should stimulate theoretical work to better understand the p_Λ region.

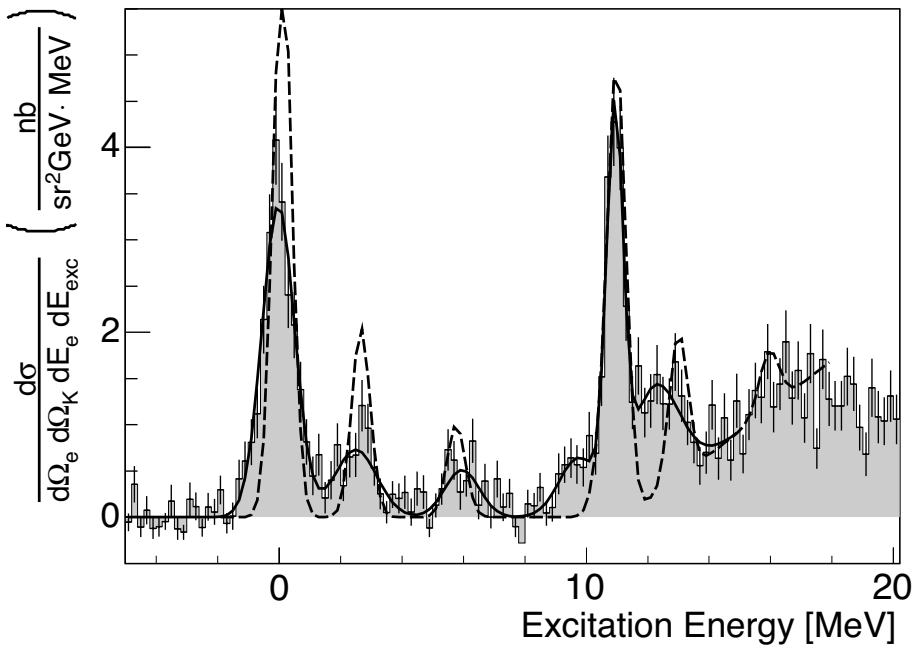

Figure 14: ${}^{12}_{\Lambda}$B excitation-energy spectrum. The best fit (solid) and a theoretical curve (dashed) are superimposed on the data. See text for details.

3.1.3 ^{16}O$(e,\, e'$K$^+)^{16}_{\Lambda}$N and H$(e, e'K^+)\Lambda$ reactions

A waterfall target was used during experiment E94-107 for hypernuclear production on oxygen nuclei as well as for the measurement of the elementary cross section p$(e,\, e'$K$^+)\Lambda$ on hydrogen nuclei.

Kinematics were set for electron detection at 6° for scattered electrons with momentum of 1.44 GeV/c, an incident beam energy of 3.66 GeV, a virtual photon energy of 2.2 GeV with $Q^2 = 0.06$ GeV^2. Scattered kaons were detected with a momentum of 1.96 GeV/c at 6°.

Figure 15 shows the preliminary data obtained for the ${}^{16}_{\Lambda}$N hypernuclear spectrum produced on Oxygen nuclei at $Q_{K^+e} = 6°$. The solid line is the result of a theoretical calculation obtained with the SLA model for the elementary cross section and by using J. Millener's calculations for the hypernuclear structure. The theoretical curve has been normalized to the data at this stage of the analysis. The overall picture shows a very good agreement between the data and the calculations, especially in terms of positions and relative strength of the levels. However, at the present stage of the analysis a discrepancy of a factor 2 between the data and the calculations is found in terms of absolute cross sections, the data suggesting smaller cross sections. This result is also consistent with a previous (π^+, K^+) experiment carried out at KEK [11]

In Table 3.1.3, the experimental cross section for the (π^+, K^+) reaction (in-

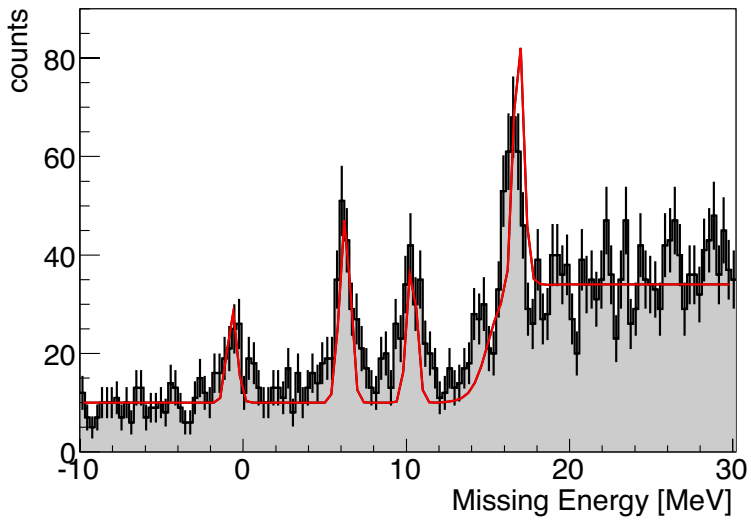

Figure 15: Preliminary data for the ${}^{16}_{\Lambda}$N missing-energy spectrum. The solid red curve presents the result of the theoretical calculation (see text for further details).

tegrated over the angular range $\theta_K = 2^o - 14^o$) and from the $(e, e'K^+)$ JLab experiment on ^{12}C and ^{16}O targets are compared with theoretical predictions (two sets of theoretical predictions differ in the assumed binding energy of p_Λ state - a Wood-Saxon wave function is used for the weakly bound p_Λ). One can see that in the case of ^{12}C the agreement is surprisingly good but for ^{16}O the theoretical predictions overestimate the data approximately by a factor 2 for the low-energy hypernuclear states $\Lambda \in s_{1/2}$. Taking into account that the structure of the closed-shell ^{16}O nucleus should be more simple than that of ^{12}C, this is rather surprising and at the moment we have no explanation for it.

HN levels		KEK (π^+, K^+)			E94-107 $(e, e'K^+)$	
$E_x[MeV]$	J^π	$\sigma^{exp}_{2^o-14^o}$	$\sigma^{the1}_{2^o-14^o}$	$\sigma^{the2}_{2^o-14^o}$	$d^3\sigma_{exp} \pm stat. \pm sys.$	$d^3\sigma_{the}$
0.00	$1^-, 2^-$	1.44±0.03	1.53	1.53	$4.47 \pm 0.21 \pm 0.58$	4.68
~ 2.65	1^-	0.24±0.02	0.25	0.25	$1.26 \pm 0.11 \pm 0.16$	1.54
~ 6.00	$1^-, 2^-$	0.23±0.02	0.16	0.16	$0.72 \pm 0.09 \pm 0.09$	0.76
8.12		0.18±0.02				
9.77					$0.91 \pm 0.10 \pm 0.12$	
~ 11.0	$0^+, 2^+, 3^+$	1.81±0.05	3.28	2.18	$2.90 \pm 0.17 \pm 0.38$	3.98
~ 12.2	2^+				$2.42 \pm 0.16^{+0.41}_{-0.73}$	1.18

Table 2: (π^+, K^+) (KEK) and $(e, e'K^+)$ (JLab E94-107) production on ${}^{12}C$, compared with theoretical predictions.

HN levels		KEK (π^+, K^+)			E94-107 $(e, e'K^+)$	
$E_x[MeV]$	J^π	$\sigma^{exp}_{2^o-14^o}$	$\sigma^{the1}_{2^o-14^o}$	$\sigma^{the2}_{2^o-14^o}$	$d^3\sigma_{exp}$	$d^3\sigma_{the}$
0.000	1^-	0.41±0.02	0.96	0.96	1.3 ±40%	2.50
∼6.5	$1^-, 2^-$	0.91 ±0.03	1.68	1.68	2.8 ±40%	4.54
∼11	$1^+, 2^+$	1.05 ±0.03	1.95	1.35	2.5 ±40%	3.94
∼17.5	$1^+, 2^+, 3^+$	1.38 ± 0.06	4.12	2.86	3.8 ±40%	7.62

Table 3: (π^+, K^+) (KEK) and $(e, e'K^+)$ (JLab E94-107 - PRELIMINARY results) production on ^{16}O, compared with theoretical predictions

The preliminary results for the simultaneous measurement of the elementary reaction on hydrogen shows also a similar discrepancy between the data (σ = 23 nb/sr^2/GeV ± 40%) with respect to the predicted cross section of 36 nb/sr^2/GeV according to the SLA model.

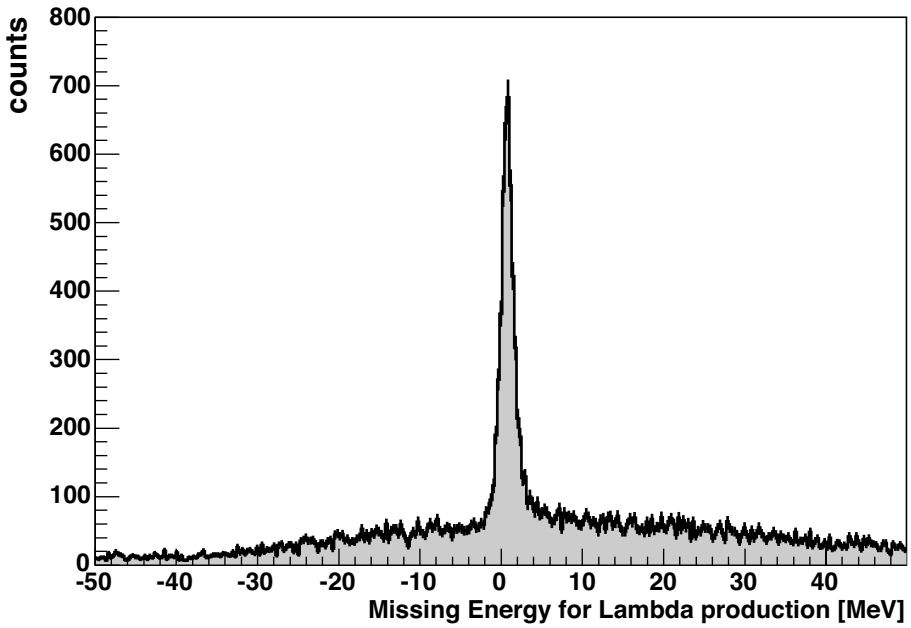

Figure 16: Preliminary data for the p(e, e'K$^+$)Λ measured on the waterfall target in the experiment E94-107.

3.1.4 RICH detector upgrade

The RICH detector will be upgraded to match the needs of the approved transversity experiment (E06-010/E06-011). The photon detection plane will be doubled (3 more pad panels added) to be able to identify kaons of 2.4 GeV/c, as shown

in the MonteCarlo generated Fig. 17. This will allow the detectors to separate kaons, in our kinematical conditions with a higher rejection ratio.

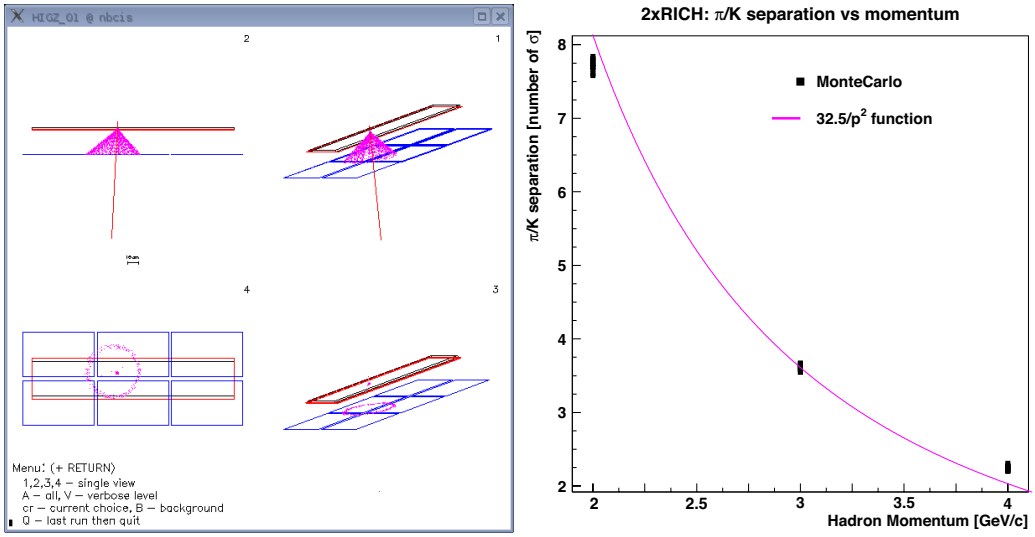

Figure 17: Left panel: upgraded RICH simulated event; right panel: expected pion/kaon angle separation (in terms of number of sigma) at different hadron momenta. The simulation is tuned to the existing hypernuclear experiment data.

3.1.5 Conclusion

The goal of experiment E94-107 was to carry out a systematic study of light hypernuclei (p-shell). The experiment required important modifications of the Hall A apparatus. The new experimental equipment showed excellent performance. The RICH detector performed as expected and was crucial in the kaon selection. The major effort in 2006 has been devoted to the analysis of Carbon data that has now been completed. The first paper is circulating in the collaboration. The data from the waterfall target are in an advanced stage. Very promising physics is coming out from these new data for ^{16}N hypernuclear spectroscopy and for the $p(e, e'K)$ cross-section measurement. A preliminary evaluation of the cross section has been done. Improvement in the missing-mass resolution has been obtained. The next steps will be to finish the waterfall target analysis (Oxygen and Hydrogen) and to write a paper. The analysis of ^{9}Be will be finished and possibly finalized in another paper.

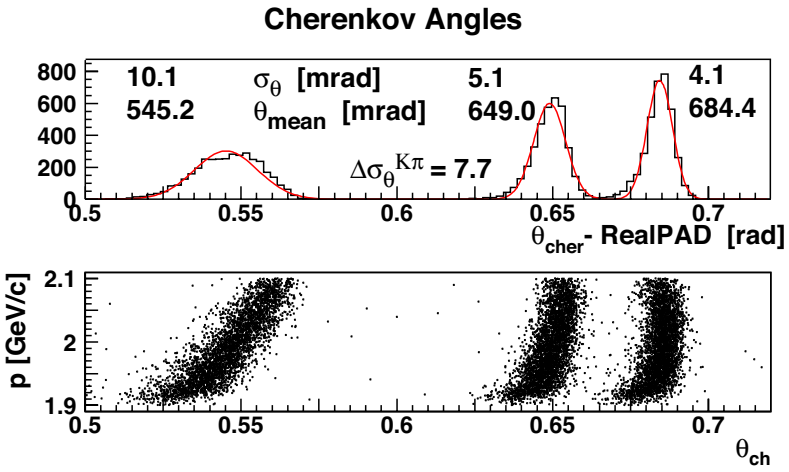

Figure 18: Upgraded RICH simulated performance: pion/kaon angular distribution (equal hadron population) at 2.0 GeV/c momentum, within the HRS acceptance (±5%). The MonteCarlo is tuned to the existing hypernuclear experimental data.

3.2 E97-110

The GDH Sum Rule, the Spin Structure of ^{3}He and the Neutron using Nearly Real Photons

J.-P. Chen, A. Deur and F. Garibaldi, spokespersons,
and
the E97-110 and Hall A Collaborations

The goal of the experiment is to measure the generalized Gerasimov-Drell-Hearn integral (GDH) and moments of spin structure functions at low Q^2 on the neutron and ^{3}He. A brief description of the physics goal and of the running of the experiment was given in the 2003 Hall A report.

3.2.1 The experiment

The experiment ran in April-May and July-August 2003. The first part of the experiment (low Q^2, April-May 2003) acquired data with a mis-wired septum magnet. The septum was fixed in June and the experiment was completed in July-August.

3.2.2 Present state and outlook

Data-analysis efforts have been concentrated on the second period which contains the bulk of the data and is easier to analyze.

The optics study of the spectrometer-septum combination has been completed (V. Sulkosky, Col. of William and Mary) as has the acceptance study and SNAKE-modeling of the magnetic transport for 6° (V. Sulkosky). It has been tested using data taken on carbon foils in the elastic regime, see Fig. 19 which shows an absolute comparison of simulated and experimental data on the Carbon elastic peak. The agreement between the simulated and experimental carbon elastic cross section at the present stage of the analysis is typically about 2-3% at 6°. The same analysis will be carried out for 9°. The Particle Identification (PID) analysis, which comprises the calibration of preshower and shower detectors and Čerenkov counters, and PID efficiency analysis, are completed (H. Lu et al, USTC: University of Science and Technology of China). A parallel analysis has been conducted (J. Yuan, Rutgers). Preliminary detector and DAQ efficiencies have been determined. A remaining task is to develop an algorithm to deal with multi-track events for the high rate settings and compare its result to the efficiency extracted from the data (J. Yuan, Rutgers). The nitrogen analysis that determines the dilution of the ^{3}He asymmetry has been completed (X. Zhan, MIT), as has the beam characterization for the second run period (T. Holmstrom, Col. of William and Mary). The C++ analyzer was adapted for the experiment and batch analysis codes are available (J. Singh, V. Sulkosky), with the exception of possible helicity

misdecoding when the dead time is high. This, which would affects the first period only, will be investigated by R. Feuerbach (W&M). A database recording the characteristics and quality of runs is available for both the first and the second periods (J. Singh, UVa). Analysis of the target polarimetries (NMR and EPR) as well as other target characteristics is well under way (J. Singh), and preliminary numbers are available.

Preliminary inelastic asymmetries are available for both 6° and 9°, and the E = 2.23 GeV, 9° asymmetries are shown in Fig. 20. Preliminary inelastic cross sections are also available for 6°. The two remaining major items before obtaining a preliminary GDH sum are: 1) radiative correction, on which J. Singh is presently working, and 2) background estimates, which is being studied by T. Holmstrom.

The data analysis for the first period is also underway, mostly done by our Chinese collaborators at USTC.

The near term plan is to obtain a 9° acceptance function and inelastic cross sections (V. Sulkosky). Then, V. Sulkosky will form preliminary GDH sum results. The remaining analysis includes: complete analysis of the elastic cross sections and asymmetries for the various targets available; finalization of inelastic cross section and asymmetry analysis; finalization of radiative corrections, analysis of the experimental uncertainties (J. Singh) and final estimate of the background.

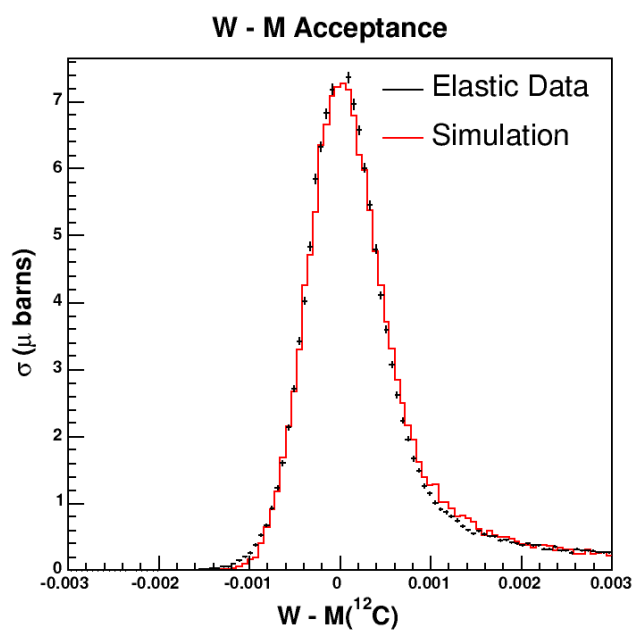

Figure 19: Preliminary Carbon elastic cross section. In red: simulation, black symbols: experimental data

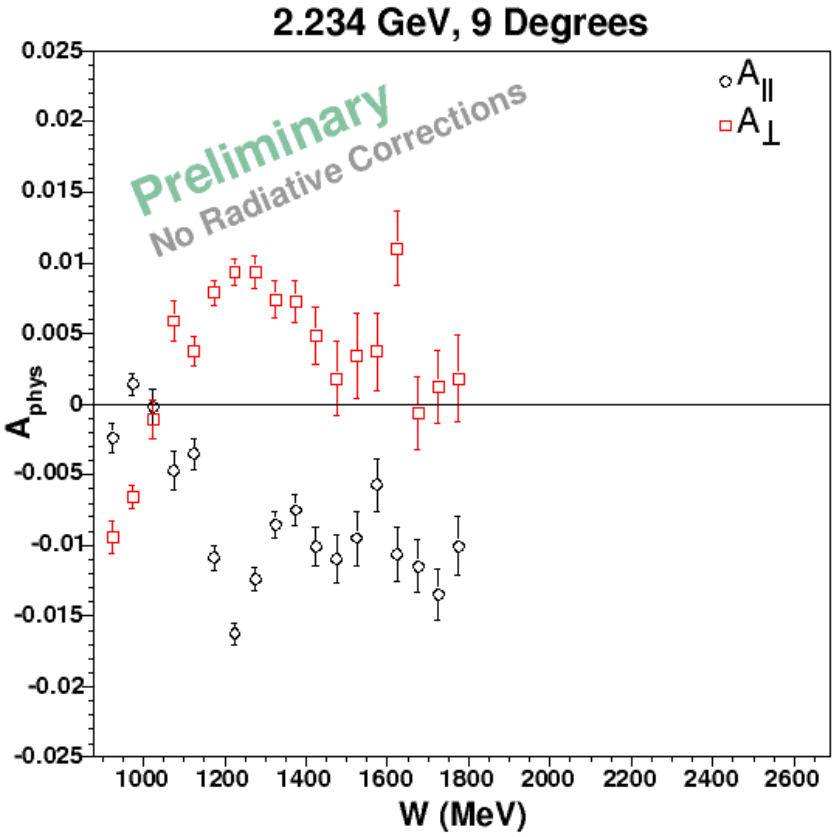

Figure 20: Preliminary inelastic asymmetries for 9° scattering angle and beam energy of 2.23 GeV. The transverse asymmetry is shown in red and the longitudinal one in black. Radiative corrections and a correction for finite binning have not been applied yet.

3.3 E99-114

Real Compton Scattering from the Proton at High Momentum Transfer

Charles Hyde-Wright, A. Nathan, and B. Wojtsekhowski, spokespersons,
and
the Hall A Collaboration

3.3.1 Introduction

Understanding the structure of hadrons requires accessing the fundamental quark and gluon degrees of freedom of QCD. Real Compton Scattering (RCS) is a unique probe of the proton, as there are no hadronic dynamics in the initial or final channels. However, as RCS is a second-order process, the full QCD dynamics enters the reaction between the space-time points of photon absorption and emission. The present study of RCS at high energy and momentum transfer was undertaken with the dual purpose of testing contemporary theories of the reaction mechanism and extracting a novel form factor of the quark structure of the proton.

The only data for RCS in the hard scattering regime were obtained 25 years ago by the pioneering Cornell experiment [12]. It was observed that the experimental cross section was at least 10 times larger than that predicted by asymptotic pQCD, in which the reaction is mediated by the exchange of two hard gluons [13–16]. More recently, calculations have been done using the handbag mechanism [17,18], in which the external photons couple to a single quark, that couples to the spectator particles through the Generalized Parton Distributions (GPD). These calculations are rather close to the Cornell cross-section data. The apparent non-applicability of asymptotic pQCD and dominance of the handbag mechanism was reinforced by a recent measurement of the longitudinal polarization transfer parameter K_{LL} [15, 19], that is in fair agreement with the handbag prediction [19] and in unambiguous disagreement with the pQCD prediction. The present experiment was designed to test more stringently the reaction mechanism by improving the statistical precision and extending the kinematic range of the Cornell data.

3.3.2 Experiment

The experiment, shown schematically in Fig. 21, was performed in Hall A, with basic instrumentation described in Ref. [20]. A 100% duty-factor electron beam with a current up to 40 μA and energies of 2.34, 3.48, 4.62, or 5.75 GeV was incident on a 0.81-mm thick Cu radiator. The mixed beam of electrons and bremsstrahlung photons was incident on a 15-cm liquid H_2 target, located just downstream of the radiator, with a photon flux of up to 2×10^{13} equivalent quanta/s. The scattered photon was detected in a calorimeter consisting of an array of 704 lead-glass blocks ($4 \times 4 \times 40$ cm^3) placed a distance 5-18 m from the target and sub-tending a solid

angle of 30-60 msr, with a typical position resolution of 1 cm and energy resolution σ_E/E= 5-7%. The associated recoil proton was detected in one of the Hall A High Resolution Spectrometers (HRS), with a solid angle of 6.5 msr, momentum acceptance of $\pm 4.5\%$, relative momentum resolution of 2.5×10^{-4}, and angular resolution of 2.4 mrad, the latter limited principally by scattering in the target. The central momentum of the HRS was set to detect protons corresponding to incident photons at a mean energy of approximately 90% of the electron beam energy. The trigger was formed from a coincidence between a signal from a scintillator counter in the HRS focal plane and a signal in the calorimeter greater than half the expected RCS photon energy.

3.3.3 Analysis

Potential RCS events were selected based on the kinematic correlation between the scattered photon and the recoil proton. The excellent HRS optics were used to reconstruct the momentum, direction, and reaction vertex of the recoil proton to determine the energy of the incident photon and to calculate δx and δy, the difference of in-plane and out-of-plane coordinates, respectively, between the expected and measured location of the detected photon on the front face of the calorimeter. An example of the distribution of events in the δx-δy plane is shown in Fig. 22. The RCS events, which are in the peak at $\delta x = \delta y = 0$, lie upon a continuum background primarily from the $p(\gamma, \pi^0 p)$ reaction, with the subsequent decay $\pi^0 \rightarrow \gamma\gamma$. An additional background is due to electrons from *ep* elastic scattering, which is kinematically indistinguishable from RCS. A magnet between the target and the calorimeter (see Fig. 21) deflects these electrons horizontally 10-20 cm relative to undeflected RCS photons, so that the *ep* events are clearly separated from the RCS events, as shown in Fig. 22. By making the coplanarity cut $\mid \delta y \mid \leq 15$ cm, then projecting onto the δx axis, one obtains the δx distribution shown in Fig. 23. The curve is a calculation of the π^0 continuum background, which we now discuss.

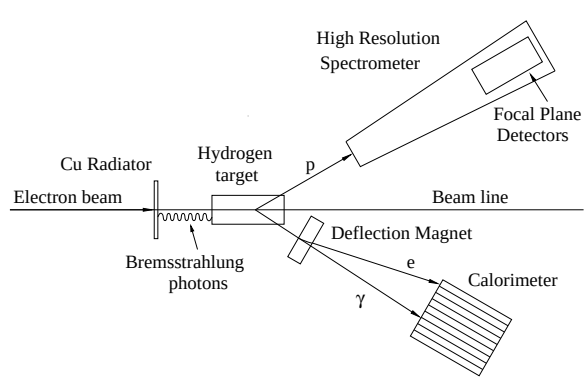

Figure 21: Schematic layout of the RCS experiment.

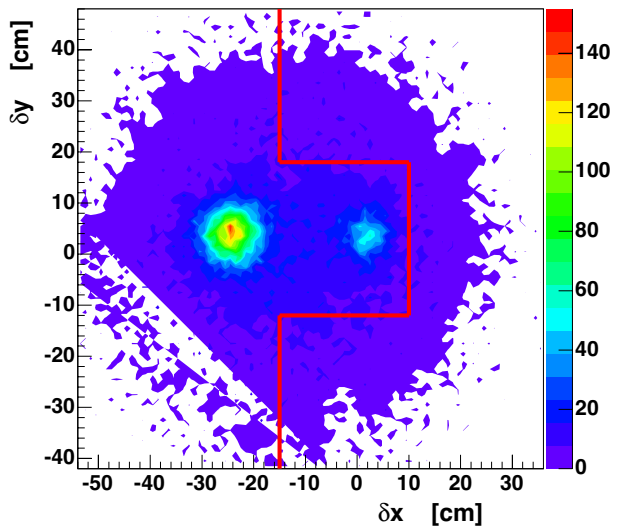

Figure 22: Kinematic correlations of the photon-proton events for the kinematics $s = 6.79$, $-t = 3.04$ GeV^2. Shown is a contour plot of the difference between the predicted and measured in-plane (δx) and out-of-plane coordinates of the photon on the front face of the calorimeter. The predicted coordinates are based on the measurement of momentum, direction, and reaction vertex of the recoil proton in the HRS. The peaks near $\delta x = \delta y = 0$ and $\delta x = -25$, $\delta y = 0$ contain the RCS and *ep* events, respectively. The continuum events are photons from π^0 photoproduction. The events to the right of the solid red line are used to normalize the π^0 events in the Monte Carlo simulation.

A Monte Carlo simulation of the experiment was used to determine the acceptances of the combined HRS-calorimeter system and to determine the π^0 contribution to Fig. 23. The simulation utilized a thick-target bremsstrahlung code to calculate the incident photon spectrum [21]; an event generator for RCS, (γ,π^0), and *ep* elastic scattering; and the SIMC code [22] to track recoil protons through the HRS. Dedicated $p(e, e'p)$ runs were performed with the Cu radiator removed to verify that SIMC correctly accounts for the distribution of proton recoil events in momentum, angle, and reaction vertex across the acceptance of the HRS and to confirm that the known *ep* cross section is reproduced to better than 3% [23,24]. To determine the π^0 background, the simulated π^0 events are normalized to the number of actual events in regions of δx-δy space that are free of RCS and *ep* events (see Fig. 22), then used to calculate the curve in Fig. 23. The tight kinematic constraints of our coincidence geometry precludes contributions from heavier mesons, such as η's. Subtracting the curve from the data, then integrating over the region of δx shown in Fig. 23, the "raw" RCS cross section is determined. As a byproduct

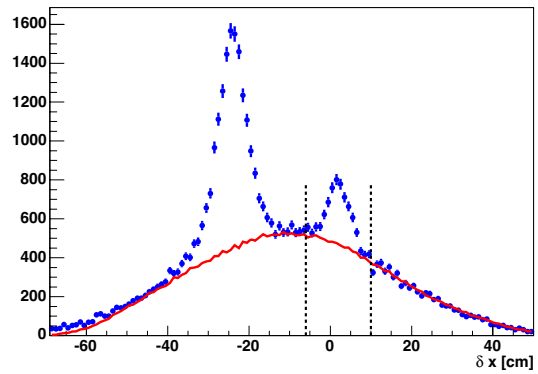

Figure 23: Distribution of δx, with a coplanarity cut $\mid \delta y \mid \leq 15$ cm, with the RCS and ep events indicated. The curve is a Monte Carlo calculation of the continuum π^0 events. The vertical dashed lines are the cuts used to calculate the number of RCS events.

of this analysis, we have obtained cross sections for the $p(\gamma, \pi^0)p$ reaction, which will be presented in a later publication.

Two corrections need to be applied to obtain the final RCS cross section. The first correction is due to $ep\gamma$ events in which an elastically scattered electron radiates a hard photon in the material between the target and deflection magnet. Such events will fall in the $\delta x = 0$ peak in Fig. 23 and are distinguishable from RCS events by their energy, as measured in the calorimeter. We use the Monte Carlo to calculate the shape of the background, then normalize the calculation to the number of events below the RCS peak in the E_{calo} spectrum, as shown in Fig. 24. The $ep\gamma$ events contribute from $\sim$2% at backward angles to as much as 23% at forward angles.

The second correction is due to quasi-real photons from the $p(e, p\gamma)e'$ reaction. We simulate that reaction with our Monte Carlo, using the spectrum of quasi-real photons calculated according to the method of [25]. Although the scattered electron is not detected, the kinematic cuts on the HRS and calorimeter–particularly the δx and δy cuts–place stringent constraints on the virtuality of the photon. We find that the quasi-real photons have a mean Q^2=0.14$\times$ 10^{-3} GeV^2 and contribute in the range 11-15% to the total incident photon flux, depending on the kinematic point.

3.3.4 Results

The cross-section data are presented in Fig. 25 along with the previous Cornell data [12]. The curves are theoretical predictions based on the handbag diagram. The solid curves are calculations based on the GPD approach [19], in which the

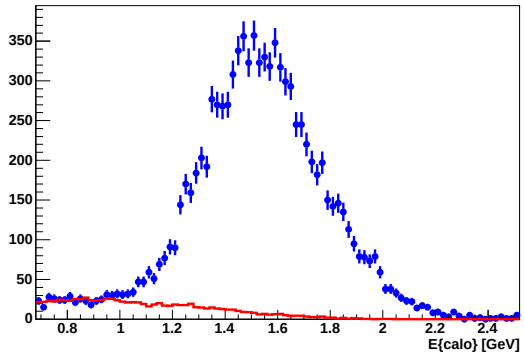

Figure 24: Energy distribution in the calorimeter for events with $|\delta y| \leq 15$ cm and $|\ \delta x\ | \leq 8$ cm. The events between 0.7 and 1.0 GeV were used to isolate the $ep\gamma$ background in order to normalize the simulation, shown as the red histogram.

photon-parton subprocess is calculated to next-to-leading order (NLO) in α_s and a model is used for the GPDs based on the known parton distribution functions and the nucleon electromagnetic form factors. The widths of the shaded areas indicate the uncertainties due to the mass uncertainties in the hard subprocess [26]. The dashed curves also use the handbag diagram [27], using the constituent quark model to calculate the hard subprocess and quark wave functions adjusted to fit existing data for the nucleon electromagnetic form factors. Both sets of curves cover a limited range in $-t$ because the calculations based on the handbag mechanism are valid only for $s, -t, -u$ larger than approximately 2.5 GeV^2. Over that range they are in good agreement with the data. It is interesting to examine the scaling behavior of the cross section at fixed θ_{cm}, where the asymptotic pQCD mechanism predicts $d\sigma/dt = f(\theta_{cm})/s^n$ with $n = 6$. We have extracted the scaling power $n(\theta_{cm})$ from the present cross-section data and plotted them in Fig. 26, along with the Cornell data. [12]. Both the data and the GPD-based handbag calculation, shown as the dashed curve, are in good agreement with a fixed value $n = 7.9 \pm 0.2$, in contradiction to asymptotic pQCD.

The GPD-based handbag calculations lead to a factorization of the RCS cross section into a product of the Klein-Nishina (KN) cross section from a quark and a sum of form factor-like objects [18]:

$$\left.\frac{d\sigma}{dt}\right|_{\mathrm{RCS}} = \left.\frac{d\sigma}{dt}\right|_{\mathrm{KN}} R_V^2 \left[f_V + f_A \left(\frac{R_A}{R_V}\right)^2 \right] , \tag{1}$$

where f_V and f_A are kinematic factors. The vector and axial form factors, R_V and R_A, contain new information about the structure of the nucleon that is accessible only through the RCS reaction. In the kinematics of the present experiment, $f_A \ll f_V$; therefore we expect R_A to make only a small contribution to our cross

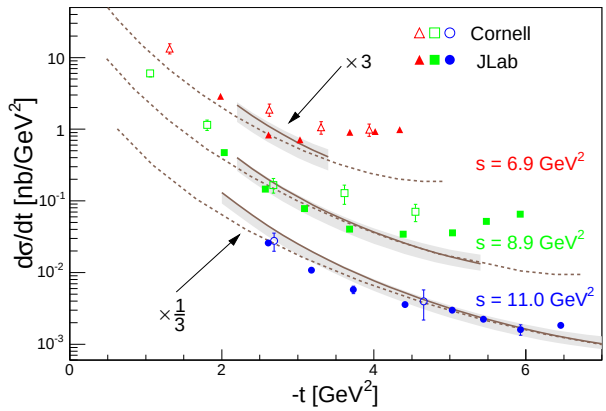

Figure 25: Cross section of the RCS process vs. transferred momentum t at three values of s. Full points and open points are data from the present and Cornell experiments [12], respectively, the latter corrected for differences in s values assuming a scaling power of 7.5.

section. We therefore focus the discussion on R_V, which is derived from the same GPD H^a as the Dirac form factor F_1 [17,18]:

$$R_V(t) = \sum_a e_a^2 \int_{-1}^{+1} \frac{dx}{x} H^a(x;0,t) \tag{2}$$

$$F_1(t) = \sum_a e_a \int_{-1}^{1} dx\, H^a(x,0,t) \tag{3}$$

where a denotes the quark flavor. The present measurement of the cross section over a wide range of t allows extraction of the form factor R_V, utilizing the NLO expressions of Ref. [19] for f_V and f_A. The ratio $R_A/R_V = 0.81$ was taken from our polarization measurement [28] and was assumed to be independent of s and t. The results for R_V are shown in Fig. 27 for $-u \geq 2.5$ GeV^2. We note that values of R_V derived at fixed t but different s are in excellent agreement with each other, lending strong credence to the factorization implied by Eq. 1. Moreover, R_V is approximately given by $1.4F_{1p}$, which should help to further constrain H^a.

In summary, the RCS cross section from the proton was measured in a range s = 5-11 GeV^2 at large momentum transfer. Calculations based on the handbag diagram are in good agreement with experimental data, suggesting that the reaction mechanism in the few GeV energy range is dominantly one in which the external photons couple to a single quark. The cross-section data were used within the framework of Ref. [19] to extract $R_V(t)$, a new form factor of the quark structure of the proton.

We would like to thank P. Kroll, J. M. Laget, and G. Miller for discussions of the physics of wide-angle Compton scattering.

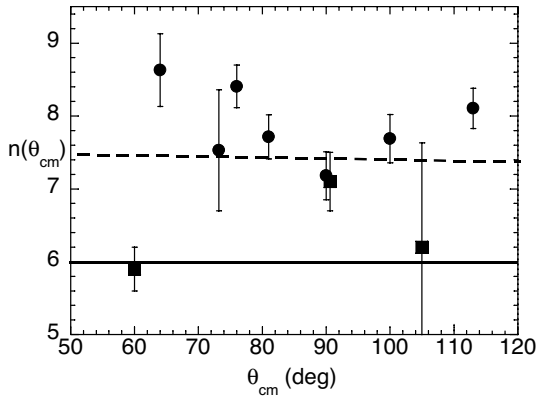

Figure 26: Scaling of the RCS cross section at fixed θ_{cm}. Square points are results from the Cornell experiment [12]. Solid circles are results from the present experiment. The solid curve is the prediction (n=6) of asymptotic pQCD, while the dashed curve is the GPD-based handbag calculation.

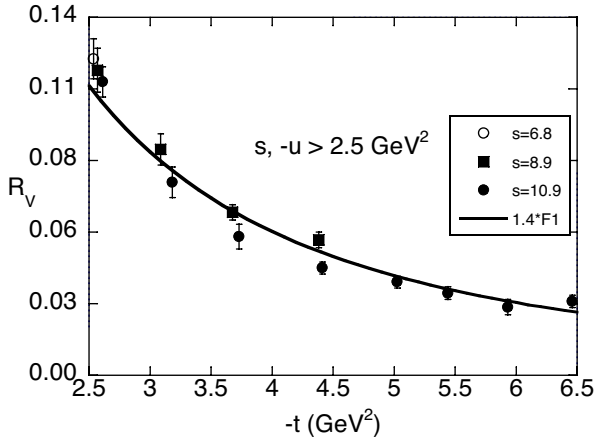

Figure 27: Extracted RCS form factor R_V. The solid line is F_{1p}, scaled by a factor 1.4.

3.4 E99-115 and E00-114

Results from the HAPPEx Experiments

G. Cates, K. Kumar, D. Lhuillier, D. Armstrong and R. Michaels, spokespersons,
and
the Hall A Collaboration

3.4.1 Introduction

The Hall A Proton Parity Experiment (HAPPEx) collaboration took data in 2005 and has submitted the results for publication [29]. The timely publication and unprecedented accuracy demonstrate that the Hall A spectrometers and the JLab beam are well suited for performing parity-violation experiments, and this bodes well for the future of the parity program in Hall A. The experiment measured the electroweak asymmetry in elastic scattering of 3 GeV electrons off hydrogen and ^{4}He targets at $\langle\theta_{lab}\rangle \approx 6°$. The asymmetry is defined as $A = (\sigma_R - \sigma_L)/(\sigma_R + \sigma_L)$ where $\sigma_{R(L)}$ is the differential cross section for elastic scattering of right(R) and left(L) handed longitudinally polarized electrons. The ^{4}He result is $A_{\rm PV} = (+6.40 \pm 0.23\ (\text{stat}) \pm 0.12\ (\text{syst})) \times 10^{-6}$. The hydrogen result is $A_{\rm PV} = (-1.58 \pm 0.12\ (\text{stat}) \pm 0.04\ (\text{syst})) \times 10^{-6}$. The asymmetry for hydrogen is a function of a linear combination of G_E^s and G_M^s, the strange quark contributions to the electric and magnetic form factors of the nucleon respectively, and that for ^{4}He is a function of G_E^s alone. The measurements imply $G_E^s + 0.09\,G_M^s = 0.007 \pm 0.011 \pm 0.006$ at $\langle Q^2\rangle = 0.109\,\text{GeV}^2$ and $G_E^s = 0.002 \pm 0.014 \pm 0.007$ at $\langle Q^2\rangle = 0.077\,\text{GeV}^2$. The helium result is the first time parity violation was measured in that nucleus and it is the smallest fractional error bar ($\leq 4\%$) ever achieved in a parity experiment. The hydrogen result had a systematic error ≤ 100 ppb due to the impressive "parity quality" of the JLab beam.

3.4.2 Motivation

The motivation for this experiment is to study the role of strange quarks in the structure of nucleon, a research topic of great interest in the past 15 years. The electroweak asymmetry in polarized electron scattering is a particularly clean way to access the strange vector matrix elements [30–36].

We briefly remind the reader how parity violation allows extraction of strangeness. Electromagnetic scattering at a given kinematics can measure only two linear combinations of the Sachs form factors. For example, the proton form factors in terms of u, d, and s quark form factors are:

$$G_{E,M}^{\gamma p} = \frac{2}{3}G_{E,M}^{u} - \frac{1}{3}G_{E,M}^{d} - \frac{1}{3}G_{E,M}^{s} \tag{4}$$

where $G^f_{E,M}$ is the electric (E) or magnetic (M) form factor for quark flavor f. Here it is assumed that the quark flavors u, d, and s contribute and the goal is to determine $G^s_{E,M}$, the strangeness form factors.

Charge symmetry between proton p and neutron n is normally assumed, so that for the quark form factors

$$G^u_p = G^d_n \; ; \quad G^d_p = G^u_n \; ; \quad G^s_p = G^s_n \tag{5}$$

where the subscripts p and n are for proton and neutron.

Since there are too many quark form factors for the given number of nucleon electromagnetic form factors, one needs additional information to determine whether or not there is a contribution from the strangeness form factors $G^s_{E,M}$. This is provided by parity violation because the Z^0 of the weak interaction accesses the same flavor structure with different coupling constants given by the Standard Model. For a proton:

$$\begin{aligned} G^{Zp}_{E,M} = & \left(\frac{1}{4} - \frac{2}{3}\sin^2\theta_W\right) G^u_{E,M} \; + \\ & \left(-\frac{1}{4} + \frac{1}{3}\sin^2\theta_W\right) \times \left[G^d_{E,M} + G^s_{E,M}\right] \end{aligned} \tag{6}$$

Parity violation in elastic scattering from the ^{4}He nucleus is directly sensitive to G^s_E. Neglecting well-known radiative corrections the asymmetry is

$$A_{\rm PV} = A_0 \tau \left\{ 4 \sin^2 \theta_W \; + \; \frac{2G^s_E}{G^p_E + G^n_E} \right\} \tag{7}$$

where

$$A_0 = \frac{G_F M_P^2}{\sqrt{2}\pi\alpha} = 316.7 \text{ ppm} \tag{8}$$

Thus, by combining measurements from the proton and from helium we can separate G^s_E and G^s_M. The interpretation of the experiments is quite clean, requiring only the assumptions of charge symmetry in the proton and that at our low Q^2 nuclear effects in ^{4}He are under sufficient control theoretically.

The 2005 HAPPEx measurements were made at very low Q^2 where one is sensitive mainly to the static moments ρ_s and μ_s, the strangeness radius and magnetic moment. Most theoretical models focus on predictions of these static moments at $Q^2 = 0$, while only a subset of the models attempt to predict the form factors at higher Q^2 (for reviews see [33–36]). The problem is one of non-perturbative QCD dynamics and is very challenging.

3.4.3 Experimental Issues and Progress

The HAPPEx experiments use the two HRS spectrometers at equal angles to the beam; this doubles our rate and helps constrain and cancel some systematics,

e.g. transverse polarization. The septum magnets provided by INFN allowed us to reach 6° scattering angle. The high resolution provides the major advantage of suppressing backgrounds and permitting an integrating technique: we simply place a total absorption detector at the elastic peak and integrate the PMT signal from Čerenkov light from each detector. The signal is integrated over the duration of a helicity pulse. This relies on there being very little background. We measure our background in separate calibration runs in counting mode at low rate using the VDCs. Low-rate counting measurements were also carried out to measure Q^2, which required a new kind of kinematic recoil analysis from a water target to calibrate the scattering angle to the required precision. The beam polarization is measured every few days by a Møller polarimeter and monitored continuously with a Compton polarimeter. The experimental techniques are described in more detail in Refs. [29,37–39].

The septum magnets were supplemented in 2005 with small "sweeper magnets", which swept away low-energy charged backgrounds that cause heating in the septum coils and had limited our beam current in 2004. The sweeper magnets worked well for the hydrogen target, allowing us to run at high current, but they did not have much impact for helium, probably because of neutron backgrounds.

In 2005, we made tremendous progress in controlling helicity-correlated systematics, see Fig. 28 which shows the helicity-correlated position differences, which average to ∼1 nanometer during the run. This accomplishment is due to a long-term effort to improve the optics setup at the polarized source as well as the tune of the accelerator. Most of the work to control systematic errors is done at the polarized source. The helicity-correlated intensity asymmetry was maintained to be less than 1 ppm by an active feedback loop. We have a well-developed model for reducing and controlling the laser systematics. For the accelerator, progress in understanding the betatron matching has helped achieve maximum dampening of position differences, while improved understanding of beam tuning provided good phase advances along our beam line that permit us to simultaneously have good measurements of the sensitivities to each of the beam parameters.

There was also a significant improvement in the systematic error of Compton polarimetry.

3.4.4 Results for G_E^s and G_M^s

Comparing our results to the theoretical expectations, we extract $G_E^s = 0.002 \pm 0.014 \pm 0.007$ at $Q^2 = 0.077\,\mathrm{GeV}^2$ and $G_E^s + 0.09 G_M^s = 0.007 \pm 0.011 \pm 0.004 \pm 0.005$ (FF) at $Q^2 = 0.109\,\mathrm{GeV}^2$, where the uncertainties in the nucleon electromagnetic form factors govern the last error. Figure 29 displays the combined result for these and our previous measurements [38,39], taken with $\langle Q^2 \rangle$ between 0.077-0.109 GeV^2. The requisite small extrapolation to a common $Q^2 = 0.1\,\mathrm{GeV}^2$ was made assuming that $G_E^s \propto Q^2$ and that G_M^s is constant. The values $G_E^s = -0.005 \pm 0.019$ and $G_M^s = 0.18 \pm 0.27$ are obtained.

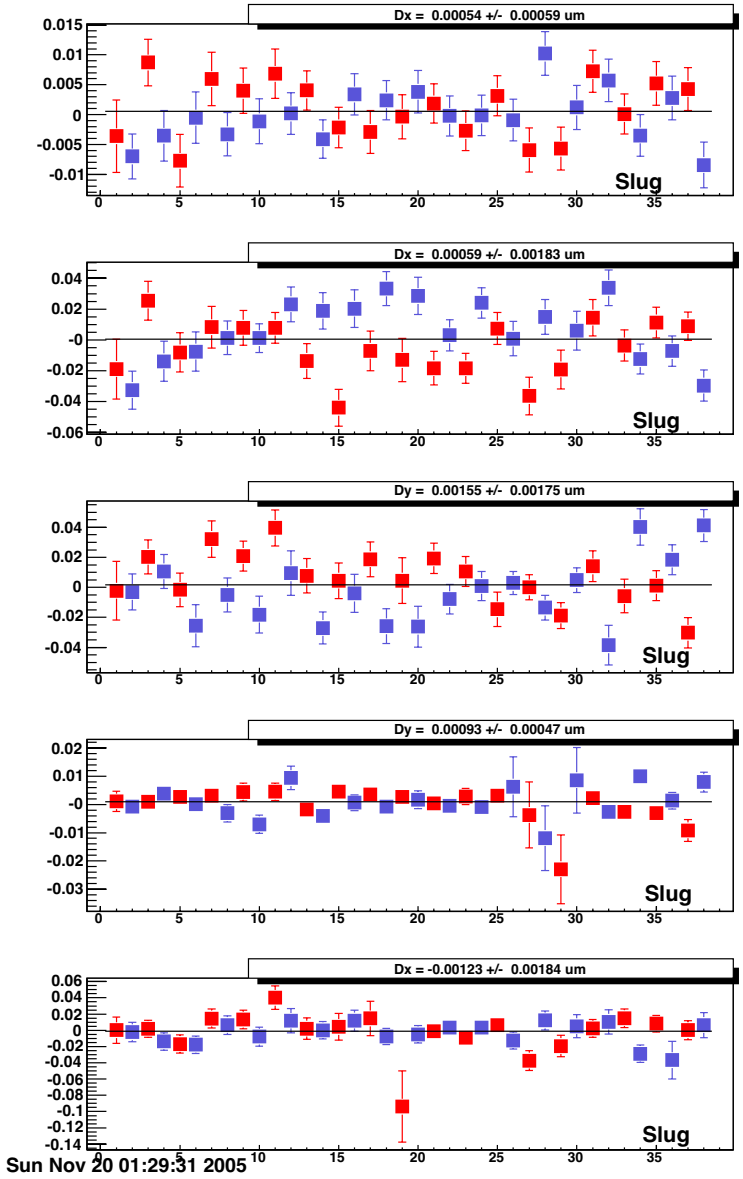

Figure 28: "Parity quality" beam. Shown are helicity-correlated beam monitor differences (μm) versus slug number (1 "slug" $\sim$ 1 day of running) for HAPPEx. The top four plots are X and Y monitors near the target, and the bottom plot is a monitor in the dispersive section of the magnet ARC leading into the hall, providing a relative energy monitor. The averages over a month of running are $\sim$ 1 nanometer.

Figure 29 also displays predictions from selected theoretical models to set the scale (for the references see our publication [29] which has the same figure). Those that predict little strange quark dynamics in the vector form factors are favored [40,41]. Other measurements [42–44] that had suggested non-zero strangeness effects are consistent, within quoted uncertainties, with our results at $Q^2 = 0.1\,\mathrm{GeV}^2$. Due to the improved statistical precision and lower G_A^Z sensitivity of our result, adding these earlier published measurements does not alter our conclusions.

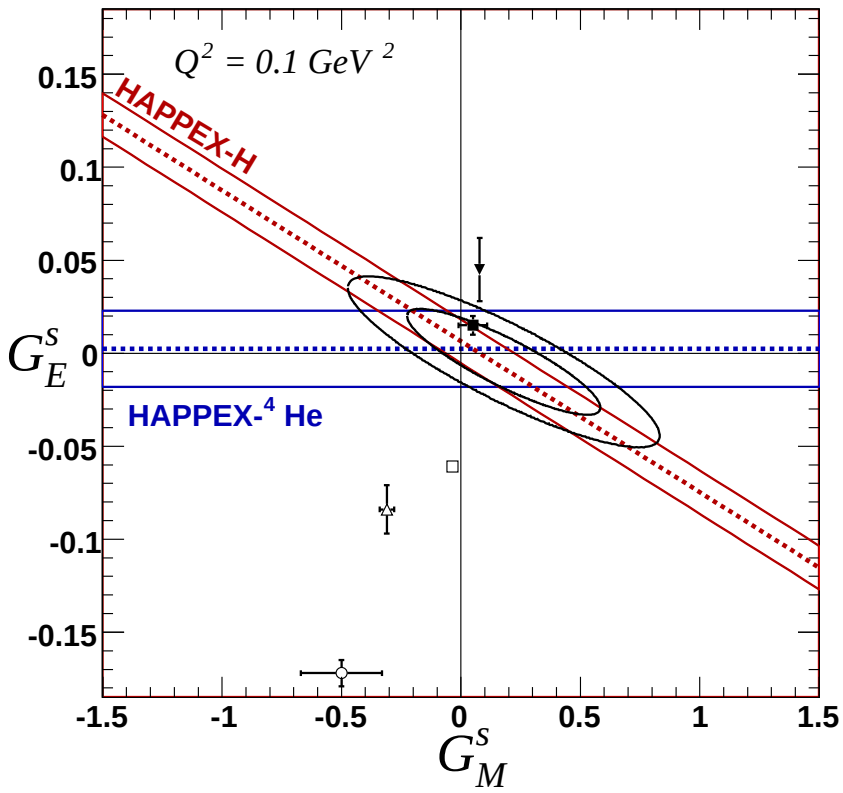

Figure 29: HAPPEx constraints on strangeness form factors. Shown are the 68% and 95% C.L. constraints in the $G_E^s - G_M^s$ plane from the present data ([38,39] and the 2005 measurement). Various theoretical predictions are plotted (see the plot in [29] which contains the references). The 1-σ bands (a quadrature sum of statistical and systematic errors) and central values from the new results alone are also shown.

3.4.5 Summary and Outlook

HAPPEx has published the most precise constraints on the strange form factors at $Q^2 \sim 0.1\,\mathrm{GeV}^2$. The results are consistent with other parity experiments [42–44] and suggest a very small contribution of strange quarks at low Q^2. It will be important to complete the world-wide parity-violation program and provide a detailed picture of the $s\bar{s}$ contributions to nucleon structure at various distances scales, thus placing constraints on theoretical models of non-perturbative QCD. In the future, probably 2008, the HAPPEx collaboration will perform the HAPPEx-III experiment at $Q^2 \sim 0.6$ GeV^2 where there was a "hint" of non-zero strangeness from the G0 experiment forward-angle run [44]. The parity-violation method will also be applied to other physics topics, in particular to Standard Model tests [45] and to PREx [46]. PREx is a high-precision measurements of the neutron RMS radius in a heavy nucleus (^{208}Pb). PREx has generated considerable interest outside the JLab community, especially from neutron star astrophysics.

3.5 E00-007

Deuteron Photodisintegration

R. Gilman, R. Holt and Z.-E. Meziani, spokespersons,
and
the Hall A Collaboration

Experiment E00-007 ran in Hall A during October, 2002. The experiment was analyzed by X. Jiang of Rutgers University. The goal of E00-007 was to measure an angular distribution of the recoil proton polarization observables in deuteron photodisintegration at $E_\gamma = 2$ GeV. The measurement is the latest in a series of deuteron photodisintegration measurements, testing the idea that this exclusive reaction, at large c.m. energy and high four-momentum transfer, is best described by models based on quark-gluon, rather than hadronic, degrees of freedom. It follows directly our previous measurements [47] of the recoil polarizations at $\theta_{c.m.} = 90°$, that were performed for E_γ up to 2.4 GeV. E00-007 is, in fact, the only measurement of polariation observables at angles $\theta_{c.m.} \neq 90°$ and significantly above 1 GeV.

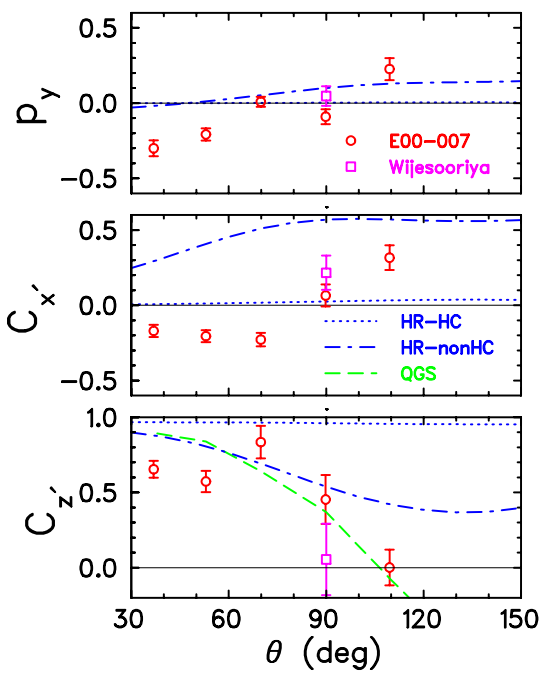

Figure 30: Angular distributions for all three recoil proton polarization components in deuteron photodisintegration, for $E_\gamma = 2$ GeV. See text for details.

The analysis of E00-007 is now complete, and an article has been submitted [48] to Phys. Rev. Lett. The basic physics results are shown in Fig. 30. First, the new

results, labelled E00-007, at $E_\gamma \approx 2$ GeV, agree reasonably with the earlier work, labelled Wijesooriya, at $E_\gamma = 1.86$ GeV. A slow energy dependence of the recoil polarization above $E_\gamma \approx 1$ GeV was found in [47], so the difference in energies is likely not too important. All three polarization components are consistent with a smooth variation with angle, and with zero-crossing near $\theta_{cm} = 90°$. As p_y and $C_{x'}$ do not generally vanish, we again confirm that hadron helicity conservation is violated.

Because the longitudinal polarization results from a sum and difference of squared amplitudes, it is insensitive to phases. Thus, it can be predicted as reliably as the cross section. In contrast, $C_{x'}$ and p_y are the real and imaginary parts of the same sum of interfering amplitudes [49,50], and are highly sensitive to phases, and thus more difficult to predict.

Two calculations of the spin observables are available. Figure 30 shows that the quark-gluon string (QGS) model [51] predicts a longitudinal polarization transfer in good qualitative agreement with the measured data, but makes no prediction for the transverse polarizations, due to their sensitivity to phases. Given the good agreement with deuteron photodisintegration cross-section data in the few GeV region [53], the QGS model must be regarded as the most successful existing model of photodisintegration at a few GeV.

Figure 30 also shows predictions for all three observables from the hard rescattering (HR) model [52]. One calculation (dotted line) assumes that there is only a small helicity non-conservation, leading to small values of $C_{x'}$ and p_y, and $C_{z'}$ being nearly unity[1]. The second (dash-dot line) calculation assumes a large helicity non-conservation. The data support a large helicity non-conservation, but clearly the predictions for the transverse polarization are not adequate.

More insight into what is happening in the transverse polarization comes from the discussion of the HR model in ref. [52]. It is pointed out that the transverse polarization components are approximately proportional to a particular amplitude in pn scattering ("ϕ_5") that vanishes at $\theta_{cm} = 90°$ in the isovector channel. Thus, the transverse polarization data might be indicating that the isovector channel dominates over the isoscalar channel, more so than in the calculation. This observation is consistent with the situation in the Σ asymmetry [51], for which the helicity conserving limit depends on the amount of isoscalar vs. isovector nature of the high-energy photon coupling. At $\theta_{cm} = 90°$, in the isoscalar limit, $\Sigma \rightarrow$ -1, while in the isovector limit, $\Sigma \rightarrow 1$. All data above $\sim$1 GeV are consistent with $\Sigma \approx 0.3$. Taken together, the recoil polarizations and Σ asymmetry might be indicating that the high-energy photon coupling is predominantly isovector. In the QGS model, the isoscalar–isovector interference also leads to a dip in the forward-angle ($\theta_{cm} \leq 30°$) cross section, that is suggested, although not clearly

[1]Helicity conservation leads to $C_{x'}$ and p_y vanishing, but the limit for $C_{z'}$ is model dependent. In the HR model, the helicity-conserving amplitude $F_{1+} \geq F_{5\pm}$, while F_{3-} is small, as a + helicity photon scatters from a + helicity proton. The limit is *not* the same as the usual one presented in [50], which assumes $F_{1+} \approx F_{3-}$

proven, by the extensive angular distributions from Hall B CLAS [53].

While the HR model does not agree quite as well as the QGS model with $C_{z'}$ or with the cross section for energies around 2 GeV, it is at least as successful at predicting the cross section above about 3 GeV [50], and its p_y predictions are consistent with the large-angle data.

To summarize, the two models which predict the longitudinal polarization transfer, the QGS and HR models, are in qualitative agreement with these data; while neither model adequately explains the transverse polarization components, the HR model indicates the qualitative behavior might arise from isovector dominance. High-energy photodisintegration of pp pairs [54] is the next major test of the underlying dynamics and of the theoretical models, as these two models give very different predictions for pp photodisintegration. Future experiments to determine the Σ asymmetry and to clearly demonstrate the dip in the forward-angle cross section also would help to clarify the underlying dynamics of deuteron photodisintegration.

3.6 E00-102

Testing the Limits of the Single-Particle Model in ^{16}O$(e, e'p)$

A. Saha, W. Bertozzi, L.B. Weinstein, and K. Fissum, spokespersons,
and
the Hall A Collaboration

Experiment E00-102 is an update to Hall A experiment E89-003: Measurement of the cross section, R_{LT}, and A_{LT} for the ^{16}O$(e, e'p)$ reaction. Experiment E89-003 made measurements at energy and momentum transfer of $\omega = 0.445$ GeV and $Q^2 = 0.8$ GeV^2 respectively, up to a missing momentum of $p_m = 0.345$ GeV/c [55–57]. This update experiment expands these measurements up to $p_m = 0.755$ GeV/c at $\omega = 0.449$ GeV and $Q^2 = 0.902$ GeV^2. The goals of these measurements are to determine:

- the limits of validity of the single-particle model of valence-proton knockout;
- the effects of relativity and spinor distortion on valence-proton knockout using the diffractive character of the A_{LT} asymmetry; and
- the bound-state wave function and spectroscopic factors for valence knockout.

The cross section will be determined for measurements from $p_m = -0.515$ GeV/c to $p_m = +0.755$ GeV/c, in order to determine the point at which single-knockout calculations fail and two-nucleon effects become important. R_{LT} and A_{LT} will be separated for p_m up to ± 0.515 GeV/c to further test the relativistic DWIA calculations. Figure 31 shows anticipated data points from E00-102 for A_{LT} as a function of missing momentum for the $1p$-shell states along with data obtained from E89-003, both compared to calculations from Udias *et al.*

Data were taken at a fixed beam energy of 4.620 GeV, $|\vec{q}| = 1.066$ GeV/c, and $\theta_q = 56.22°$. Throughout the entire experiment, the electron arm (HRS-L) was fixed at 12.5° with a central momentum of 4.121 GeV/c, allowing it to be used as a luminosity monitor. The hadron arm (HRS-R) angle was varied from 28.3° to 96.1° to cover the necessary missing-momentum range. These kinematics are shown in Fig. 32.

Both detector stacks were used in their standard configurations. Each stack contained an additional S0 scintillator for checking trigger efficiency, and the HRS-L contained a pion rejector, used for e^-/π^- separation. The target used was the Hall A self-normalizing three-foil waterfall target [58,59]. Each water foil was approximately 200 mg/cm^2 thick and separated by 25.4 mm. The foils were rotated to an angle of 57.4° with respect to the beam direction, as shown in Fig. 33. Using the hydrogen in the water, precise calibrations can be made as well as a normalization of the cross section to the known ^{1}H$(e, e'p)$ and ^{1}H(e, e') cross sections.

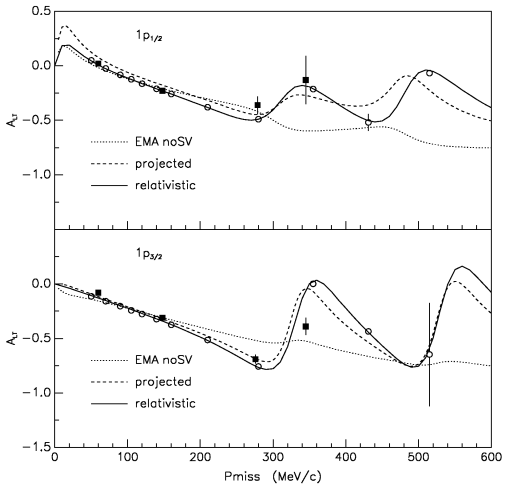

Figure 31: Projected A_{LT} data compared to E89-003 results and calculations of Udias *et al.* Open circles are anticipated data points from E00-102, solid squares are E89-003 data obtained at slightly different kinematics.

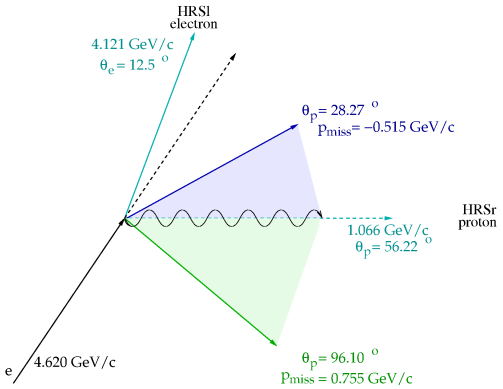

Figure 32: E00-102 kinematics. The beam energy was fixed at 4.620 GeV, and the HRS-L remained fixed at 12.5° with a central momentum of 4.121 GeV/c. The HRS-R was varied around the direction of parallel kinematics to cover the necessary missing-momentum range.

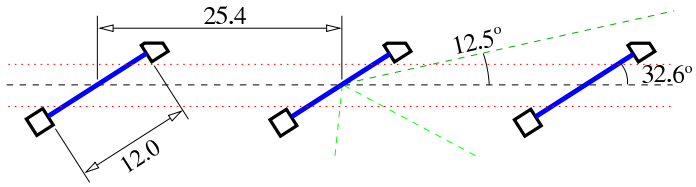

Figure 33: E00-102: E00-102 waterfall target

Detector calibrations, beam-position and beam-energy calibrations have been performed. Optimized detector maps have been created, and the data have been replayed using ESPACE. Analysis of the spectrometer mispointing has been performed. The water foil thicknesses have been determined by comparison of ^{16}O$(e, e'p)$ yields to a BeO target of known thickness, and a preliminary comparison of measured ^{1}H$(e, e'p)$ yields to simulations have been made. An analysis of the electronic dead-time measurement is in progress.

In the past year, extensive progress has been made at ODU in adapting the ROOT/C++ analyzer to the E00-102 analysis. The ESPACE optics calibration database has been transferred to the new format, and tested extensively to demonstrate agreement between ESPACE and the analyzer. A model of the waterfall target has been built into the analyzer to calculate energy-loss corrections. The three-foil target was not supported in ESPACE. The C++ analyzer was written for a more modern configuration of the coincidence trigger logic, so a new coincidence-time module was written for the analyzer. Results comparable in quality to ESPACE are obtained, and are illustrated in Fig. 34. The LeRose R-functions were added to the analyzer, giving a new option for detector acceptance cuts and acceptance matching between data and and simulations. The C++ analyzer's superior handling of multi-track events will provide additional insights into the determination of the electronic dead time.

Lund University, in collaboration with Madrid, has integrated the Udias RDWIA model [60,61] into the MCEEP simulation. An interpolatable hyper-cube containing the results of the Udias calculation over a broad range of kinematics was generated and used to weight the MCEEP events. This allows the calculation to be correctly averaged over the finite acceptance of the spectrometers. An in-depth comparison of the MCEEP output and the results of the previous oxygen experiment (E89-003) has been performed.

In Fig. 35, the simulated longitudinal-transverse asymmetry A_{LT} for the removal of $1p1/2$-state protons from ^{16}O in E89-003 kinematics is presented. Experimental cuts have been applied to the simulated data. Open red boxes result from the simulations, each box representing a particular (ω, q, p_m) bin. In the top panel, the results of the simulations for the E89-003 acceptances considered

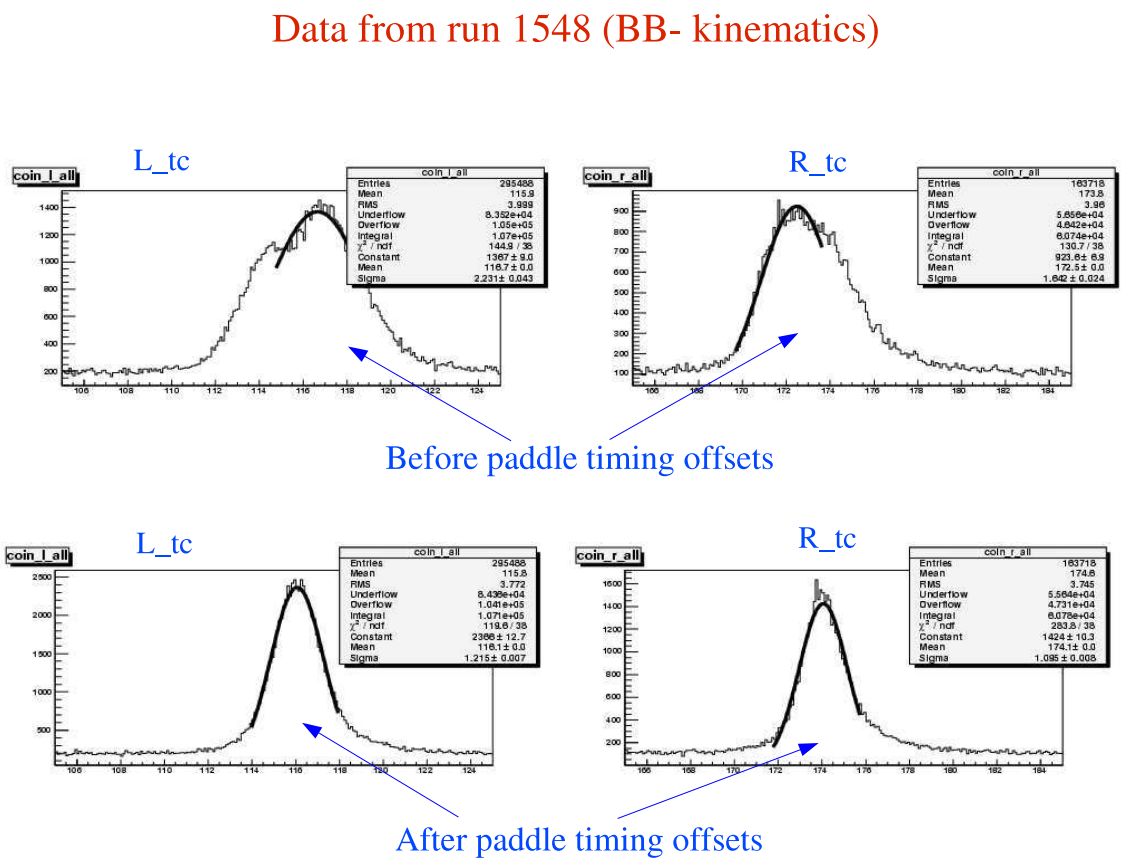

Figure 34: E00-102: Coincidence-time spectra from the Root/C++ analyzer before and after the construction of the specialized E00-012 coincidence timing code.

in the data analysis are shown. The blue circles represent the average of the A_{LT} values over all of the red (ω, q, p_m) bins corresponding to a given kinematics. It is clear that the averaged simulated A_{LT} values agree reasonably well with the published data. In the bottom panel, the p_m evolution of the results corresponding to "extremely reduced" spectrometer acceptances: ± 0.1 mrad for spectrometer angles and $\pm 0.1\%$ for the electron and ejected proton momenta is shown. It can be noted that, as the acceptances are reduced, the simulated results collapse to the point-acceptance RDWIA calculations.

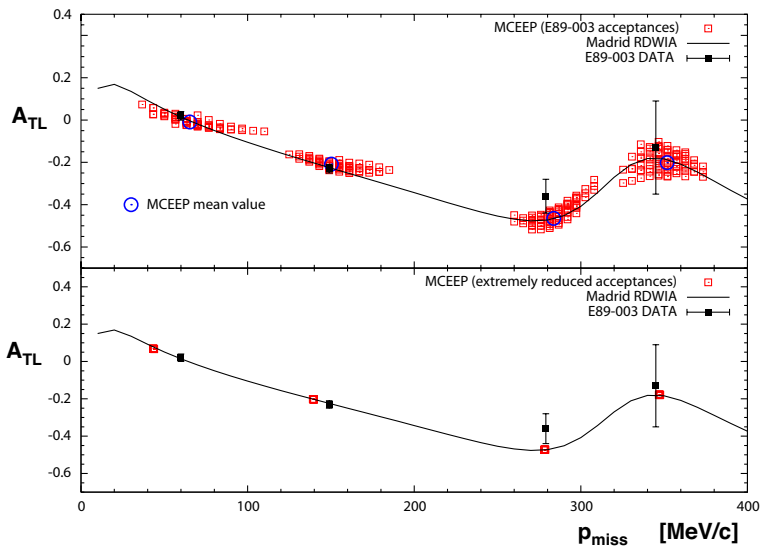

Figure 35: Selected results from the Lund/Madrid MCEEP simulations.

With the recent improvements in the analysis and simulation tools, full scale data analysis is ready to begin. Absolute $(e, e'p)$ cross-section values, along with R_{LT} and A_{LT} on ^{16}O will be extracted.

3.7 E00-110

Deeply Virtual Compton Scattering at 6 GeV

C.E. Hyde-Wright, P.-Y. Bertin, R. Ransome and F. Sabatié, spokespersons,
and
the Hall A Collaboration

3.7.1 Deeply Virtual Compton Scattering Experiment

We have measured the helicity-dependent cross section for the $\vec{e}p \to e\gamma p$ reaction in the kinematics of Table 4. We have also completed the analysis of the helicity-independent cross section for Kin-3. QCD factorization theorems [62,63] predict that at sufficiently high Q^2, these reactions can be described by a new class of quark and gluon matrix elements of the target, called Generalized Parton Distributions (GPDs) [64–66]. The GPDs relate the spatial and momentum distributions of a parton in the proton. Extracting GPDs from DVCS requires the fundamental demonstration that DVCS is well described by the twist-2 diagram of Fig. 36 (and its interference with the BH amplitude). In [67] we report strong evidence for this cornerstone hypothesis.

Kin	k' (GeV/c)	θ_e (°)	Q^2 (GeV^2)	$x_{\rm Bj}$	θ_q (°)	W (GeV)	E_γ (GeV)
1	3.53	15.6	1.5	0.36	−22.3	1.9	2.14
2	2.94	19.3	1.9	0.36	−18.3	2.0	2.73
3	2.34	23.8	2.3	0.36	−14.8	2.2	3.33

Table 4: Experimental $ep \to ep\gamma$ kinematics, for incident beam energy $E = 5.75$ GeV. θ_q is the central value of the $\mathbf{q}$-vector direction. The PbF_2 calorimeter was centered on θ_q for each setting. The photon energy for $\mathbf{q}' \parallel \mathbf{q}$ is E_γ.

The E00-110 experiment ran with the 5.75 GeV electrons incident on a 15 cm long liquid H_2 target. Our typical luminosity was 10^{37}/cm^2/s with a 76% beam polarization. We detected the scattered electrons in one High Resolution Spectrometer (HRS). Photons above a 1 GeV energy threshold (and $\gamma\gamma$ coincidences from π^0 decay) were detected in a 11×12 array of $3 \times 3 \times 18.6$ cm^3 PbF_2 crystals, whose front face was located 110 cm from the target center. We calibrated the PbF_2 array by coincident elastic $H(e, e'_{\rm Calo} p_{\rm HRS})$ data. With (elastic) $k' = 4.2$ GeV/c, we obtain a PbF_2 resolution of 2.4% in energy and 2 mm in transverse position (one-σ). The calibration was monitored during the experiment by reconstruction of the $\pi^0 \to \gamma\gamma$ mass from $H(e, e'\pi^0)X$ events.

We present in Fig. 37 the missing mass squared obtained for $H(e, e'\gamma)X$ events, with coincident electron-photon detection. After subtraction of an accidental

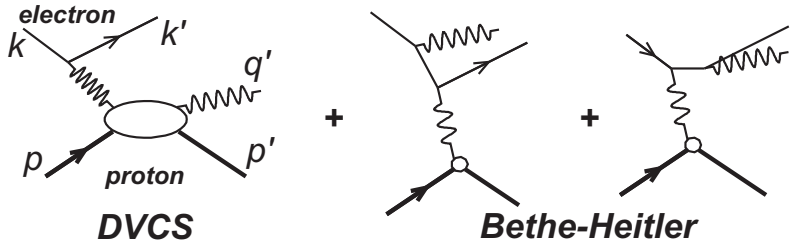

Figure 36: Lowest-order QED diagrams for the process $ep \to ep\gamma$, including the DVCS and Bethe-Heitler (BH) amplitudes. The external momentum four-vectors are defined on the diagram. The virtual photon momenta are $q = k - k'$ in the DVCS- and $\Delta = q - q'$ in the BH-amplitudes. The invariants are: $W^2 = (q+p)^2$, $Q^2 = -q^2 > 0$, $t = \Delta^2$, $x_{\rm Bj} = Q^2/(2p \cdot q)$, and the DVCS scaling variable $\xi = -\overline{q}^2/(\overline{q} \cdot P) \approx x_{\rm Bj}/(2 - x_{\rm Bj})$, with $\overline{q} = (q+q')/2$ and $P = p + p'$.

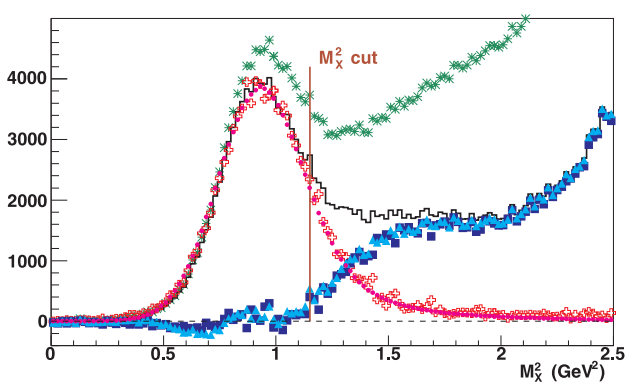

Figure 37: Missing mass squared for $\mathrm{H}(e,e'\gamma)X$ events (stars) at $Q^2 = 2.3$ GeV^2 and $-t \in [0.12, 0.4]$ GeV^2. The solid histogram shows the data once the $\mathrm{H}(e,e'\gamma)\gamma X'$ events have been subtracted. The other histograms are described in the text.

coincidence sample, we have the following competing channels in addition to $\mathrm{H}(e,e'\gamma)p$: $ep \to e\pi^0 p$, $ep \to e\pi^0 N\pi$, $ep \to e\gamma N\pi$, $ep \to e\gamma N\pi\pi \ldots$. From symmetric (lab-frame) π^0-decay, we obtain a high-statistics sample of $\mathrm{H}(e,e'\pi^0)X'$ events, with two-photon clusters in the $\mathrm{PbF_2}$ calorimeter. From these events, we determine the statistical sample of [asymmetric] $\mathrm{H}(e,e'\gamma)\gamma X'$ events that must be present in our $\mathrm{H}(e,e'\gamma)X$ data. The solid M_X^2 spectrum displayed in Fig. 37 was obtained after subtracting this π^0 yield from the total (stars) distribution. This is a 14% average subtraction in the exclusive window defined by 'M_X^2 cut' in Fig. 37. Depending on the bin in $\phi_{\gamma\gamma}$ and t, this subtraction varies from 6% to 29%. After our π^0 subtraction, the only remaining channels, of type $\mathrm{H}(e,e'\gamma)N\pi$, $N\pi\pi$, *etc.* are kinematically constrained to $M_X^2 > (M + m_\pi)^2$. This is the value ('M_X^2 cut' in Fig. 37) we chose for truncating our integration. Resolution effects can cause the inclusive channels to contribute below this cut. To evaluate this possible contamination, we used an additional proton array (PA) of 100 plastic scintillators. For $\mathrm{H}(e,e'\gamma)X$ events near the exclusive region, we can predict which block in the PA

should have a signal from a proton from an exclusive $\mathrm{H}(e, e'\gamma p)$ event. Open red crosses show the $X = (p + y)$ missing mass squared distribution for $\mathrm{H}(e, e'\gamma p)y$ events in the predicted PA block, with a signal above an effective threshold 30 MeV (electron equivalent). Black squares shows our inclusive yield, obtained by subtracting the normalized triple coincidence yield from the $\mathrm{H}(e, e'\gamma)X$ yield. The dotted curve shows our simulated $\mathrm{H}(e, e'\gamma)p$ spectrum, including radiative and resolution effects, normalized to fit the data for $M_X^2 \leq M^2$. Blue triangles show the estimated inclusive yield obtained by subtracting the simulation from the data. The black squares and the blue triangles are in good agreement, and show that our exclusive yield has less than 3% contamination from inclusive processes.

3.7.2 GPDs and the DVCS Cross Sections

To order twist-3 the DVCS helicity-dependent ($d\Sigma$) and helicity-independent ($d\sigma$) cross sections are given by [69]:

$$\begin{aligned}
\frac{d^4\Sigma}{d^4\Phi} &= \frac{1}{2}\left[\frac{d^4\sigma^+}{d^4\Phi} - \frac{d^4\sigma^-}{d^4\Phi}\right] = \frac{d^4\Sigma(|DVCS|^2)}{d^4\Phi} \qquad (9)\\
&+ \sin(\phi_{\gamma\gamma})\Gamma_1^{\Im}\,\Im\mathrm{m}\left[\mathcal{C}^I(\mathcal{F})\right] - \sin(2\phi_{\gamma\gamma})\Gamma_2^{\Im}\,\Im\mathrm{m}\left[\mathcal{C}^I(\mathcal{F}^{\mathrm{eff}})\right],\\
\frac{d^4\sigma}{d^4\Phi} &= \frac{1}{2}\left[\frac{d^4\sigma^+}{d^4\Phi} + \frac{d^4\sigma^-}{d^4\Phi}\right] = \frac{d^4\sigma(|DVCS|^2)}{d^4\Phi} \qquad (10)\\
&+ \frac{d^4\sigma(|BH|^2)}{d^4\Phi} + \Gamma_{0,\Delta}^{\Re}\,\Re\mathrm{e}\left[\mathcal{C}^I + \Delta\mathcal{C}^I\right](\mathcal{F})\\
&+ \Gamma_0^{\Re}\Re\mathrm{e}\left[\mathcal{C}^I(\mathcal{F})\right] - \cos(\phi_{\gamma\gamma})\Gamma_1^{\Re}\Re\mathrm{e}\left[\mathcal{C}^I(\mathcal{F})\right] + \cos(2\phi_{\gamma\gamma})\Gamma_2^{\Re}\Re\mathrm{e}\left[\mathcal{C}^I(\mathcal{F}^{\mathrm{eff}})\right],
\end{aligned}$$

where $d^4\Phi = dQ^2 dx_{\mathrm{Bj}} dt d\phi_{\gamma\gamma}$ and the azimutal angle $\phi_{\gamma\gamma}$ of the detected photon follows the "Trento-Convention" [68]. The $\Gamma_n^{\Re,\Im}$ are kinematic factors with a $\phi_{\gamma\gamma}$ dependence that arises from the electron propagators of the BH amplitude. The $\mathcal{C}^I$ and $\Delta\mathcal{C}^I$ angular harmonics depend on the interference of the BH amplitude with the set $\mathcal{F} = \{\mathcal{H}, \mathcal{E}, \tilde{\mathcal{H}}, \tilde{\mathcal{E}}\}$ of twist-2 Compton form factors (CFFs) or the related set $\mathcal{F}^{\mathrm{eff}}$ of effective twist-3 CFFs:

$$\mathcal{C}^I(\mathcal{F}) = F_1\mathcal{H} + \xi G_M\tilde{\mathcal{H}} - \frac{t}{4M^2}F_2\mathcal{E} \qquad (11)$$

$$\left[\mathcal{C}^I + \Delta\mathcal{C}^I\right](\mathcal{F}) = F_1\mathcal{H} - \frac{t}{4M^2}F_2\mathcal{E} - \xi^2 G_M\left[\mathcal{H} + \mathcal{E}\right]. \qquad (12)$$

The CFFs are defined in terms of the GPDs H_f, E_f, $\tilde{H}_f$,and $\tilde{E}_f$, defined for each quark flavor f:

$$\begin{aligned}
\mathcal{H}(\xi,t) &= \sum_f \left[\frac{e_f}{e}\right]^2 \Bigg\{ i\pi\left[H_f(\xi,\xi,t) - H_f(-\xi,\xi,t)\right]\\
&+ \mathcal{P}\int_{-1}^{+1} dx \left[\frac{2x}{\xi^2 - x^2}\right] H_f(x,\xi,t)\Bigg\}. \qquad (13)
\end{aligned}$$

On the one hand, $d\Sigma$ measures the imaginary part of the BH-DVCS interference terms and provides direct access to GPDs at $x = \xi$. On the other hand, $d\sigma$ determines the real part of the BH-DVCS interference terms and measures the integral of GPDs over its full domain in x.

We neglect the DVCS^2 terms in our analysis. Therefore, our experimental results for $\Im\mathrm{m}[\mathcal{C}^{\mathcal{I}}]$ and $\Re\mathrm{e}[\mathcal{C}^{\mathcal{I}}]$ may contain, respectively, twist-3 and twist-2 DVCS^2 terms, which enter with similar $\sin\phi_{\gamma\gamma}$ and $\cos\phi_{\gamma\gamma}$ dependence. However, the DVCS^2 term in $d\Sigma$ is kinematically suppressed by at least an order of magnitude in our kinematics [69], because it is not enhanced by the BH amplitude. We have submitted proposal PR07-007 to PAC31 to determine the contribution of the DVCS^2 terms in $d\sigma$, by performing measurements at two different beam energies. In any case, the terms we neglect do not affect the cross sections we extract, which are accurately parametrized, within statistics, by the contributions we included.

3.7.3 Simulation and Analysis

Our simulation includes internal bremsstrahlung in the scattering process and external bremsstrahlung and ionization straggling in the target and scattering chamber windows. We include spectrometer resolution and acceptance effects and a full GEANT3 simulation of the detector response to the DVCS photons and protons. Radiative corrections for virtual photons and unresolved real photons are applied according to the VCS (BH+Born amplitude) specific prescriptions of Ref. [70].

For each $(Q^2, x_{\mathrm{Bj}}, t)$ bin, we fit the $\Re\mathrm{e}$ and $\Im\mathrm{m}$ parts (as appropriate) of the harmonics $\mathcal{C}_n \in \{\mathcal{C}^{\mathcal{I}}(\mathcal{F}), \mathcal{C}^{\mathcal{I}}(\mathcal{F}^{\mathrm{eff}}), \left[\mathcal{C}^{\mathcal{I}} + \Delta\mathcal{C}^{\mathcal{I}}\right](\mathcal{F})\}$ as independent parameters. In Kin-1 and Kin-2, due to the lower photon energy E_γ (Table 4), our acceptance, trigger, and read out did not record a comprehensive set of $ep \to e\pi^0 X$ events. For those events we were able to reconstruct, we found only a few percent contribution to $d\Sigma$, but a larger contribution to $d\sigma$. Therefore, for Kin-1,2, we only extract results on $d\Sigma$. In PR07-007, we will upgrade the calorimeter and trigger, so that we can measure the π^0 yield and the unpolarized DVCS cross section in all kinematics.

3.7.4 DVCS Results

For one $(Q^2, x_{\mathrm{Bj}}, t)$ bin, Fig. 38 shows the helicity-dependent and helicity-independent cross sections, respectively. We notice that the twist-3 terms make only a very small contribution to the cross sections. Note also that the helicity-independent cross section is much larger than the BH contribution alone, especially from 90° to 270°. This indicates that the relative Beam Spin Asymmetry $BSA = d^4\Sigma/d^4\sigma$ cannot be simply equated to the imaginary part of the BH-DVCS interference divided by the BH cross section. Figure 39 (Left) shows the Q^2 dependence of the imaginary angular harmonic $\Im\mathrm{m}[\mathcal{C}^{\mathcal{I}}]$ over our full t domain, with $\langle t\rangle = -0.25$ GeV^2

($\langle t \rangle$ varying by ± 0.01 GeV^2 over Kin 1–3).

The absence of Q^2 dependence of $\Im\mathrm{m}[\mathcal{C}^{\mathcal{I}}(\mathcal{F})]$ within its 3% statistical uncertainty provides crucial support to the dominance of twist-2 in the DVCS amplitude. $\Im\mathrm{m}[\mathcal{C}^{\mathcal{I}}(\mathcal{F})]$ is thereby a direct measurement of the linear combination of GPDs. The acceptance-averaged ratios of the kinematic coefficients of the bilinear DVCS terms to the BH-DVCS terms are below 1.2% for $d\Sigma$ and below 4.5% for $d\sigma$.

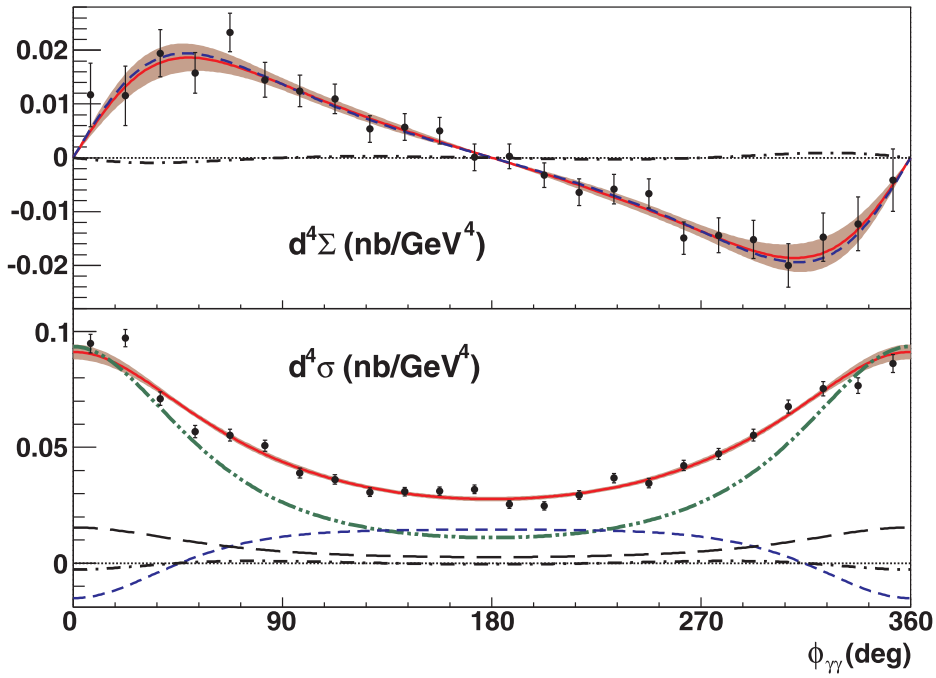

Figure 38: Data and fit to $d^4\Sigma/dQ^2dx_{\mathrm{Bj}}dtd\phi_{\gamma\gamma}$, and $d^4\sigma/[dQ^2dx_{\mathrm{Bj}}dtd\phi_{\gamma\gamma}]$, as a function of $\phi_{\gamma\gamma}$. Both are in the bin $\langle Q^2, t\rangle = (2.3, -0.28)$ GeV^2 at $\langle x_{\mathrm{Bj}}\rangle = 0.36$. Error bars show statistical uncertainties. Red solid lines show total fits with one-σ statistical error bands. The systematic uncertainty is given in the text. The green dot-dot-dashed line is the $|\mathrm{BH}|^2$ contribution to $d^4\sigma$. The short-dashed lines in $d^4\Sigma$ and $d^4\sigma$ are the contributions from the fitted $\Im\mathrm{m}$ and $\Re\mathrm{e}$ parts of $\mathcal{C}^{\mathcal{I}}(\mathcal{F})$, respectively. The long-dashed line is the fitted $\Re\mathrm{e}[\mathcal{C}^{\mathcal{I}} + \Delta\mathcal{C}^{\mathcal{I}}](\mathcal{F})$ term. The dot-dashed curves are the fitted $\Im\mathrm{m}$ and $\Re\mathrm{e}$ parts of $\mathcal{C}^{\mathcal{I}}(\mathcal{F}^{\mathrm{eff}})$.

Figure 39 (Right) displays the twist-2 $\mathcal{C}$ angular harmonics ($\Re\mathrm{e}$ and $\Im\mathrm{m}$ parts) as functions of t, together with the VGG model estimates [71–73]. The VGG model is in qualitative agreement with the $\Im\mathrm{m}[\mathcal{C}^{\mathcal{I}}(\mathcal{F})]$ data, but significantly underpredicts the principal-value integrals ($\Re\mathrm{e}$ parts of the angular harmonics).

We have obtained the first explicit demonstration of exclusivity in DVCS kinematics. These results are the first measurements of DVCS cross sections in the

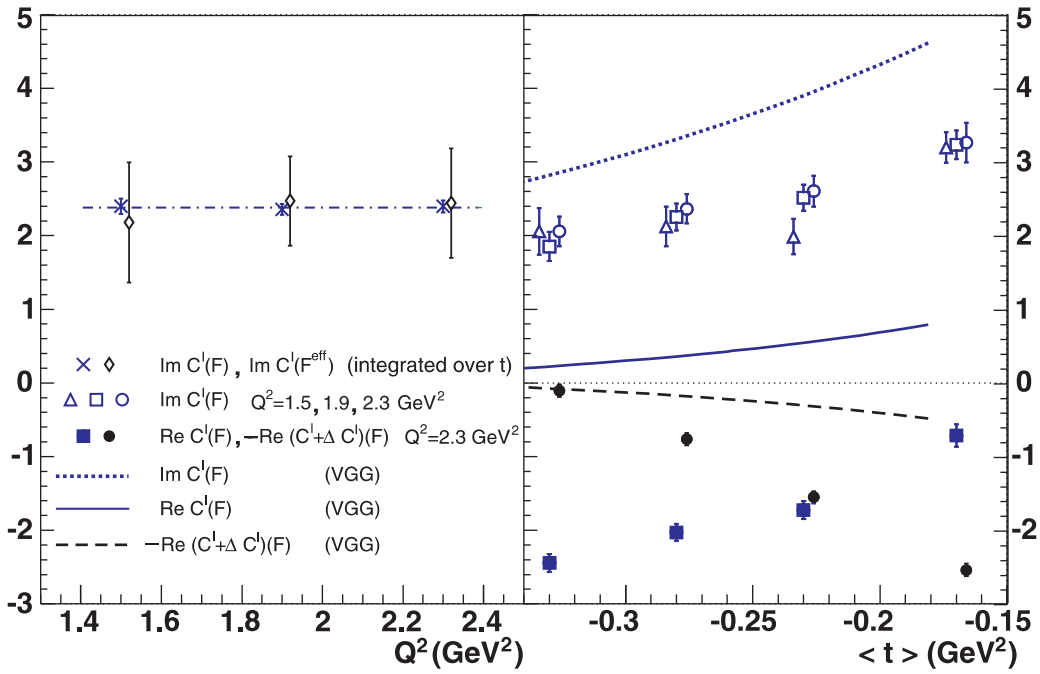

Figure 39: Left: Q^2 dependence of $\Im$m parts of (twist-2) $\mathcal{C}^{\mathcal{I}}(\mathcal{F})$ and (twist-3) $\mathcal{C}^{\mathcal{I}}(\mathcal{F}^{\text{eff}})$ angular harmonics, averaged over t. The horizontal line is the fitted average of $\Im\text{m}[\mathcal{C}^{\mathcal{I}}(\mathcal{F})]$. Right: Extracted real and imaginary parts of the twist-2 angular harmonics as functions of t. Their error bars show statistical uncertainties.

valence quark region. From the Q^2 dependence of the angular harmonics of the helicity-dependent cross section, we provide solid evidence of twist-2 dominance in DVCS, which makes GPDs accessible to experiment even at modest Q^2. This result supports the striking prediction of perturbative QCD scaling in DVCS [64,66]. As a consequence of this evidence for scaling in the exclusive channel, and our separate determination of the helicity-dependent and helicity-independent cross sections, we extract for the first time a model-independent combination of GPDs and GPDs integrals.

3.7.5 Deeply Virtual π^0 Production

We expect to finalize our analysis of $\text{H}(\vec{e}, e'\pi^0)p$ at $Q^2 = 2.3$ GeV^2 in early 2007, and submit the results for publication.

3.8 E01-012

Measurement of neutron (^{3}He) spin structure functions in the resonance region

J. P. Chen, S. Choi and N. Liyanage, spokespersons,
and
the Hall A Collaboration

Experiment E01-012 ran in January and February, 2003. The goal of this experiment is to perform a precision extraction of the neutron spin structure function g_1^n and the virtual photon asymmetry A_1^n in the resonance region over a moderate Q^2 range (up to $Q^2 = 4$ GeV^2) using the Hall A polarized ^{3}He target. The results from this experiment, combined with deep-inelastic scattering data, provides a test of quark-hadron (Bloom-Gilman) duality predictions for the neutron spin structure function g_1^n and the virtual-photon asymmetry A_1^n. The Bloom-Gilman duality has been experimentally demonstrated for the spin-independent structure function F_2. Duality is observed when the smooth scaling curve at high momentum transfer is an average over the resonance bumps at lower momentum transfer, but at the same value of the scaling variable x_B. Results from E01-012 enable one of the first precision tests of the spin and flavor dependence of quark-hadron duality. The demonstration of duality for spin structure functions will enable the use of resonance data to study the nucleon spin structure in the very high x_B region.

In this experiment we used the polarized beam and the polarized ^{3}He target to measure the inclusive $^3\vec{\mathrm{He}}(\vec{e}, e')X$ reaction. Both Hall A High Resolution spectrometers (HRS) were used in a symmetric configuration in electron detection mode. Three beam energies, 3 GeV, 4 GeV and 5 GeV were used with spectrometer angles of 25° and 32°. At each kinematic setting parallel and perpendicular asymmetries were measured with the target spin parallel and perpendicular to the electron beam, respectively.

We formed the polarized cross-section differences, $\Delta\sigma_{\parallel(\perp)}$ corresponding to the target spin aligned parallel (perpendicular) to the beam helicity. From these quantities, the spin-dependent structure functions g_1 and g_2 were extracted. External and internal radiative corrections have been applied to the polarized cross-section differences following the formalism of Mo and Tsai [74] for the spin-independent part of the radiative corrections and Akushevich and Shumeiko [75] for the spin-dependent part.

So far the physical quantities generated are at fixed energies and scattering angles. In order to form the partial first moment of g_1, interpolation to constant Q^2 is performed. The results of g_1 for ^{3}He are shown in Fig. 40 at the four interpolated Q^2 values of 1.2, 1.8, 2.4 and 3.0 GeV^2. Also plotted is the DIS parametrization evolved down to our Q^2 from the GRSV group [76].

In order to test global duality [77], the integral of g_1 over the resonance region is evaluated. The DIS parametrization has been evolved down to our Q^2 and

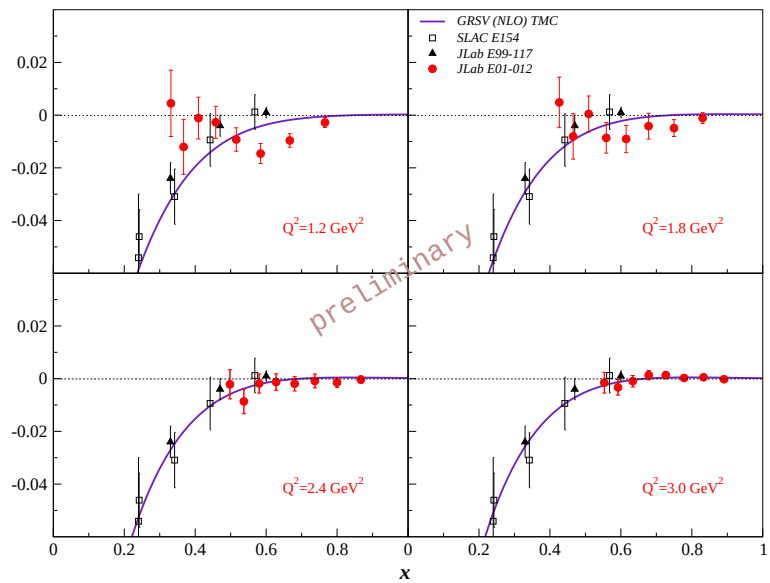

Figure 40: The spin structure function $g_1^{^3\mathrm{He}}$ in the resonance region at Q^2 of 1.2, 1.9, 2.6 and 3.3 GeV^2. The curve was generated from the GRSV NLO parton distribution functions [76].

integrated over the same x-range. Moreover, target-mass corrections have been applied to the DIS parametrization to take into account the finite mass of the target [78].

The neutron integral was evaluated using the method of Ref. [79]:

$$\tilde{\Gamma}_1^{^3\mathrm{He}} = P_n \tilde{\Gamma}_1^n + 2.0 P_p \tilde{\Gamma}_1^p \tag{14}$$

where $P_n = 0.86$ and $P_p = -0.028$ are the respective effective polarization of the neutron and the proton in ^{3}He [80]. The integral of the proton spin structure function g_1^p was extracted from the CLAS eg1b data [81]. Figures 41 and 42 present the comparison of the integral of g_1 over the resonance region to DIS parameterizations [82,76,83] abbreviated BB, GRSV and AAC, respectively. All parameterizations were taken at Next-to-Leading Order. Target mass corrections have been applied to the DIS parameterizations. Our data are about 2σ away from the BB parametrization for our lowest and highest Q^2. However all our data agree within uncertainties with the GRSV and AAC parameterizations, considering that the parametrization should also have an error band (the uncertainties on g_1 was not given). Therefore, it appears that quark-hadron duality holds globally even down to $Q^2 = 1.2$ GeV^2.

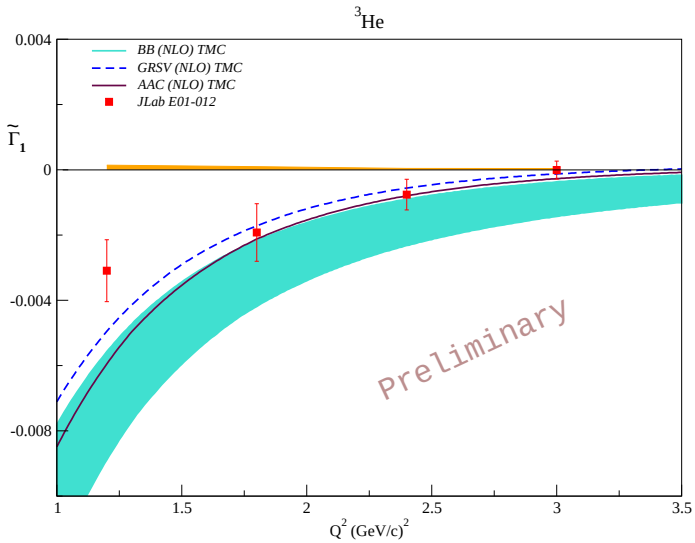

Figure 41: $\tilde{\Gamma}_1^{^3\mathrm{He}}$: test of spin duality on ^{3}He. Also plotted are the DIS parameterizations of Blumlein and Bottcher [82] (blue band), GRSV [76] (dashed curve) and AAC [83] (solid curve) after applying target-mass corrections. The orange band represents the systematic uncertainty of our data.

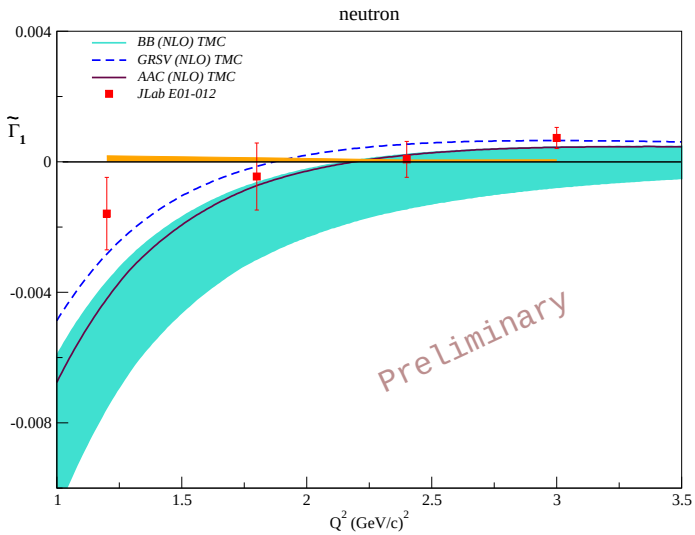

Figure 42: Same as in Fig. 41 but for $\tilde{\Gamma}_1^n$.

Quark-hadron duality was also studied through the photon-nucleon asymmetry A_1. From the parallel and perpendicular asymmetries, the virtual photon asymmetry A_1 was extracted. Figure 43 shows the preliminary results for A_1^{3He} for the four Q^2 values of this experiment. The extraction of A_1^n from $A_1^{3\mathrm{He}}$ has not been finalized yet and the results for $A_1^{3\mathrm{He}}$ are presented here. The qualitative behavior of A_1^n will be similar to the behavior of $A_1^{3\mathrm{He}}$ presented here. For the two lowest average Q^2 data, it can be seen that $A_1^{3\mathrm{He}}$ near or at the $\Delta(1232)$ peak is large and negative unlike the DIS behavior. But as the Q^2 increases, $A_1^{3\mathrm{He}}$ crosses zero and becomes positive even in the $\Delta(1232)$ region. This is due to the rise of the non-resonant background under the resonance region. Moreover the fall off of the $\Delta(1232)$ form factor reduces the strength of the $\Delta(1232)$ as Q^2 increases. Finally, the two highest Q^2 sets of resonance data follow the same trend; this is an indication that the Q^2 dependence of A_1 has weakened as expected from the DIS data. This may be the first indication of "x-scaling" for A_1^n in the resonance region.

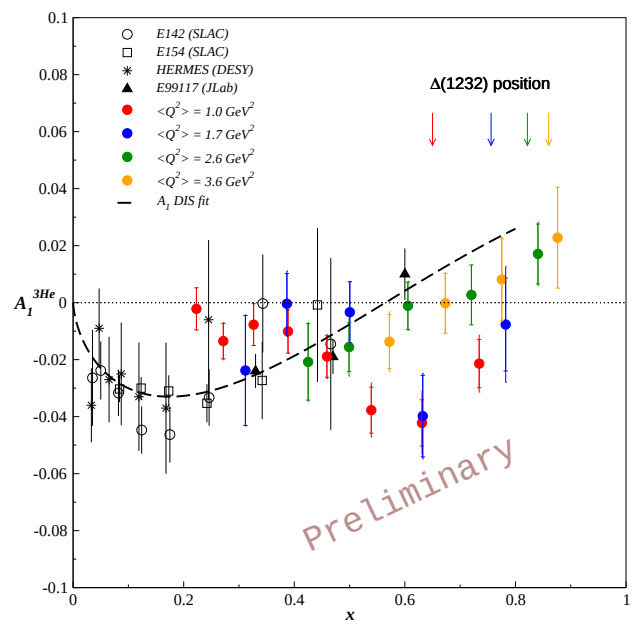

Figure 43: $A_1^{3\mathrm{He}}$ in the resonance region. DIS data are from E142, E154, HERMES and E99-117. The curve is a fit to $A_1^{3\mathrm{He}}$ DIS data.

Current Status: The analysis of the E01-012 data is almost complete; we are in the process of finalizing the results and preparing the publications.

3.9 E01-015

Studying the Internal Small-Distance Structure of Nuclei via the Triple Coincidence $(e, e'p + N)$ Measurement

W. Bertozzi, E. Piasetzky, J. Watson and S. Wood, spokespersons,
and
the Hall A Collaboration

The attractive short-range component of the nucleon-nucleon force can cause some of the protons inside a nucleus to form pairs. These pairs have a low center-of-mass momentum and a high relative momentum where low and high are relative to the Fermi sea level which is approximately 220 MeV/c. Experiment E01-015 sought to indirectly observe this effect by measuring the triple coincidence $(e, e'pn)$ and $(e, e'pp)$ events from carbon at high missing momentum.

The experiment completed data taking in April of 2005. The $^{12}C(e, e'p)$ data were taken with the two Hall A high resolution spectrometers and, for each $(e, e'p)$ event, the BigBite spectrometer and a neutron detector ADCs and TDCs were read-out. This allowed the experiment to measure the $(e, e'pn)$ and $(e, e'pp)$ channels simultaneously without having to set up a complex multi-arm triggering system. Figure 44 shows a CAD picture of the experimental set-up as well as a vector diagram of the kinematics.

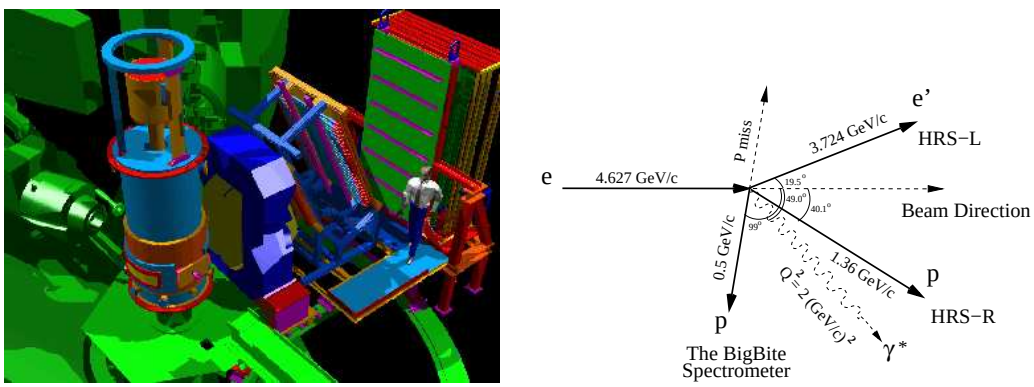

Figure 44: The left image shows a computer-aided design (CAD) drawing of the SRC experimental setup. The right image shows a vector diagram of the kinematics.

There are four Ph.D. students working on the analysis of the data. Peter Monaghan (MIT) is analyzing the ^{12}C$(e, e'p)$ reaction, Ran Shneor (Tel Aviv University) the ^{12}C$(e, e'pp)$ reaction, Ramesh Raj Subedi (Kent State University) the ^{12}C$(e, e'pn)$ reaction, and Neil Thomson (University of Glasgow) triple coincidence events where a deuteron was detected in either an HRS and/or in BigBite. The

analysis of the $(e, e'pp)$ and $(e, e'pn)$ channels is nearly complete and a draft of a paper of the $(e, e'pp)$ results which will be submitted to Phys. Rev. Lett., is in circulation. The principle result of this paper, which presents the ratio of $(e, e'pp)$ to $(e, e'p)$ events at high missing momentum, is shown in Fig. 45.

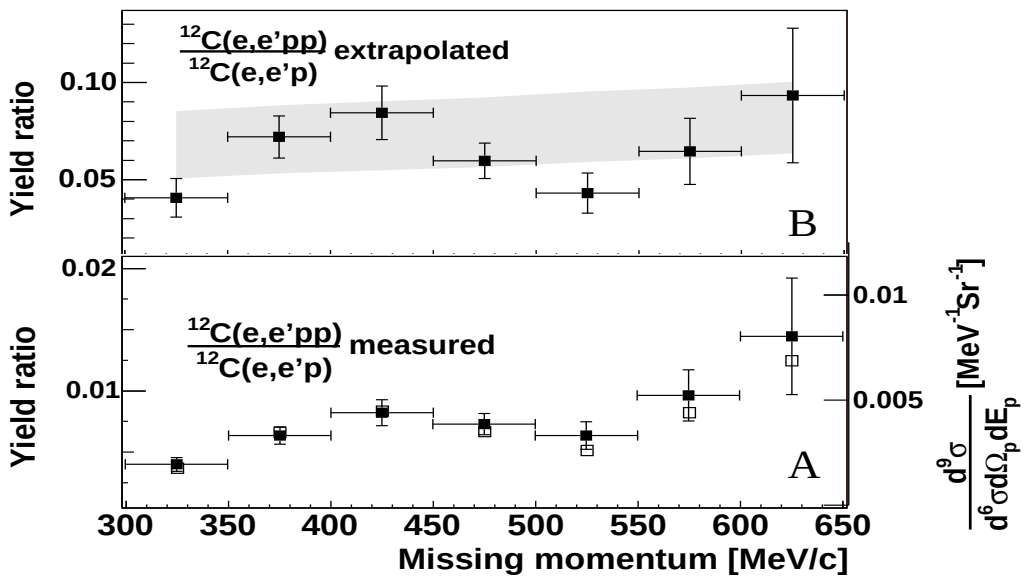

Figure 45: The measured (**A**) and extrapolated (**B**) ratios of yields for the ^{12}C$(e, e'pp)$ and the ^{12}C$(e.e'p)$ reactions. The full squares in **A** denote the yield ratio and the open squares the corresponding ratio of the differential cross section for the ^{12}C$(e, e'pp)$ reaction to that of the ^{12}C$(e, e'p)$ reaction. A Monte Carlo was used for the extrapolation shown in **B** where the finite acceptance of the BigBite spectrometer is taken into account. The gray area in **B** represents a band of $\pm 5\sigma$, uncertainty in the width of the center-of-mass momentum of the pair. This value and associated uncertainty were extracted from the data.

In summary, preliminary results from the experiment are circulating and, with four Ph.D. students working on the analysis, the final results from this experiment should be completed in the upcoming year.

3.10 E02-013

Measurement of the Neutron Electric Form Factor G_E^n at High Q^2

G. Cates, N. Liyanage and B. Wojtsekhowski, spokespersons,
and
the E02-013 and Hall A Collaborations

3.10.1 Introduction

The single discovery at JLab that has caused perhaps the most surprise is that the ratio of the proton's electromagnetic form factors, G_E^p/G_M^p, decreases almost linearly with Q^2 [84]. The implications of this result include the importance of quark orbital angular momentum in determining the QCD dynamics of the nucleon. Indeed, evidence of the importance of quark orbital angular momentum has emerged in numerous other experiments as well. It is also the case that form-factor measurements are providing some of the strongest constraints on models of Generalized Parton Distributions (GPDs) [85]. Furthermore, theoretical explanations for the Q^2 behavior of the ratio of the proton's form factors G_E^p/G_M^p tend to make predictions for the neutron as well. The electric form factor of the neutron G_E^n, however, has only just begun to be measured at values of Q^2 in the range where the surprising behavior of G_E^p/G_M^p was observed. The measurement of G_E^n is thus critical to gaining a better understanding of the implications of the behavior of G_E^p/G_M^p. Also, among the four nucleon form factors, G_E^n is unique in that it vanishes in the static limit. It has a non-zero value at scales of 0.2 to 1 fm which can be understood in terms of a pion cloud. At smaller distance scales, below 0.1 fm, where quark degrees of freedom dominate, G_E^n provides a window into the isospin dimensions of the GPDs and the study of possible other quark configurations, such as di-quarks in the nucleon.

The first suggestion to measure G_E^n with a polarized ^{3}He target was made in 1984 by B. Blankleider and R. Woloshyn [86], and it was soon also discussed by J. Friar *et al.* [87]. There were a number of experiments performed at NIKHEF, Mainz, and Bates, which realized this plan at momentum transfers below 1 GeV^2 [88]. The applicability of a polarized ^{3}He target for G_E^n measurements was carefully studied in non-relativistic 3-body Faddeev type calculations. At momentum transfers in the range of $0.5-1\,\mathrm{GeV}^2$ the model dependence of such measurements becomes large. For sufficiently high momentum transfer final-state interactions become less important and corrections can be calculted within the Glauber approach [89]. However, with standard spectrometers, the statistical uncertainty in G_E^n from such measurements at a Q^2 of few GeV^2 becomes unacceptable. It was clear that a precise measurement of G_E^n would require a certain amount of innovation.

Part of the solution to limited counting rates has emerged over the last several years as experience has accumulated using detector systems with open geometries.

Specifically, the Real Compton Scattering experiment, JLab E99-114, achieved a reliable and acceptably low trigger rate using a largely unshielded lead-glass calorimeter [28]. The success of this experiment led us to investigate a design for an electron spectrometer in which one adds to the segmented calorimeter a finely-segmented high-resolution drift chamber and a magnet with a modest field integral. Using this approach we designed a spectrometer (BigBite) with a solid angle much larger (by 15 times) than the HRS and capable of running at a luminosity typical of the Hall A polarized target.

To take advantage of the large acceptance of BigBite it was also necessary to have a neutron detector with a reasonably matched acceptance. Furthermore, in order to achieve sufficient selectivity in identifying quasi-elastic electron-neutron events, we also needed a neutron detector that would provide a certain amount of kinematic resolution. To address these needs we designed and constructed what we believe is the world's largest neutron detector, which has been nicknamed BigHAND (Big Hall A Neutron Detector). At a weight of roughly 80 tons, BigHAND contains over 200 neutron bars and provides a considerable amount of segmentation. The final selection of the quasi-elastic events was accomplished through the analysis of the transverse component of the missing momentum, for which a resolution could be achieved that was much higher than was the case for the longitudinal component. This technique represents one of the key elements of the experimental concept of E02-013 and was central to enabling us to measure the form factor up to very large momentum transfer. We note that evidence supporting the feasibility of this technique was checked prior to the submission of the E02-013 proposal using ^{3}He$(e, e'p)$ data from a Hall B CLAS experiment [90].

3.10.2 Experiment overview

Experiment E02-013 measured the electric form factor of the neutron by studying spin asymmetries in quasi-elastic scattering in the reaction $^3\vec{\mathrm{He}}(\vec{e}, e'n)$ at four values of Q^2 up to 3.5 GeV^2. The scattered electron and the recoil neutron were detected in coincidence using the above-mentioned open-geometry electron spectrometer BigBite (with a solid-angle acceptance of roughly 76 msr) and the large neutron detector BigHAND which (with an active detection area of around $8\,\mathrm{m}^2$) at a distance 9 to 12 m provided adequate acceptance for quasi-elastic neutrons. Because of the large fringe field of BigBite, and the need to have the target within a distance of roughly one meter, it was necessary to construct a polarized ^{3}He target that provided substantial magnetic shielding. With both spectrometer arms and the target all presenting largely new construction, G_E^n was the largest installation in Hall A since the hall's original commissioning. An engineering drawing of the full experimental setup is shown schematically in Fig. 46.

The BigBite spectrometer was constructed using a large dipole magnet that came from NIKHEF. While the magnet itself was used during an earlier experiment, an entirely new detector package was constructed for the G_E^n experiment.

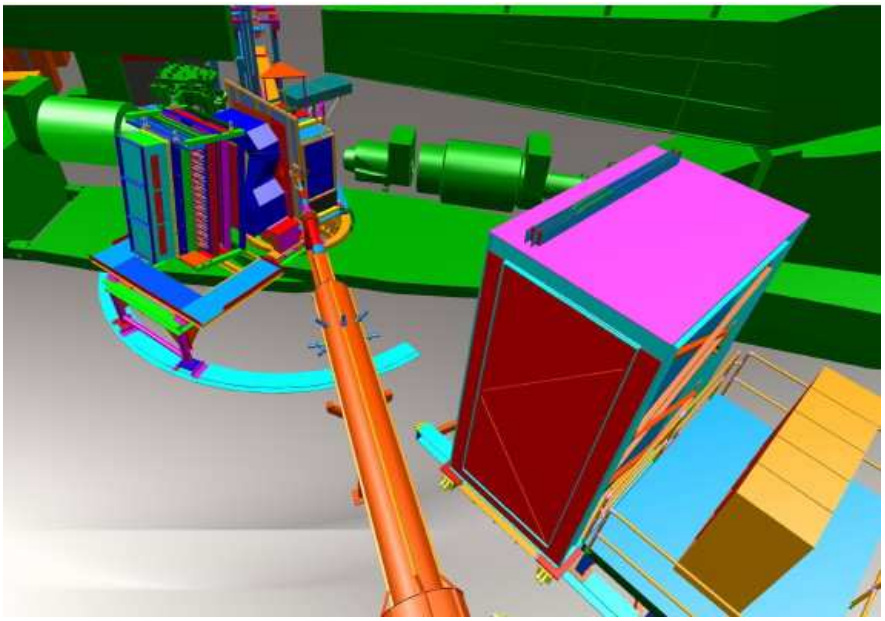

Figure 46: A schematic view of the E02-013 experiment. View from downstream of target. BigBite is on the left, BigHand is on the right.

The detector package includes three wire chambers: a front chamber, a middle chamber, and a back chamber. The front and back chambers each have six planes of sensitive wires, and the middle chamber has three planes of such wires. BigBite also contains a lead-glass shower counter, separated into both a pre-shower and full-absorption region. A hit above high threshold in the shower counter together with a neutron event from BigHAND provided the basic coincidence trigger for the experiment. A top view of BigBite and the downstream part of the target is shown in Fig. 47.

The BigHAND neutron detector contained over 200 neutron bars arranged in seven vertical walls sandwiched between iron, of which the thickness was optimized to provide the best efficiency for detecting high-energy neutrons. It also contained two veto walls with roughly 180 veto counters protected from the target by two inches of lead. Energy discrimination in BigHAND was achieved by measuring time of flight (TOF), and the segmentation was sufficient to facilitate the transverse missing-momentum technique described earlier which was used to identify quasi-elastic events. The BigHAND is shown in Fig. 48 at the moment when the Hall A technical staff is preparing to move it to a next kinematic point, which took about 2-3 hours.

The polarized ^{3}He target that sat on the pivot in Hall A was basically designed from the ground up. A magnetic holding field of roughly 20 G was produced using

Figure 47: Top view on the BigBite spectrometer and the downstream part of the target.

a large iron box that also provided shielding from the fringe field of BigBite and served as a scattering chamber. The sealed glass target cells in which the ^{3}He was polarized contained a hybrid mixture of potassium and rubidium, in contrast with previous target cells in which the only alkali-metal present was rubidium. This permitted the use of "alkali-hybrid spin-exchange optical pumping", a variant of the technique used previously that permitted substantially higher polarization, quicker pump-up times, and less sensitivity to depolarization from the passage of the electron beam. The use of the hybrid technology, however, also meant that the oven that was used to heat the "pumping chamber" of the target cell needed to be able to maintain temperatures substantially higher than previously. The laser optics were also largely new. Light from high-power diode-laser arrays was brought to the target using optical fibers. The optics used for polarizing the light and focusing it onto the target cells were mounted directly on top of the target enclosure, thus avoiding the need for the large "laser hut" that had been used previously for polarized ^{3}He experiments in Hall A. The target held a polarization about 50% during many weeks of continuous running with an 8 μA electron beam as shown in Fig. 49.

An extraordinary effort was required to construct the experimental apparatus for G_E^n, but it was necessary to do so in order to have an experiment capable of producing sufficient statistics in a reasonable length of time. Using a polarized ^{3}He target that was 40 cm in length and roughly 10 atm in pressure, and beam

Figure 48: A view of the BigHAND detector during preparation for moving it to the next kinematic point.

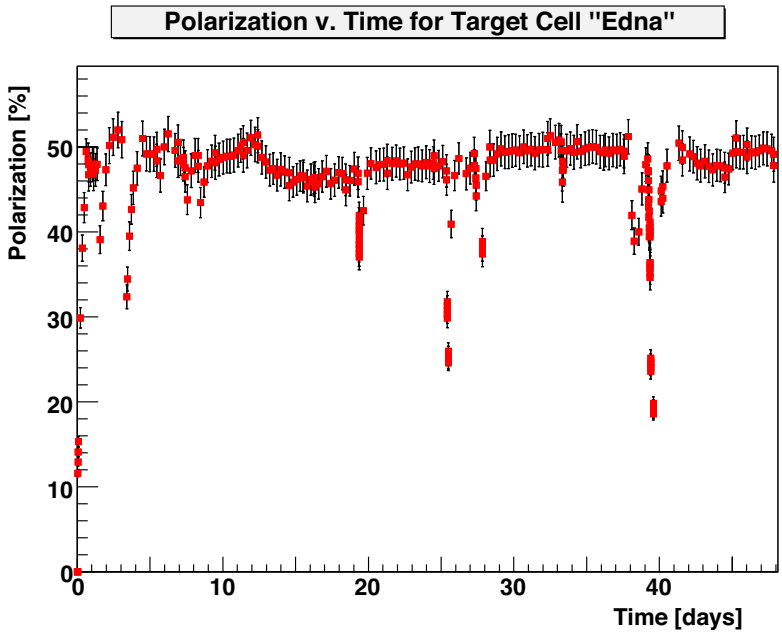

Figure 49: Target polarization in E02-013 experiment.

currents in the range of $7 - 9\,\mu$A, E02-013 operated at a high luminosity of $5 \cdot 10^{36}$ Hz/cm^2. Furthermore, as a result of the use of "alkali-hybrid spin-exchange optical pumping" (or *hybrid* technology for short), polarizations in the range of 50% were obtained in beam, substantially higher than roughly 40% that had been the norm. With high luminosity, improved target polarization, and the very large acceptance of the BigBite/BigHAND combination, we achieved a Figure-of-Merit that was at least 15 times larger than that of any previous G_E^n experiment.

3.10.3 Experimental run

The G_E^n experiment began installation in December of 2005, began commissioning by the end of February 2006, and collected production data over a period of roughly 2 1/2 months. Despite being the first experiment to use the new BigBite detector package, the experiment began taking data after just a few days of commissioning during which a number of reasonably serious problems were solved. Initial difficulties included the alignment of the target cell with respect to the beam, and problems with the VME TDCs in the wire-chamber read out at high rates. The rest of the experiment saw only minor difficulties including leaks through the holes in the beam-line Be window, whose origin was traced to a chemical reaction accelerated in the radiation environment. The steady data taking was aided by a variety of on-line monitoring tools such as an event display

for the BigBite detector package, a scaler display for the 200 neutron bars in BigHAND, and a variety of on-line analysis GUIs. Within a few weeks from the start of data taking, we were confident of the quality of our data, something that was nontrivial given that we were using almost entirely new equipment. The expected accuracy of the results is illustrated in Fig. 50.

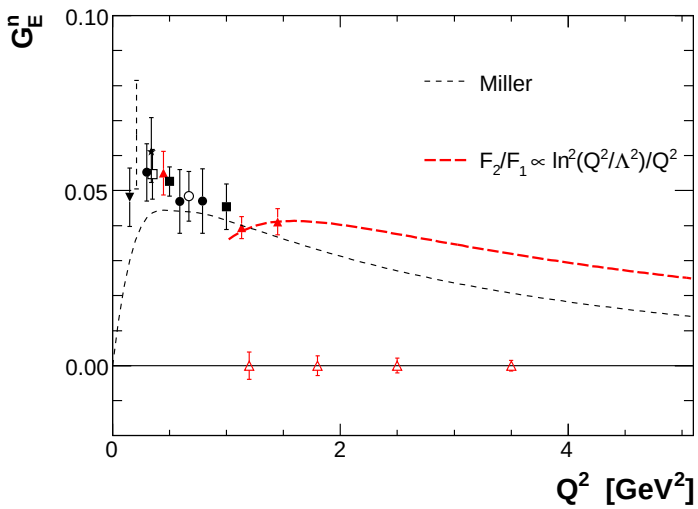

Figure 50: Selected world data on G_E^n with the values of Q^2 in E02-013 and the expected accuracy. The black curve is a calculation in the relativistic constituent quark model by G. Miller [91]. The red curve takes its shape from the pQCD prediction by A. Belitsky *et al.* [92] and has been amplitude normalized to the experimental G_E^n value at 1.3 GeV^2.

3.10.4 Current status of data analysis

The analysis of the G_E^n data is currently underway, and while we have not yet released any numbers on G_E^n itself, we have presented preliminary results from various aspects of the analysis at conferences, including raw asymmetries from one of our kinematic points at 1.8 GeV^2. Major aspects of the G_E^n analysis include tracking in BigBite, calibration in the BigBite calorimeter, timing and position calibration in the neutron arm, target polarimetry, and target polarization direction, and dilution factors.

Since BigBite is essentially an entirely new spectrometer, considerable efforts have gone into the development of track-reconstruction algorithms, verification and improvement of the optics model, and particle identification. During commissioning we performed calibration runs with hydrogen, as well as optics runs using carbon foils. In Fig. 51, for instance, we show a histogram representing the vertex

reconstruction from optics runs using carbon foils that indeed shows the expected width of 5 mm. In Fig. 52, a scatter plot from a hydrogen calibration run displays electron momentum versus scattering angle. The well-defined band represents the elastic peak which we could resolve at the one percent level. The final analysis of the BigBite optics is still in progress. The shower detector, which served very well for trigger purposes, was calibrated before the experiment with cosmic rays. Such a simple calibration was sufficient for data taking and provided an energy resolution of ∼20%, see in Fig. 53 the correlation between the shower amplitude and the electron momentum. The two-layer shower detector also allowed the identification of the electrons by analyzing the amplitude in the first layer, see the distribution in Fig. 54, that demonstrates a very efficient rejection of pions.

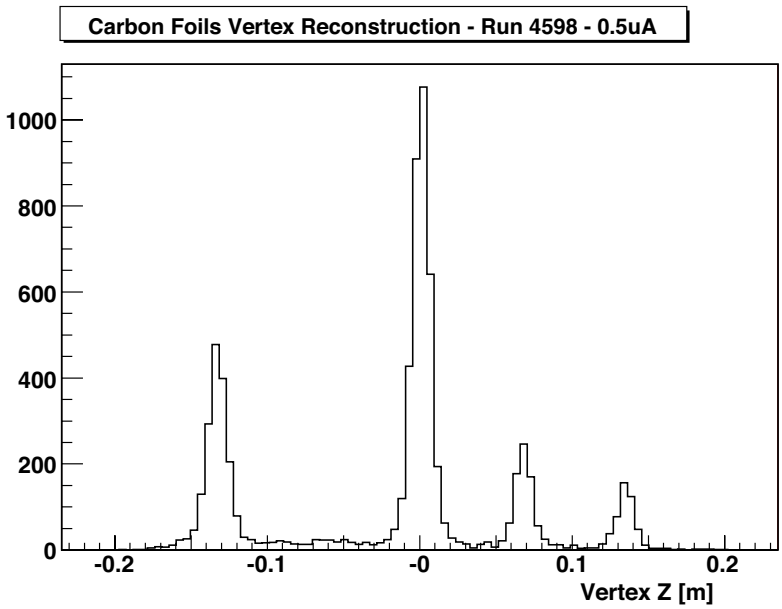

Figure 51: The target-coordinate reconstruction for the optics target.

The analysis of the neutron-arm data is a big challenge already due to the large number of different counters and the huge amount of data per event. The most important characteristics are time-of-flight resolution, veto efficiency, and neutron detection efficiency. Preliminary results for each of these parameters are very encouraging. The time resolution, which at the trigger level is ∼20 ns with a real to accidental coincidence of 2:1 (Fig. 55), improves to ∼0.5 ns after corrections, as shown in Fig. 56. The veto efficiency per counter is about 95%, which is consistent with expectations at the high counting rate.

The very preliminary combined analysis of data from the electron and the neutron detectors is presented in Fig. 57 and Fig. 58 for the momentum transfer $Q^2 = 1.8$ GeV^2. The left panel of Fig. 57 shows electron-proton events for the

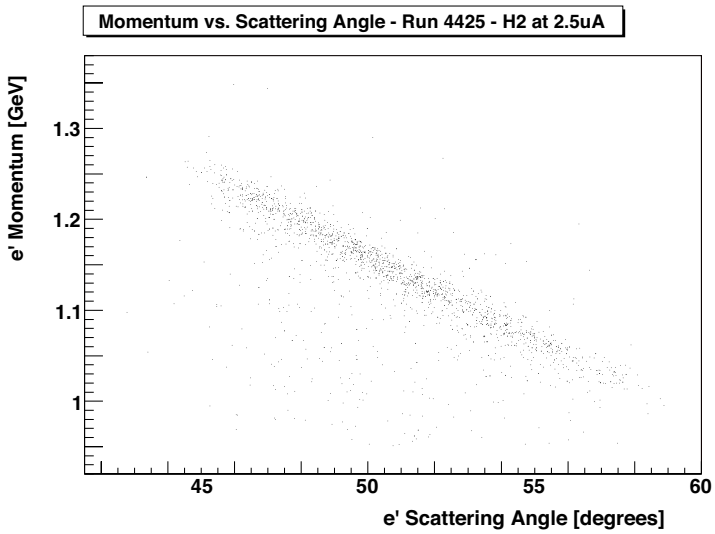

Figure 52: The electron momentum vs. scattering angle in BigBite.

reconstructed mass W and the missing momentum projected on the momentum transfer direction P_{par}. The right panel of the same figure shows a similar distribution for the electron-neutron events. Although the background is much larger, the quasi-elastic peak is well visible. The final selection of the quasi-elastic events is done by analysis of the component of the missing momentum orthogonal to the momentum transfer direction P_{per}, as it is shown in Fig. 58 for the electron-neutron events. The left panel shows the event distribution in variables W and P_{per}. The right panel shows three histograms, made for the ranges of W indicated on the left panel. The histograms colored by green display the levels of accidentals. It is easy to see that for the W of the quasi-elastic peak the P_{per} distribution has the expected maximum near 70 MeV/c and the ratio of the signal to the accidentals is sufficiently large for further analysis.

We would like to thank the E02-013 analysis team, especially R. Feuerbach and S. Riordan, for the plots included in this contribution.

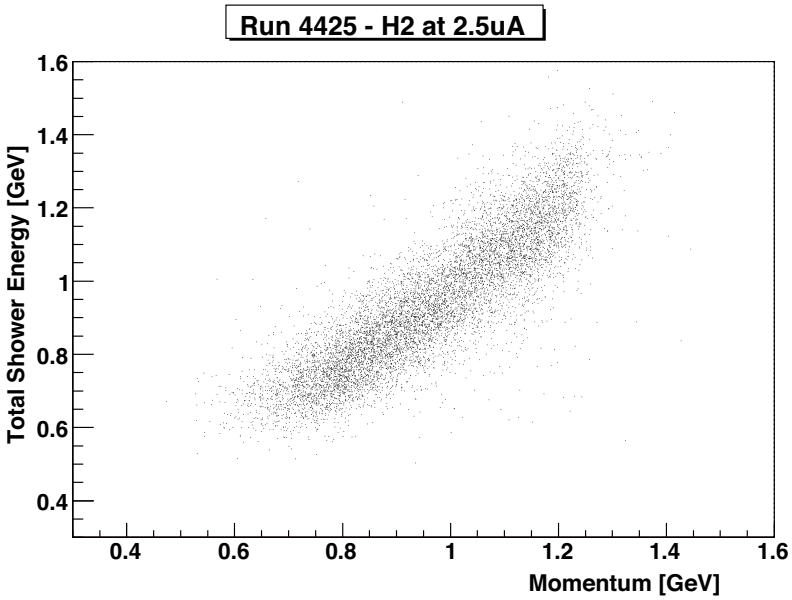

Figure 53: The energy in the shower detector vs. electron momentum.

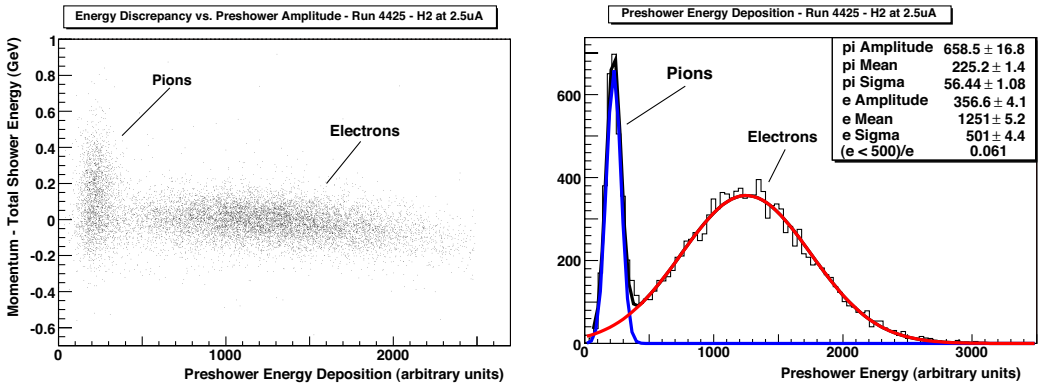

Figure 54: The energy deposition in the pre-shower layer showing a clear separation between the pion peak and the electron peak.

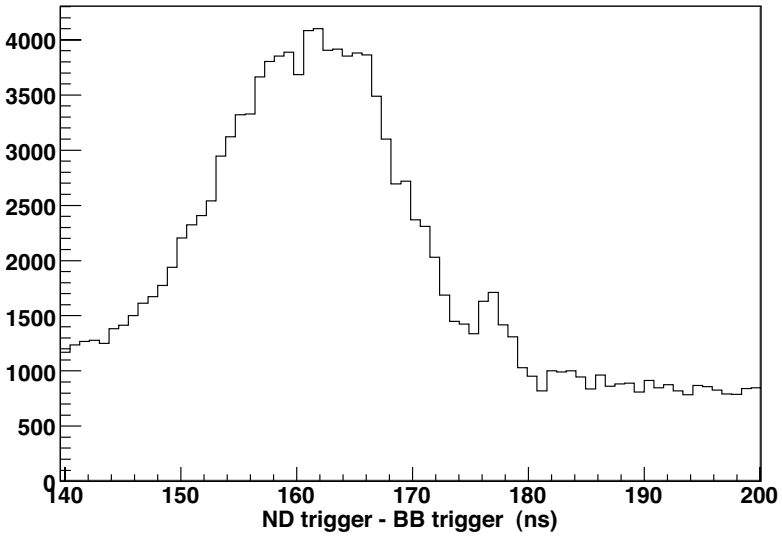

Figure 55: The raw time spectra between trigger signals of two arms.

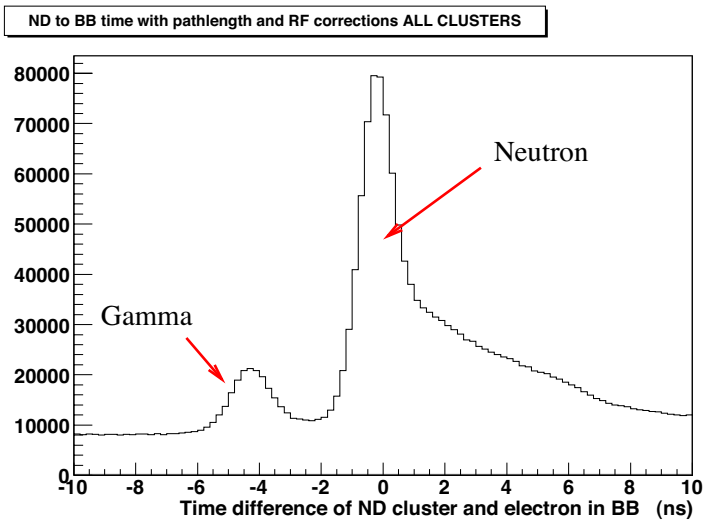

Figure 56: The time-of-flight spectra for electron-neutron events. The peak located 4 ns left of the neutron peak is due to prompt photons.

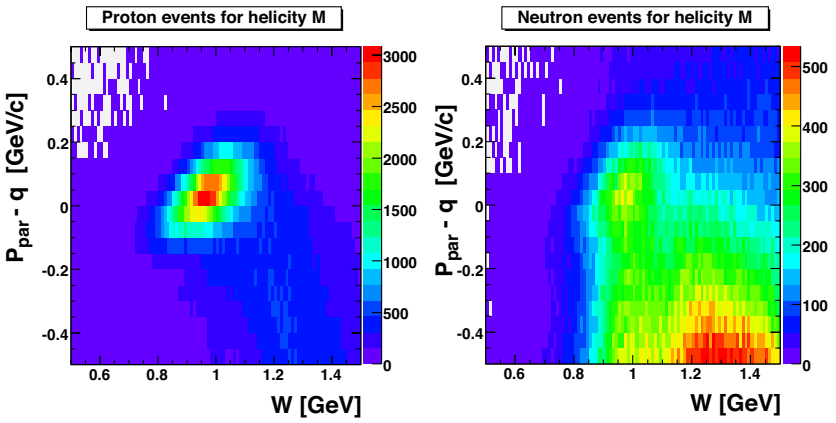

Figure 57: Left: distribution of the electron-proton events for W vs. the missing momentum parallel to the momentum transfer; right: the same distribution for the electron-neutron events.

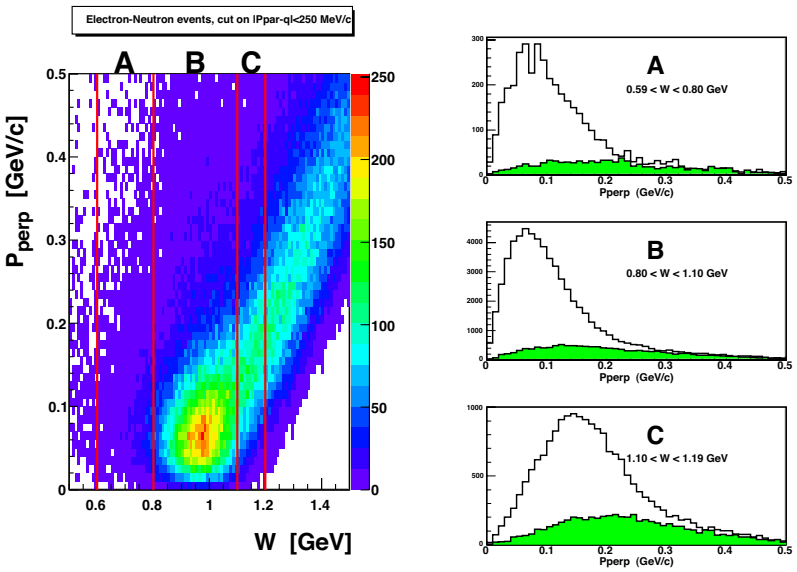

Figure 58: Left: distribution of the electron-neutron events for W vs. the missing momentum perpendicular to the momentum transfer; right: the P_{per} distributions for the selected intervals of W with the level of accidental events indicated by green.

3.11 E03-104

Probing the Limits of the Standard Model of Nuclear Physics with the ^{4}He$(\vec{e}, e'\vec{p})^3$H Reaction

R. Ent, R. Ransome, S. Strauch and P. Ulmer, spokespersons,
and
the Hall A Collaboration

Experiment E03-104 ran in Hall A from October 3 to November 9, 2006 and analysis is now underway. Michael Paolone from the University of South Carolina is the Ph.D. student analyzing the data.

The goal of the experiment was to measure the induced and transferred polarization in the ^{4}He$(\vec{e}, e\vec{p})^3$H reaction in quasielastic kinematics and for low missing momenta at Q^2 values of 0.8 and 1.3 GeV^2. The observables include the polarization-transfer coefficients perpendicular and parallel to the three-momentum-transfer direction, P'_X and P'_z, as well as the induced polarization, P_y, normal to the electron-scattering plane. The ratio P'_x/P'_z is expected to be sensitive to the ratio of the proton electromagnetic form factors, G_E/G_M, in the dense nuclear medium; P_y is due to final-state interactions. Measuring both the polarization-transfer ratio for ^{4}He and ^{1}H, allows us to determine the double ratio $R = (P'_x/P'_z)_{^4\mathrm{He}}/(P'_x/P'_z)_{^1\mathrm{H}}$ and compare the reaction on the bound proton directly with that on the free proton.

Experiment E03-104 is an extension of E93-049 [93]. The latter experiment found reasonable agreement between data and calculation only after inclusion of medium-modified nucleon form factors, as predicted by the quark-meson coupling (QMC) model [94]. Although conventional DWIA calculations could, in principle, be improved at the cost of added complexity, the inclusion of medium-modified nucleons may offer a more economical description of the structure of the nucleon in the nuclear medium. However, the uncertainties of existing data do not allow a definite conclusion; see Fig. 59. The theoretical community has a substantial and growing interest in obtaining more precise data for this reaction. New microscopic calculations by R. Schiavilla *et al.* [95] challenge the interpretation of the experimental data in terms of medium-modified form factors. However, the calculations include a parameterization of final-state interactions which are not well constrained. The expected high-precision data on the induced polarization will be a crucial test of this part of the reaction mechanism. In addition, new calculations based on the Glauber approximation, by Ryckebusch *et al.* [96], and a chiral quark-soliton model (CQSM) calculation of the in-medium form factors by Smith and Miller [97], provide alternative explanations.

The experiment was installed directly after the LEDEX experiment and used essentially the same set-up. The only new pieces of equipment were 10 cm long high-pressure ^{4}He and the liquid ^{1}H target cells. The experimental run was a success. E03-104 collected several hundred million events, as listed in Table 5.

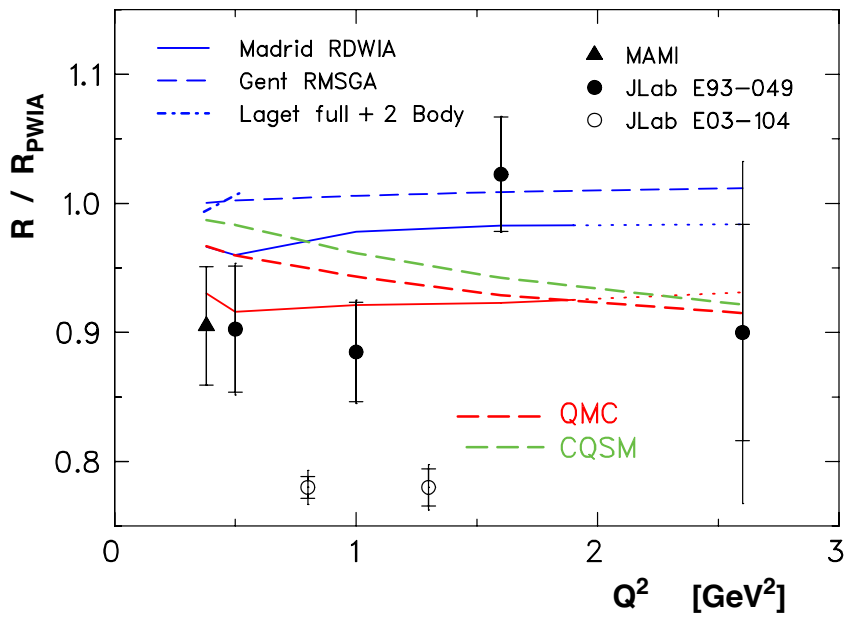

Figure 59: Existing data from Mainz and JLab along with anticipated uncertainties from experiment E03-104. R is the ratio of transverse to longitudinal polarization of the recoiling protons in ^{4}He compared to the same ratio for ^{1}H. The data are compared to calculations by the Madrid and Ghent groups, with and without including in-medium modifications as predicted by quark-meson coupling (QMC) and chiral quark-soliton (CQSM) models; and at $Q^2 < 0.5$ GeV^2 only, to Laget's full calculation, including two-body currents. Lines connect the acceptance-averaged theory calculations. See Ref. [93] for further details.

The preliminary analysis of this experiment indicates the measured polarization-

Table 5: Number of collected events on the hydrogen and helium targets

	$Q^2 = 0.8$ GeV^2	$Q^2 = 1.3$ GeV^2
Data on ^{1}H	300 M	500 M
Data on ^{4}He	190 M	200 M

transfer double ratio will have an uncertainty roughly a factor of two to three smaller than for E93-049. Limitations of the CHL required running at 80 μA instead of the originally planned current of 100 μA on the helium target, and the average efficiency of the focal-plane polarimeter was slightly lower than expected. However, a higher than expected beam polarization, about 86%, and both higher beam currents and a higher data-acquisition rates while running on the hydrogen target, largely compensated for the lower beam current on helium. Preliminary results of the hydrogen runs are shown in Fig. 60.

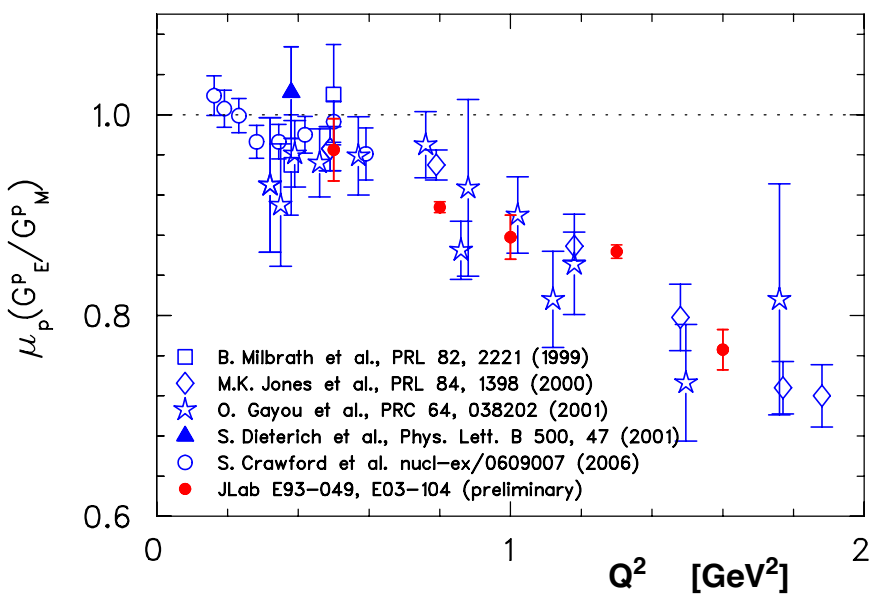

Figure 60: The ratio $\mu_P G_{E_p}/G_{M_p}$ from previous recoil-polarimeter experiments [84,98–101] including E93-049 and E03-104 data. The results for E03-104 are very preliminary and are merely shown to illustrate the small statistical uncertainties obtained in this experiment.

In addition, E03-104 included calibration runs to better determine the recoil polarimeter false asymmetries. In the one-photon exchange approximation the induced polarization in ^{1}H$(e, e'\vec{p})$ vanishes. To the extent that P_y is indeed small ($< 1\%$) these data are a direct measure of false asymmetries. Improving on the plan envisioned in the proposal we took all elastic ep data (combining calibration and production data) in nine sets of proton-spectrometer momenta with a relative variation of $\delta = -8\%$ to $\delta = +8\%$ compared to the central setting. This extensive data set will allow us to study false asymmetries and the spin transport in great detail.

During a short period of time at the $Q^2 = 0.8$ GeV^2 setting, while Hall C's activities prohibited running with polarized beam, and at the end of the experiment at the $Q^2 = 1.3$ GeV^2 setting, we took some data on a ^{12}C target. These data may allow us to extract the induced polarization for the $p_{3/2}$-shell knockout in the ^{12}C$(e, e'\vec{p})$ reaction.

3.12 E03-106

Deeply Virtual Compton Scattering off the Neutron

P.-Y. Bertin, C.E. Hyde-Wright, F. Sabatié and E. Voutier, spokespersons,
and
the Hall A Collaboration

Compton scattering in the deeply virtual regime is expected to reveal unique features of the partonic structure of the nucleon in terms of Generalized Parton Distributions (GPDs). Following the E00-110 experiment where the scaling of the DVCS cross section off the proton was observed, the E03-106 experiment intends to explore DVCS off the neutron, by measuring the difference between the polarized cross section for electrons of opposite longitudinal polarizations. Because of the very small magnitude of the Dirac form factor in the neutron case, this observable is supposed to be very sensitive to E, the least known and constrained GPD.

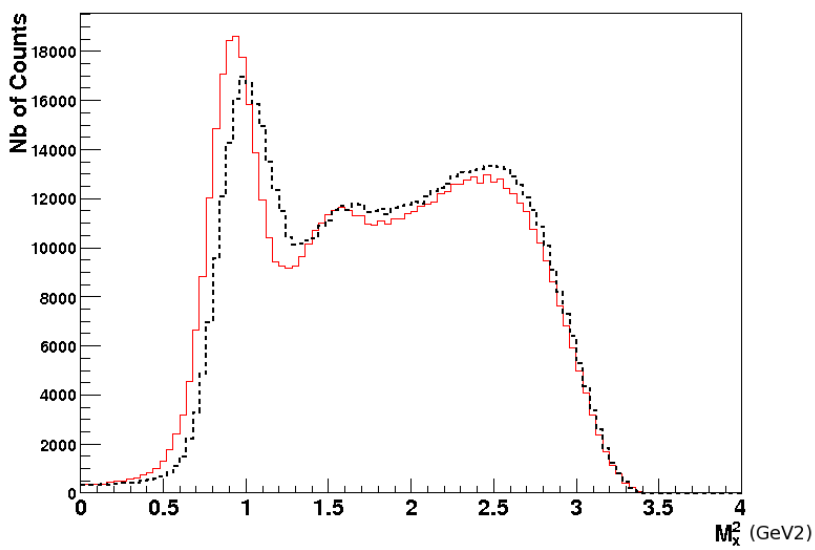

Figure 61: Global squared missing-mass spectra of the n$(e, e'\pi^-)$ reaction on a LD_2 target before (black) and after (red) the π^- calibration.

The experimental method to extract the DVCS cross section on the neutron relies on the deconvolution of the different sources of γ production

$$\mathrm{D}(e, e'\gamma)X = p(e, e'\gamma)p + n(e, e'\gamma)n + d(e, e'\gamma)d + \cdots \quad . \tag{15}$$

Subtracting the proton contribution measured on a hydrogen target, the separation of the neutron and deuteron contributions is performed via a global fitting

procedure taking advantage of the dynamical separation $(-t/2)$ between these two channels, and of the different kinematical factors that dominate their $\sin(\phi)$ moments.

The combination of the experimental resolution and the small amplitude of the neutron signal makes the subtraction method sensitive to the relative position of the missing-mass peaks. In E03-106, a shift of the missing mass was observed on the LD_2 target which was corrected via new calibration procedures using the $D(e, e'\pi^-)pp$ and the $D(e, e'\pi^0)X$ reactions to adjust the calibration coefficients obtained from elastic electron scattering on hydrogen. This shift originates in the effects of the electromagnetic background on the calorimeter when running with a higher luminosity on the LD_2 than on the LH_2 target. The result of the π^- calibration is shown on Fig. 61. The π^- and π^0 calibrations still differ by 1 %, which contributes to the systematic uncertainty of the $D(e, e'\gamma)$-$H(e, e'\gamma)$ subtraction.

A large part of the physics background contaminating the DVCS signal originates in the asymmetric decay of a π^0 where the produced high energy γ mimics the DVCS γ, and the low-energy partner is not detected because of acceptance or trigger threshold effects. This background is deduced from the simultaneously measured experimental yield of symmetric π^0 decays, which are identified by the detection of 2γ in the calorimeter. In E03-106, the measured ratio of π^0 production on deuterium, relative to hydrogen is $0.95 \pm 0.06 \pm$syst. Thus both the deuteron coherent and neutron quasi-free π^0 production are consistent with less than 5 % of the exclusive production on the proton.

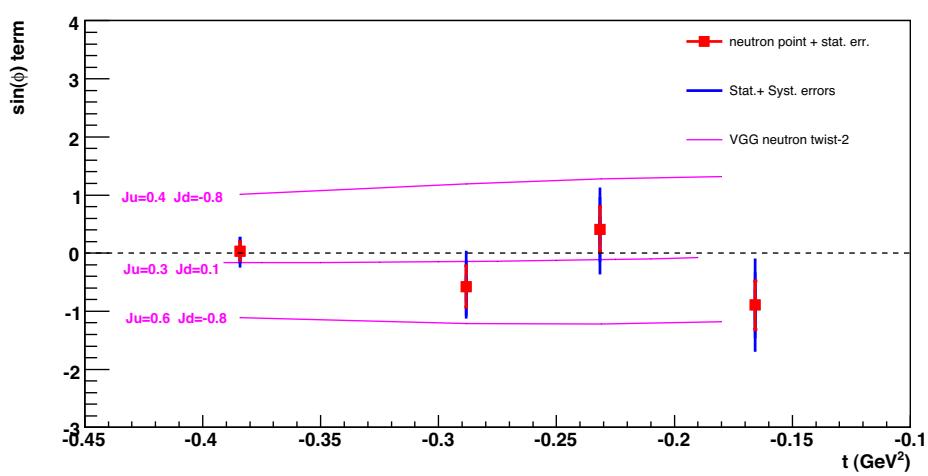

Figure 62: t dependence of the neutron moments compared to different VGG expectations.

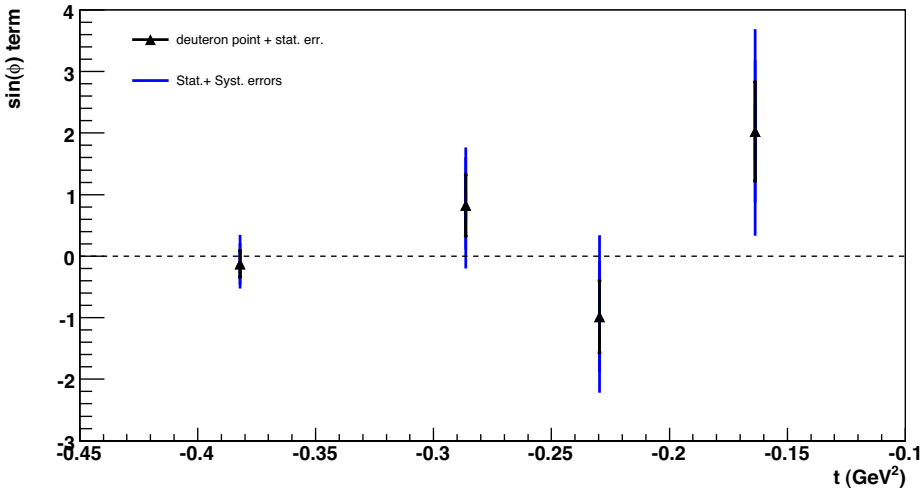

Figure 63: t dependence of the deuteron moments.

The measured polarized cross-section difference has been analyzed at leading twist, by extracting the $\sin(\phi)$ moment and taking into account the ϕ-dependent BH propagators. The resulting neutron moments turn out to be small and negative (Fig. 62), consistent with theoretical expectations; the sensivity to the GPD E through the quark angular momentum is also shown on the figure. The deuteron moment tends to exhibit a positive sign (Fig. 63), in accordance with theoretical expectations. The error bars in the figures include the systematic errors, originating from the uncertainties in the calorimeter calibration.

3.13 E04-012

High-Resolution Search for $\Theta^+(1540)$ Partners

P.E. Reimer and B. Wojtsekhowski, spokespersons,
and
the Hall A Collaboration

3.13.1 Introduction

The discovery of exotic baryonic states with positive strangeness, requiring a minimal configuration of four quarks and an antiquark would contribute greatly to the understanding of confinement in Quantum Chromodynamics (QCD). Although searches for such states have been conducted for almost 40 years with both partial wave analyses of hadroproduction (*e.g.* [102]) and electroproduction (*e.g.* [103]), these early results have generally been interpreted as unconvincing [104]. Recent claims of the observation of one such state, the $\Theta^+(1540)$ [105] have generated renewed experimental and theoretical interest in this topic. For recent reviews of the experimental evidence, see Refs. [106–108]. If confirmed, the Θ^+ could be the lowest-mass member of an antidecuplet of pentaquark states, predicted within the framework of the Chiral Quark Soliton Model [109]. Alternatively, such exotic baryons have been explained in terms of models based on diquark configurations [110], or in terms of isospin-violating strong decays, which lead to an isotensor multiplet of Θ-pentaquarks of different charge states [111]. If the Θ^+ pentaquark exists, then other members of its symmetry group and/or other multiplets containing exotic states [112,113] should be observable as well, provided they are sufficiently narrow. All of the approaches mentioned predict partner states in the mass region $M \approx 1500 - 2000$ MeV.

Here we report on a first high-resolution search at forward production angles for the Σ_5^0 and N_5^0 non-exotic members of the antidecuplet and for the exotic Θ^{++} as narrow resonances in the missing-mass spectra of the reactions $ep \to eK^+X$, $ep \to e\pi^+X$ and $ep \to eK^-X$, respectively. The measurements covered a limited range of small scattering angles, which did not allow a partial-wave analysis; however, both experimental indications [105] and theoretical expectations [114] are for the Θ^+ cross section to be forward peaked. At large scattering angle, a recently reported search found no statistically significant evidence for the Θ^{++} [115]. In the present experiment, very good mass resolution was achieved. Precise measurements of the known $\Lambda(1116)$, $\Sigma(1193)$ and $\Lambda(1520)$ states were obtained for calibration.

3.13.2 Experiment

The experiment took place in Hall A using a 5 GeV electron beam incident on a 15 cm long liquid hydrogen target. Scattered electrons were detected in one of the

High-Resolution Spectrometers (HRS) [20] in coincidence with electroproduced hadrons in the second HRS. Each spectrometer was positioned at 6° relative to the electron beam by using a septum magnet [116] to achieve this small scattering angle. The spectrometers had an effective acceptance of approximately 4 msr in solid angle and ±4.5% in momentum. To obtain the desired missing-mass coverage, the central momentum of the electron HRS was varied between 1.85 and 2.00 GeV/c, while the central momentum of the hadron HRS was changed between 1.89 and 2.10 GeV/c. In these configurations, the average momentum transfer of the virtual photon was $\langle Q^2 \rangle \approx 0.1$ GeV^2, and the average center-of-mass (CM) photon energy was $\langle E_\gamma^{CM} \rangle = 1.1$ GeV. For the kaon (pion) kinematics, the center-of-mass scattering angle was $5.6° \leq \theta_{\gamma^* K}^{CM} \leq 11.4°$ ($5.0° \leq \theta_{\gamma^* \pi}^{CM} \leq 10.4°$), and the angular acceptance was $\Delta\Omega_{\gamma^* K}^{CM} \approx 38$ msr ($\Delta\Omega_{\gamma^* \pi}^{CM} \approx 32$ msr).

Both spectrometers have a QQDQ magnet arrangement with a 45° upward bend. The detector packages, placed behind the magnetic elements, were equipped with four planes of drift chambers for tracking and two planes of hodoscopes for triggering. The electron spectrometer employed a CO_2 gas Čerenkov counter and lead-glass shower counters for pion rejection. For the kaon measurements, a clean particle identification (PID) in the hadron spectrometer was particularly important because of the very high ratio of π/K rates. With the use of two aerogel ($n = 1.015$ and 1.055) and a ring-imaging Cerenkov detector (RICH) [117] in the hadron spectrometer a pion contamination in kaon events of less than 5% was achieved. A negligible pion contamination remained after an additional separation using the coincidence timing between the hadron and electron signals. The aerogel counters and coincidence timing were also effective in removing any proton background.

The measured yields were corrected for detection and reconstruction efficiencies and dead time. Cuts on the events from the PID detectors were applied to select appropriate particle types, and vertex and coincidence time cuts were used to reduce background from accidentals. The missing mass was reconstructed using the measured momenta of the electron and kaon (pion).

Calibration data were taken in the $ep \to e'\pi^+X$ channel in the missing-mass range which included the neutron and in the $ep \to e'K^+X$ channel covering the missing-mass range including the $\Lambda(1116)$ and $\Sigma(1193)$. The missing-mass resolution was $\sigma_{instr.} = 1.5$ MeV, determined by fitting the missing-mass peaks for the neutron, $\Lambda(1116)$ and $\Sigma(1193)$. Based on the fit masses of these well-known calibration states, the accuracy of the reconstructed missing mass was determined to be better than 3 MeV. The photoproduction cross section of the $\Lambda(1520)$ was determined by fitting the $H(\gamma^*, K^+)X$ missing mass spectra to a Breit-Wigner with an energy-dependent width [118] and a non-interfering background. From this fit, the cross section was determined to be $d\sigma/d\Omega\,[\gamma^* p \to K^+\Lambda(1520)] = 417 \pm 30\ (stat.) \pm 41\ (syst.)$ nb/sr with a width of $\Gamma_{\Lambda(1520)} = 16.5 \pm 1.7\ (stat.)$ MeV at $\langle Q^2 \rangle = 0.1$ GeV^2. The largest systematic uncertainty arises from the absolute

acceptance of each of the spectrometer arms for an extended target. From the fit, the $\Lambda(1520)$ mass was determined to be 1519.9 ± 0.6 $(stat.) \pm 3$ $(syst.)$ MeV. Both the mass and width are in good agreement with the PDG averages [119].

For each of the three possible pentaquark states, missing-mass spectra from several (up to eight) different kinematic settings of the spectrometers were combined. The individual settings typically covered a range of approximately 130 MeV in missing mass. Each individual missing-mass spectrum was transformed into a photoproduction cross-section spectrum in the CM and the accidental coincidence background was subtracted. Combining the spectra required careful relative integrated luminosity normalizations and special attention to the acceptance weighting as a function of missing mass. The individual data sets overlapped to some extent, allowing for verification of the weighting and normalization. After finalizing the detector analysis, all transitions between spectrometer settings were found to be smooth, requiring no *ad-hoc* scaling. These spectra are shown in Fig. 64.

3.13.3 Analysis

Within each of the search regions, $1550 < M_x < 1810$ MeV for the Σ_5^0, $1610 < M_x < 1880$ MeV for the N_5^0 and $1480 < M_x < 1590$ MeV for the Θ^{++}, the data were examined for the existence of narrow resonances. A scan was performed in 1 MeV steps over each search region. For each mass, M_x, and width, Γ_x, the goal was to determine a range in the cross section of a hypothetical resonance that would be compatible with the missing-mass spectrum at 90% confidence, with no *a priori* assumption of a non-zero resonance cross section. To accomplish this, the Feldman and Cousins [120] approach was adopted. The procedure outlined below was repeated for widths of 0.5, 2, 5 and 10 MeV.

For a given missing mass, M_x, the first step was to determine the level of background by fitting the 20 MeV wide sidebands above and below the region containing 90% of a hypothesized peak at M_x with width Γ_x. When M_x was near the edge of the acceptance, the side band near the edge was reduced, to a minimum of 5 MeV. With the background level fixed, the data were fit to a Breit-Wigner with and energy-dependent width peak at M_x and width Γ_x convoluted with a 1.5 MeV wide Gaussian (instrumental resolution) plus the fixed background within the same window. The only free parameter in this fit was the cross section of the BW resonance, determining σ_{best}, the most likely cross section, of the possible resonance. Because of the paucity of events in some bins for some spectrometer settings, all fits used maximum likelihood techniques [120,121]. The range in cross section, σ, accepted at 90% confidence was determined by examining deviations in the log likelihood, $\ln \mathcal{L}$, as a function of σ from its best value, $\Delta \ln \mathcal{L}_{data}(\sigma, \sigma_{data}^{best})$. The limit in $\Delta \ln \mathcal{L}$ of the 90% confidence region was determined by Monte Carlo. For a given *assumed* cross section, σ_x, many Monte Carlo "experiments" were performed. Missing-mass spectra for each spectrometer setting were randomly populated with total statistics equal to that of the actual data. The spectral

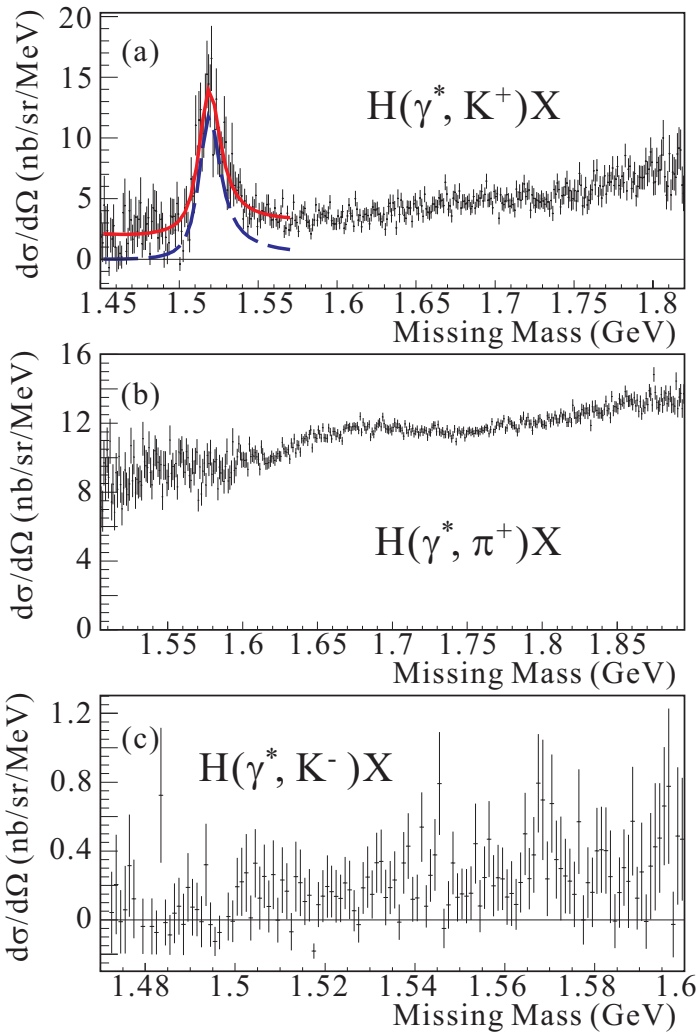

Figure 64: The acceptance-weighted, combined missing mass spectra obtained for the three reaction channels, after accidental coincidence background subtraction: (a) $\gamma^* p \rightarrow K^+ X$ (Σ_5^0 search). The solid red curve shows the fit to the $\Lambda(1520)$ and non-resonant background and the blue dashed curve shows only the $\Lambda(1520)$ contribution, (b) $\gamma^* p \rightarrow \pi^+ X$ (N_5^0 search), and (c) $\gamma^* p \rightarrow K^- X$ (Θ^{++} search). Other than the $\Lambda(1520)$ peak in the K^+ channel (a) no statistically significant, narrow peaks were found in the data.

Table 6: This table lists the largest upper limit on the photoproduction cross section of the Σ_5^0, N_5^0 and Θ^{++} in nb/sr and relative to the measured $\Lambda(1520)$ cross section of 417 ± 30 (*stat.*) ± 41 *syst.* nb/sr for resonance widths of $\Gamma = 0.5$, 2, 5, 10 MeV.

Γ	Σ_5^0		N_5^0		Θ^{++}	
[MeV]	[nb/sr]	%	[nb/sr]	%	[nb/sr]	%
0.5	10.0	2.3	4.5	1.1	3.0	0.7
2.0	11.0	2.6	5.5	1.3	3.5	0.8
5.0	13.0	3.1	6.0	1.4	3.5	0.8
10.0	17.5	4.2	10.5	2.5	4.0	1.0

shape was based on the smoothed background shape determined in the data analysis with a hypothetical resonance of cross section σ_x added. From each Monte Carlo "experiment", $\Delta \ln \mathcal{L}_{MC}\left(\sigma_x, \sigma_{MC}^{best}\right)$, the difference between the hypothetical resonance's cross section and the best fit of the Monte Carlo spectra was determined. The distribution of $\Delta \ln \mathcal{L}_{MC}$'s from the Monte Carlo "experiments" was examined to determine $\Delta \ln \mathcal{L}_{90\%}$ such that 90% of the Monte Carlo simulations had $\Delta \ln \mathcal{L}_{MC}(\sigma_x, \sigma_{MC}^{best}) > \Delta \ln \mathcal{L}_{90\%}$[2]. If $\Delta \ln \mathcal{L}_{data}(\sigma_x, \sigma_{data}^{best}) > \Delta \ln \mathcal{L}_{90\%}$ then σ_x was within the accepted 90% confidence region. In addition, curves indicating the 90% probability of background fluctuations were generated using a similar technique as suggested by Feldman and Cousins [120]. The upper limit, lower limit and statistical sensitivity curves are shown in Figs. 65, 66 and 67 for the $\Gamma_x = 0.5$ and 10 MeV cases. The maximum upper limits listed in Table 6 are expressed for each resonance in nb/sr and as a fraction of the $\Lambda(1520)$ cross section.

As can be seen in Figs. 65, 66 and 67 most of the 90% confidence region shows only upper limits and the upper limit curves oscillate about the statistical sensitivity curves. Where the lower limit curves are different from zero, they are always below the sensitivity curves implying that none of the lower limits can be distinguished from a statistical fluctuation.

There are several known or suspected resonances in this mass region, in particular several 3 or 4-star Λ and Σ states in the $\gamma^* p \to K^+ X$ channel [119]. Most are too wide (> 50 MeV) to be visible in this experiment (unless they have a *substantial* cross section) and have only been seen in partial-wave analyses or both. Taken together, they add up to a relatively smooth background.

In conclusion, a high-resolution search for the Σ_5^0, N_5^0 and Θ^{++} has been completed using the Hall A HRS spectrometers. This search had an instrumental resolution of $\sigma_{instr.} = 1.5$ MeV. No statistically significant narrow ($\Gamma < 10$ MeV) structures were observed in any of the three reaction channels. Upper limits of the photoproduction cross section for these states were found to be $< 5\%$ of the

[2]Recall $\ln \mathcal{L} < 0$ (in the large statistic limit, $\chi^2 = -2 \ln \mathcal{L}$).

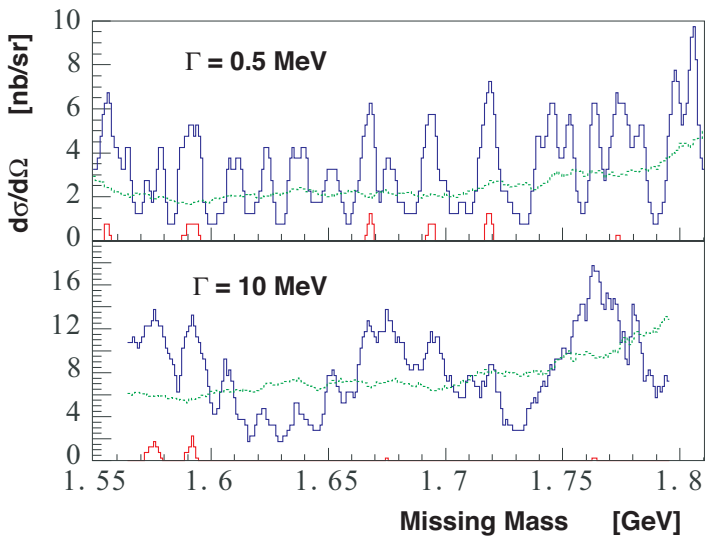

Figure 65: The upper and lower limit top (blue) and bottom (red) solid lines at 90% confidence level for the production of the Σ_5^0 in the reaction $\gamma^* p \to K^+ \Sigma_5^0$ is shown as function of mass for two possible widths of the Σ_5^0. In most cases, the lower limit (bottom–red curve) is zero. The smoother green dashed curve shows the statistical sensitivity.

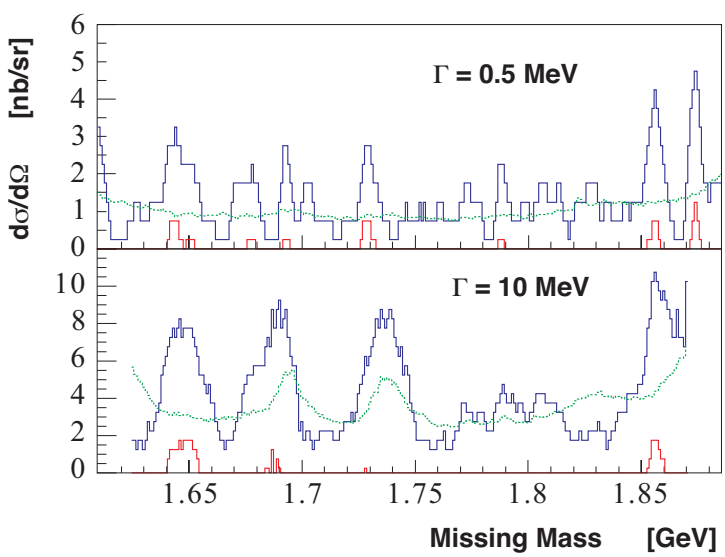

Figure 66: The 90% confidence level limits for the production of the N_5^0 in the reaction $\gamma^* p \to \pi^+ N_5^0$ is shown. The curves have the same meaning as in Fig. 65.

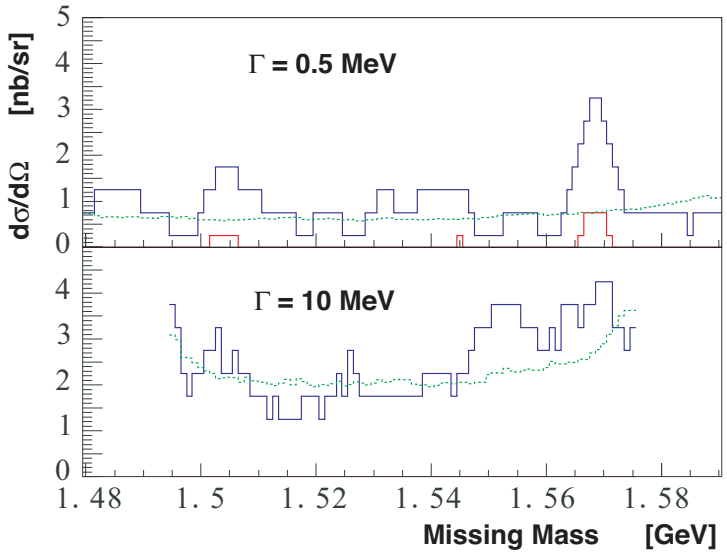

Figure 67: The 90% confidence level for the production of the Θ^{++} in the reaction $\gamma^* p \to K^- \Theta^{++}$ is shown. The curves have the same meaning as in Fig. 65.

$\Lambda(1520)$ photoproduction cross section for $\Gamma \leq 10$ MeV at 90% C.L.

We are grateful to W.J. Briscoe, W. Dunwoodie, M. Polyakov and M. Vanderhaeghen for useful discussions in planning these measurements.

3.14 E05-004 and E05-103

LEDEX Experiments

R. Gilman, D. Higinbotham, X. Jiang, A. Sarty and S. Strauch, spokespersons,
and
the Hall A Collaboration

Two Low-Energy Deuteron EXperiments (LEDEX) ran in Hall A during July – September, 2006: E05-004, $A(Q)$ at Low Q in *ed* Elastic Scattering, and E05-103, Low Energy Deuteron Photodisintegration. The experiments have three Ph.D. students analyzing the data, J. Glister from St. Mary's and Dalhousie Universities, Canada, G. Ron from Tel Aviv University, Israel, and B.W. Lee from Seoul National University, Korea.

The goal of E05-004 was to resolve a discrepancy of about 10% between two high-precision data sets, from Mainz [122] and Saclay [123], in the region $Q = \sqrt{Q^2} = 0.2 - 0.4$ GeV. The best conventional non-relativistic calculations tend to lie between the two data sets, with relativistic calculations tending to increase the prediction slightly towards the Mainz data. The best chiral perturbation theory calculations agree well with the Saclay data. It has been found that extractions of the deuteron form factors from the recent Bates tensor polarization [124] data vary by a few σ depending on whether $A(Q)$ is assumed to follow the Saclay or the Mainz data. Thus, it is important to resolve the discrepancy to determine the sign of the leading relativistic corrections at low Q, the level of convergence of chiral perturbation theory calculations, and the deuteron form factors with improved confidence.

The experimental technique was based on scattering electrons from tantalum, aluminum, carbon, hydrogen, and deuterium targets. Tantalum is used primarily for kinematic fits to determine the beam energy, while aluminum is used to subtract the background in the hydrogen and deuterium data. The carbon data provide a check of our ability to measure the cross section from a solid target; carbon cross sections were previously measured at NIKHEF to $\approx$1%. Hydrogen provides a similar check of our ability to measure the cross section, with the advantage of having the same extended target geometry as the deuterium, along with a greater sensitivity to target heating. One spectrometer was used as a luminosity monitor while the other spectrometer measured the angular distribution.

To better understand the solid angle, new $\sim$1 and 2 msr collimators were fabricated and mounted on the front of the spectrometers. To better understand the integrated beam charge for the low currents needed for these experiments, the Hall A BCM electronics were upgraded, and a new beam calorimeter was installed in the beam line. Initial comparisons among the various BCM read-outs indicate the point-to-point variations in beam current are about 0.3%. Initial studies of the absolute current calibration using the beam calorimeter as a calorimeter, versus

as a Faraday cup, indicate that the absolute current calibration is better than 1%, down to a few tenths of 1 μA.

The initial analysis of the data is underway. Spectra from the 687 MeV run in late September look clean, but some spectra on solid targets at 362 MeV indicate that the beam might have been striking the aluminum target frames. At this point, no issues have arisen which would prevent us from reaching the experimental goal of measuring absolute cross sections to within 2-3% and point-to-point cross sections to better than 1% .

The goal of E05-103 was to survey the recoil proton polarization observables in deuteron photodisintegration for photon energies near 300 MeV. Modern theoretical models based on a description of the NN force and meson photoproduction, along with Δ degrees of freedom, meson-exchange currents, and relativistic corrections provide an excellent description of deuteron photodisintegration up to a few hundred MeV photon energy. The modern calculations include a series of technical advances over older calculations, such as a dynamical treatment of the pion, a nonperturbative treatment of the Δ, and mutual interaction in the πNN system. The most striking disagreement starts at about 300 MeV; the recoil proton induced polarization near $\theta_{cm} = 90°$ is predicted to go to 0 with increasing energy, but the data show that the polarization magnitude grows and reaches nearly -1 by 500 MeV. This large peak in the induced polarization has been known, but not explained, for 30 years.

Since the induced polarization data come from a variety of measurements from different labs, with different bins in energy and angle, and since the polarization transfers are unmeasured below $\sim$500 MeV, we proposed to survey the recoil polarizations to produce a systematic set of data, with the aim of providing clues as to what underlying dynamics are missing or poorly modeled in the calculations. The experiment covered an angle range θ_{cm} from 20° to 120°, generally in 10° steps, although certain intermediate angles were skipped. We mostly used two spectrometer momentum settings to cover a photon energy range of about 270 – 360 MeV at each angle; the lower energies were not measured at the largest angles.

Some preliminary polarization transfer data (P_x^c and P_z^c) and previous induced polarization data (P_y) are shown in Fig. 68. The calculations are from [125] (solid line) along with recent, unpublished improvements from [126] (dashed line). Here one sees that the calculations are in general agreement with the data, despite differences in the details. The technical improvements in the unpublished calculations generally appear to lead to a slightly worse agreement with the polarization transfer data. A similar effect has been seen in recent tensor polarization data in deuteron photodisintegration, from Novosibirsk [127]; here T_{20} and T_{22} are better described by the most recent calculations, while older calculations describe T_{21} better. It remains to be determined whether the differences are consistent with the theoretical uncertainties, or whether they are indicative of missing or poorly modeled underlying dynamics. The new induced polarization data are not shown, as they need a more careful treatment of false asymmetries than is available online.

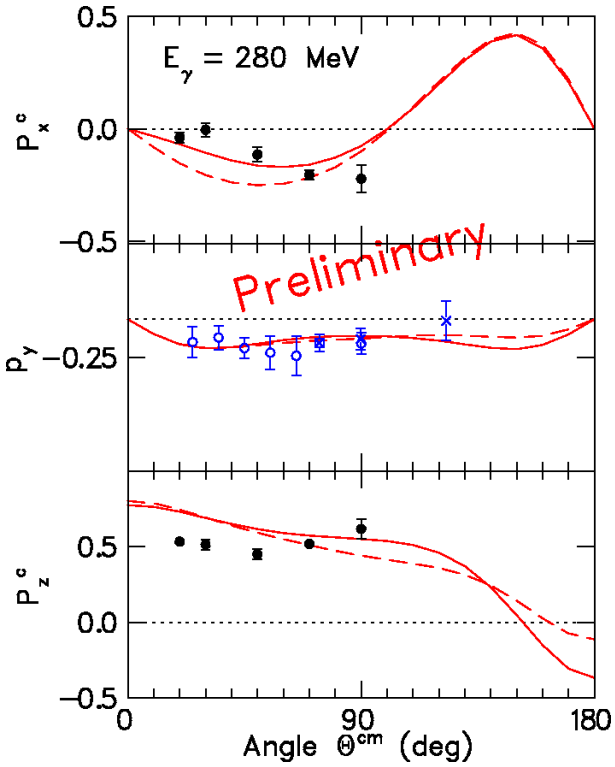

Figure 68: Angular distributions for recoil proton polarizations in deuteron photodisintegration, for $E_\gamma = 280 \pm 10$ MeV. See text for details.

4 References

[1] S. Nanda and D. Lhuillier, *Conceptual Design Report for Hall A Compton Polarimeter Upgrade*, unpublished.

[2] M. Bregant *et al.*, hep-ex/0202046, (2002).

[3] D. J. J. de Lange *et al.*, Nucl. Instrum. Methods A **406**, 182 (1998).

[4] M. W. Ahmed *et al.*, Nucl. Instrum. Methods A **469**, 95 (2000); L. Tang, private communication, 2004.

[5] C. Cuevas, W. Gunning, I. Rachek, and B. Wojtsekhowski, Low-noise amplifier-discriminator card for MWDC, 2005.

[6] M. Bevins *et al.*, *Absolute Current Calibration of 1 μA CW Electron Beam*, Proc. 7th European Workshop on Beam Diagnostics and Instrumentation for Particle Accelerators (DIPAC 2005), Lyon, France, 2005, p. 36, preprints LAB-ACP-05-388, DOE-ER-40150-3543.

[7] M. Bevins *et al.*, *Mechanical and thermal design of the CEBAF Hall A beam calorimeter*, Proc. Particle Accelerator Conference (PAC 05), Knoxville, Tennessee, 2005, p. 3819 (2005), preprint JLAB-ACE-05-327.

[8] M. Sotona and S. Frullani, Prog. Theor. Phys. Suppl. **117**, 151 (1994).

[9] J. C. David, C. Fayard, G.-H. Lamot and B. Saghai, Phys. Rev. C **53**, 2613 (1996); T. Mizutani, C. Fayard, G.-H. Lamot and B. Saghai, Phys. Rev. C **58**, 75 (1998).

[10] M. Ukai *et al.*, Phys. Rev. C **73**, 012501 (2006).

[11] O. Hashimoto and H. Tamura, Prog. Part. Nucl. Phys. **57**, 405 (2006).

[12] M. A. Shupe *et al.*, Phys. Rev. D **19**, 1929 (1979).

[13] A. S. Kronfeld and B. Nizic, Phys. Rev. D **44**, 3445 (1991).

[14] M. Vanderhaeghen, P. A. M. Guichon and J. Van de Wiele, Nucl. Phys. **A622**, c144 (1997).

[15] T. Brooks and L. Dixon, Phys. Rev. D **62** 114021 (2000).

[16] R. Thomson, Alex Pang and Cheng-Ryong Ji, Phys. Rev. D **73** 054023 (2006).

[17] A. V. Radyushkin, Phys. Rev. D **58**, 114008 (1998).

[18] M. Diehl, T. Feldmann, R. Jakob and P. Kroll, Eur. Phys. J. C **8**, 409 (1999).

[19] H. W. Huang, P. Kroll and T. Morii, Eur. Phys. J. C **23**, 301-310 (2002), *Erratum ibid.*, **31**, 279 (2003); H. W. Huang, private communication.

[20] J. Alcorn *et al.*, Nucl. Instrum. Methods A **522**, 294 (2004).

[21] J. L. Matthews and R. O. Owens, Nucl. Instrum. Methods **111**, 157 (1973).

[22] J. Arrington, http://www.jlab.org/∼johna/SIMC_documents/simc/ (unpublished).

[23] J. Arrington, Phys. Rev. C **69**, 022201(R) (2004).

[24] A. Danagoulian *et al.*, Nucl. Phys. **A755**, 281 (2005).

[25] V. M. Budnev *et al.*, Phys. Rep. **15C**, 181 (1975).

[26] M. Diehl *et al.*, Phys. Rev. D **67**, 037502 (2003).

[27] G. A. Miller, Phys. Rev. C **69**, 052201(R) (2004).

[28] D. J. Hamilton *et al.*, Phys. Rev. Lett. **94** 242001 (2005).

[29] A. Acha *et al.*, Phys. Rev. Lett. **98** 032301 (2007).
[30] R. D. McKeown, Phys. Lett. B **219** (1989) 140.
[31] E. J. Beise and R. D. McKeown, Comments Nucl. Part. Phys. **20** (1991) 105.
[32] D. H. Beck, Phys. Rev. D **39** (1989) 3248.
[33] K. S. Kumar and P. A. Souder, Prog. Part. Nucl. Phys. 45 (2000) S333.
[34] D. H. Beck and R. D. McKeown, Ann. Rev. Nucl. Part. Sci. 51 (2001) 189.
[35] D. H. Beck and B. R. Holstein, Int. J. Mod. Phys. E 10 (2000) 1.
[36] M. J. Musolf *et al.*, Phys. Rep. 239 (1994) 1.
[37] K. A. Aniol *et al.*, Phys. Rev. C **69**, 065501 (2004).
[38] K. A. Aniol *et al.*, Phys. Rev. Lett. **96**, 022003 (2006).
[39] K. A. Aniol *et al.*, Phys. Lett. B **635**, 275 (2006).
[40] R. Lewis, W. Wilcox and R. M. Woloshyn, Phys. Rev. D **67**, 013003 (2003).
[41] D. B. Leinweber *et al.*, Phys. Rev. Lett. **94**, 212001 (2005); D. B. Leinweber *et al.*, Phys. Rev. Lett. **97**, 022001 (2006).
[42] D. T. Spayde *et al.*, Phys. Lett. B **583**, 79 (2004).
[43] F. E. Maas *et al.*, Phys. Rev. Lett. **94**, 152001 (2005).
[44] D. S. Armstrong *et al.*, Phys. Rev. Lett. **95**, 092001 (2005).
[45] http://hallaweb.jlab.org/experiment/E05-007
[46] http://hallaweb.jlab.org/parity/prex
[47] K. Wijesooriya *et al.*, Phys. Rev. Lett. **86**, 2975 (2001).
[48] X. Jiang *et al.*, nucl-ex/0702002, submitted to Phys. Rev. Lett.
[49] V.P. Barannik *et al.*, Nucl. Phys. **A451**, 751 (1986).
[50] R. Gilman and Franz Gross, J. Phys. G **28**, R37, (2002).
[51] V.Yu Grishina *et al.*, Eur. Phys. J. A **18**, 207 (2003); V.Yu Grishina *et al.*, Eur. Phys. J. A **19**, 117 (2004).
[52] M.M. Sargsian, Phys. Lett. B **587**, 41 (2004).
[53] M. Mirazita *et al.*, Phys. Rev. C **70**,014005 (2004).
[54] S.J. Brodsky *et al.*, Phys. Lett. B **578**, 69 (2003); E. Piasetzky *et al.*, JLab experiment E03-101.
[55] W. Bertozzi, K. Fissum, A. Saha and L. Weinstein, spokespersons, JLab experiment E89-003.
[56] J. Gao *et al.*, Phys. Rev. Lett. **84**, 3265 (2000).
[57] N. Liyanage *et al.*, Phys. Rev. Lett. **86**, 5670 (2001).
[58] F. Garibaldi *et al.*, Nucl. Instrum. Methods A **314**, 1 (1992).
[59] E. Cisbani *et al.*, *A Waterfall Target System for Hall A at Jefferson Lab*, INFN/ISS **97/04** (1997).
[60] J. M. Udias *et al.*, Phys. Rev. Lett. **83**, 5451 (1999).
[61] J. M. Udias, private communication.
[62] John C. Collins and Andreas Freund, Phys. Rev. D **59**, 074009, (1999).
[63] Xiang-Dong Ji and Jonathan Osborne, Phys. Rev. D **58**, 094018 (1998).
[64] Xiang-Dong Ji, Phys. Rev. Lett. **78**, 610 (1997).
[65] Dieter Mueller *et al.*, Fortschr. Phys. 42, 101 (1994).
[66] A. V. Radyushkin, Phys. Rev. D **56**, 5524 (1997).

[67] Carlos Muñoz Camacho *et al.*, Phys. Rev. Lett. **97**, 262002 (2006).
[68] Alessandro Bacchetta, Umberto D'Alesio, Markus Diehl and C. Andy Miller, Phys. Rev. D **70**, 117504 (2004).
[69] Andrei V. Belitsky, Dieter Mueller and A. Kirchner, Nucl. Phys. **B629**, 323 (2002).
[70] M. Vanderhaeghen *et al.*, Phys. Rev. C **62**, 025501 (2000).
[71] M. Vanderhaeghen, P. A. M. Guichon and M. Guidal, Phys. Rev. D **60**, 094017 (1999).
[72] K. Goeke, Maxim V. Polyakov and M. Vanderhaeghen, Prog. Part. Nucl. Phys. **47**, 401 (2001).
[73] M. Guidal, M. V. Polyakov, A. V. Radyushkin and M. Vanderhaeghen, Phys. Rev. D **72**, 054013 (2005).
[74] Luke W. Mo and Yung-Su Tsai, Rev. Mod. Phys. 41, 205 (1969).
[75] I. V. Akushevich and N. M. Shumeiko, J. Phys. G 20, 513 (1994).
[76] M. Gluck, E. Reya, M. Stratmann and W. Vogelsang, Phys. Rev. D **63**, 094005 (2001).
[77] N. Bianchi, A. Fantoni and S. Liuti, Phys. Rev. D **69**, 014505 (2004).
[78] Aleksander V. Sidorov and Dimiter B. Stamenov, hep-ph/0604092 (2006).
[79] Claudio Ciofi degli Atti and S. Scopetta, Phys. Lett. B **404**, 223 (1997)
[80] J. L. Friar *et al.*, Phys. Rev. C **42**, 2310 (1990).
[81] T. Forest *et al.*, in preparation
[82] J. Blumlein and H. Bottcher, Nucl. Phys. **B636**, 225 (2002).
[83] Y. Gogo *et al.*, Phys. Rev. D **62**, 034017 (2000).
[84] M. K. Jones *et al.*, Phys. Rev. Lett. **84**, 1398 (2000).
[85] M. Diehl *et al.*, Eur. Phys. J. C 39, 1 (2005).
[86] B. Blankleider and R. M. Woloshyn, Phys. Rev. C **29**, 558 (1984+
[87] J. L. Friar *et al.*, Phys. Rev. C **42**, 2310 (1991).
[88] Ch. Hyde-Wright and K. de Jager, Ann. Rev. Nucl. Part. Sci. 54:217-267,2004.
[89] M. M. Sargsian *et al.*, Phys. Rev. C **71**, 044615 (2005).
[90] R. Niyazov and L. Weinstein, private communication, 2001.
[91] G. A. Miller, Phys. Rev. C **66**, 032201 (2002).
[92] A. Belitsky, X. Ji and F. Yuan, Phys. Rev. Lett. **91**, 092003 (2003).
[93] S. Strauch *et al.*, Phys. Rev. Lett. **91**, 052301 (2003).
[94] D. H. Lu *et al.*, Phys. Lett. B **417**, 217 (1998); Phys. Rev. C **60**, 068201 (1999).
[95] R. Schiavilla *et al.*, Phys. Rev. Lett. **94**, 072303 (2005).
[96] P. Lava, J. Ryckebusch, B. Van Overmeire and S. Strauch, Phys. Rev. C **71**, 014605 (2005).
[97] Jason R. Smith and Gerald A. Miller, Phys. Rev. C **70**, 065205 (2004).
[98] B. Milbrath *et al.*, Phys. Rev. Lett. **82**, 2221 (1999).
[99] O. Gayou *et al.*, Phys. Rev. C **64**, 038202 (2001).
[100] S. Dieterich *et al.*, Phys. Lett. B **500**, 47 (2001).
[101] S. Crawford *et al.*, Phys. Rev. Lett. **98** 052301 (2007).

[102]R. L. Cool *et al.*, Phys. Rev. Lett. **17**, 102 (1966).
[103]S. Mori *et al.*, Phys. Rev. **185**, 1687 (1969).
[104]T. G. Trippe *et al.*, (Particle Data Group), Rev. Mod. Phys. **48**, S1 (1976).
[105]T. Nakano *et al.*, (LEPS), Phys. Rev. Lett. **91**, 012002, (2003).
[106]K. H. Hicks, Prog. Part. Nucl. Phys. **55**, 647 (2005).
[107]V. D. Burkert, Int. J. Mod. Phys. A **21**, 1764 (2006)
[108]R. A. Schumacher, Proc. 17th Particles and Nuclei Conference (PANIC05), Santa Fe, 2005, AIP **842** 409 (2006); nucl-ex/0512042.
[109]D. Diakonov, V. Petrov and M. V. Polyakov, Z. Phys. **A359**, 305 (1997).
[110]R. L. Jaffe and F. Wilczek, Phys. Rev. Lett. **91**, 232003 (2003).
[111]S. Capstick, P. R. Page and W. Roberts, Phys. Lett. B **570**, 185 (2003).
[112]R. A. Arndt *et al.*, Phys. Rev. C **69**, 035208 (2004).
[113]Y. I. Azimov *et al.*, Eur. Phys. J. A **26**, 79 (2005).
[114]H. Kwee, M. Guidal, M. V. Polyakov and M. Vanderhaeghen, Phys. Rev. D **72**, 054012 (2005).
[115]V. Kubarovsky *et al.*, (CLAS), Phys. Rev. Lett. **97**, 102001 (2006).
[116]P. Brindza *et al.*, IEEE Trans. Appl. Superconductivity **11**, 1594 (2001).
[117]M. Iodice *et al.*, Nucl. Instrum. Methods A **553**, 231 (2005).
[118]J. D. Jackson, Nuovo Cim. **34**, 1644 (1964).
[119]W. M. Yao *et al.*, (Particle Data Group), J. Phys. G **33**, 1 (2006).
[120]G. J. Feldman and R. D. Cousins, Phys. Rev. D **57**, 3873 (1998).
[121]S. Baker and R. D. Cousins, Nucl. Instrum. Methods A **221**, 437 (1984).
[122]G. G. Simon *et al.*, Nucl. Phys. **A364**, 285 (1981).
[123]S. Platchkov *et al.*, Nucl. Phys. **A510**, 740 (1990).
[124]J. Calarco, private communication.
[125]M. Schwamb and H. Arenhövel, Mod. Phys. Lett. A **18**, 190 (2003); M. Schwamb and H. Arenhövel, Nucl. Phys. **A696**, 556 (2001); and M. Schwamb and H. Arenhövel, Nucl. Phys. **A690**, 682 (2001).
[126]M. Schwamb, Habilitation thesis, Johannes Gutenberg-Universität Mainz, 2006.
[127]I. Rachek *et al.*, submitted to Phys. Rev. Lett. , nucl-ex/0611030.

5 Hall A Collaboration Member List

Armando Acha	*Florida International University*
Kalyan Allada	*University of Kentucky*
Bryon Anderson	*Kent State University*
Mattias Andersson	*University of Lund*
Konrad A. Aniol	*California State University*
John Annand	*University of Glasgow*
David S. Armstrong	*College of William and Mary*
John Arrington	*Argonne National Laboratory*
Todd Averett	*College of William and Mary*
Elizabeth Beise	*University of Maryland*
Hachemi Benaoum	*Syracuse University*
Fatiha Benmokhtar	*University of Maryland*
Jacques Berthot	*Laboratoire de Physique Corpusculaire, Clermont-Ferrand*
Pierre Bertin	*Laboratoire de Physique Corpusculaire, Clermont-Ferrand*
Bill Bertozzi	*Massachusetts Institute of Technology*
Louis Bimbot	*Institut de Physique Nucléaire, Orsay*
Werner Boeglin	*Florida International University*
Alexander Borissov	*University of Glasgow*
Ed Brash	*University of Regina*
Vincent Breton	*Laboratoire de Physique Corpusculaire, Clermont-Ferrand*
Herbert Breuer	*University of Maryland*
Etienne Burtin	*DAPNIA/SPhN, CEA, Saclay*
John Calarco	*University of New Hampshire*
Alexandre Camsonne	*Jefferson Laboratory*
Larry Cardman	*Jefferson Laboratory*
Gordon D. Cates	*University of Virginia*
Christian Cavata	*DAPNIA/SPhN, CEA, Saclay*
George Chang	*University of Maryland*
Nicholas Chant	*University of Maryland*
Jian-Ping Chen	*Jefferson Laboratory*
Seonho Choi	*Seoul National University, Korea*
Eugene Chudakov	*Jefferson Laboratory*
Evaristo Cisbani	*INFN/Sezione Sanità*
Leon Cole	*Hampton University*
Luminita Coman	*Florida International University*
Marius Coman	*Florida International University*
Brandon Craver	*University of Virginia*
Benjamin Crowe	*North Carolina Central University*
Francesco Cusanno	*INFN/Sezione Sanità*

Dan Dale	*University of Kentucky*
Areg Danagoulian	*University of Illinois*
Nathalie Degrande	*Ghent State University*
Raffaele De Leo	*INFN/Sezione Bari*
Alexandre Deur	*Jefferson Lab*
Nicole d'Hose	*DAPNIA/SPhN, CEA, Saclay*
Rachele di Salvo	*INFN/Sezione Roma2*
Pibero Djawotho	*College of William and Mary*
Frank Dohrmann	*Argonne National Laboratory*
Jean-Eric Ducret	*DAPNIA/SPhN, CEA, Saclay*
Chiranjib Dutta	*University of Kentucky*
Dipangkar Dutta	*Duke University/TUNL*
Kim Egiyan	*Yerevan Physics Institute*
Martin B. Epstein	*California State University*
Stephanie Escoffier	*DAPNIA/SPhN, CEA, Saclay*
Catherine Ferdi	*Laboratoire de Physique Corpusculaire, Clermont Ferrand*
Robert Feuerbach	*Jefferson Lab*
Mike Finn	*College of William and Mary*
Kevin Fissum	*University of Lund*
Helene Fonvieille	*Laboratoire de Physique Corpusculaire, Clermont-Ferrand*
Bernard Frois	*DAPNIA/SPhN, CEA, Saclay*
Salvatore Frullani	*INFN/Sezione Sanità*
Haiyan Gao	*Duke University*
Franco Garibaldi	*INFN/Sezione Sanità*
David Gaskell	*Jefferson Laboratory*
Ashot Gasparian	*Hampton University*
Gagik Gavalian	*Old Dominion University*
Olivier Gayou	*Massachusetts Institute of Technology*
Shalev Gilad	*Massachusetts Institute of Technology*
Ron Gilman	*Rutgers, The State University of New Jersey*
Alexander Glamazdin	*Kharkov Institute of Physics and Technology*
Charles Glashausser	*Rutgers, The State University of New Jersey*
Jackie Glister	*Saint Mary's University*
Javier Gomez	*Jefferson Laboratory*
Victor Gorbenko	*Kharkov Institute of Physics and Technology*
Tim Gorringe	*University of Kentucky*
Jacqueline Glister	*Saint Mary's University*
Keith Griffioen	*College of William and Mary*
David Hamilton	*University of Glasgow*
Ole Hansen	*Jefferson Laboratory*
David Hayes	*Old Dominion University*

Mitra Hashemi Shabestari	*University of Virginia*
Joaquin Herraiz	*Universidad Complutense, Madrid*
Bill Hersman	*University of New Hampshire*
Doug Higinbotham	*Jefferson Laboratory*
Wendy Hinton	*Old Dominion University*
Richard Holmes	*Syracuse University*
Harry Holmgren	*University of Maryland*
Tim Holmstrom	*College of William and Mary*
Maurik Holtrop	*University of New Hampshire*
Tanja Horn	*Jefferson Laboratory*
Edik Hovhannisyan	*Yerevan Physics Institute*
Calvin Howell	*Duke University*
Garth Huber	*University of Regina*
Charles Hyde-Wright	*Old Dominion University*
Hassan Ibrahim	*Old Dominion University*
Ru Igarashi	*University of Saskatchewan*
Mauro Iodice	*INFN/Sezione Sanità*
Riccardo Iommi	*INFN/Sezione Sanità*
Dave Ireland	*University of Glasgow*
Kees de Jager	*Jefferson Laboratory*
Stephanie Jaminion	*Laboratoire de Physique Corpusculaire, Clermont-Ferrand*
Yi Jiang	*University of Science and Technology of China (USTC)*
Xiaodong Jiang	*Rutgers, The State University of New Jersey*
Mark K. Jones	*Jefferson Laboratory*
Seigo Kato	*Yamagata University*
Mina Katramatou	*Kent State University*
Lisa Kaufman	*University of Massachusetts*
James Kellie	*University of Glasgow*
James Kelly	*University of Maryland*
Sophie Kerhoas	*DAPNIA/SPhN, CEA, Saclay*
Armen Ketikyan	*Yerevan Physics Institute*
Kouichi Kino	*Tohoku University*
Norm Kolb	*University of Saskatchewan*
Ameya Kolarkar	*University of Kentucky*
Wolfgang Korsch	*University of Kentucky*
Serge Kox	*Laboratoire de Physique Subatomique et de Cosmologie, Grenoble*
Alexander Kozlov	*University of Regina*
Kevin Kramer	*College of William and Mary*
Laird Kramer	*Florida International University*
Elena Khrosinkova	*Kent State University*

Elena Kuchina	*Rutgers, The State University of New Jersey*
Krishna S. Kumar	*University of Massachusetts*
Gerfried Kumbartzki	*Rutgers, The State University of New Jersey*
Geraud Lavessiere	*Laboratoire de Physique Corpusculaire, Clermont-Ferrand*
Byungwuek Lee	*Seoul National University*
John LeRose	*Jefferson Laboratory*
Mark Leuschner	*University of New Hampshire*
David Lhuillier	*DAPNIA/SPhN, CEA, Saclay*
Richard Lindgren	*University of Virginia*
Ken Livingston	*University of Glasgow*
Nilanga Liyanage	*University of Virginia*
George Lolos	*University of Regina*
Robert Lourie	*Renaissance Technology*
Hai-jiang Lu	*University of Science and Technology of China (USTC)*
Richard Madey	*Kent State University*
Kazushige Maeda	*Tohoku University*
Vahe Mamyan	*Yerevan Physics Institute*
Mark Manley	*Kent State University*
Demetrius Margaziotis	*California State University*
Pete Markowitz	*Florida International University*
Jacques Marroncle	*DAPNIA/SPhN, CEA, Saclay*
Jacques Martino	*SUBATECH, IN2P3, Nantes*
Samvel Mayilyan	*Yerevan Physics Institute*
Malek Mazouz	*Faculté des Sciences de Monastir, Tunisia*
Kathy McCormick	*Pacific Northwest National Lab*
David Meekins	*Jefferson Laboratory*
Zein-Eddine Meziani	*Temple University*
Robert Michaels	*Jefferson Laboratory*
Bernard Michel	*Université Blaise Pascal, Clermont-Ferrand*
Wilson Miller	*University of Virginia*
Joseph Mitchell	*Renaissance Technology*
Bryan Moffit	*Massachusetts Institute of Technology*
Peter Monaghan	*Massachusetts Institute of Technology*
Jean Mougey	*Laboratoire de Physique Subatomique et de Cosmologie, Grenoble*
Pierre Moussiegt	*Laboratoire de Physique Subatomique et de Cosmologie, Grenoble*
Carlos Munoz-Camacho	*DAPNIA/SPhN, CEA, Saclay*
Sirish Nanda	*Jefferson Laboratory*
Alan Nathan	*University of Illinois*
Vladimir Nelyubin	*St. Petersburg Nuclear Physics Institute*
Damien Neyret	*DAPNIA/SPhN, CEA, Saclay*
Dima Nikolenko	*Budker Institute of Nuclear Physics*
Blaine Norum	*University of Virginia*

Michael Olson	*St. Norber College*
Zisis Papandreou	*University of Regina*
Kent Paschke	*University of Virginia*
Jen-Chieh Peng	*University of Illinois*
Lubomir Penchev	*College of William and Mary*
Charles Perdrisat	*College of William and Mary*
Cristina Perez	*Universidad Complutense, Madrid*
Gerassimos G. Petratos	*Kent State University*
Artush Petrosyan	*Yerevan Physics Institute*
Eli Piasezky	*Tel Aviv University*
Stephane Platchkov	*DAPNIA/SPhN, CEA, Saclay*
Roman Pomatsalyuk	*Kharkov Institute of Physics and Technology*
Ishay Pomerantz	*Tel Aviv University*
Luis Prieto	*Universidad Complutense, Madrid*
Dan Protopopescu	*University of Glasgow*
Andrew Pucket	*Massachusetts Institute of Technology*
Vina Punjabi	*Norfolk State University*
Thierry Pussieux	*DAPNIA/SPhN, CEA, Saclay*
Issam Qattan	*North-Western University*
Xin Qian	*Duke University*
Yi Qiang	*Massachusetts Institute of Technology*
Gilles Quéméner	*Laboratoire de Physique Subatomique et de Cosmologie, Grenoble*
Igor Rachek	*Budker Institute of Nuclear Physics*
Cesar Raminez	*Universidad Complutense, Madrid*
Ronald Ransome	*Rutgers, The State University of New Jersey*
Brian Raue	*Florida International University*
Juerg Reinhold	*Florida International University*
Bodo Reitz	*Jefferson Laboratory*
Yves Roblin	*Jefferson Laboratory*
Rikki Roché	*Old Dominion University*
Mike Roedelbronn	*University of Illinois*
Guy Ron	*Tel Aviv University*
Oscar Rondon	*University of Virginia*
Guenther Rosner	*University of Glasgow*
Gary Rutledge	*TRIUMF*
Marat Rvachev	*Massachusetts Institute of Technology*
Franck Sabatie	*DAPNIA/SPhN, CEA, Saclay*
Arun Saha	*Jefferson Laboratory*
Teijiro Saito	*Tohoku University*
Adam J. Sarty	*Saint Mary's University*
Brad Sawatsky	*Temple University*
Ralph Segel	*Northwestern University*

Andrei Semenov	*Kent State University*
Albert Shahinyan	*Yerevan Physics Institute*
Ran Sheyor	*Tel Aviv University*
Simon Sirca	*Massachusetts Institute of Technology*
Karl Slifer	*University of Virginia*
Timothy Smith	*University of New Hampshire*
Patricia Solvignon	*Temple University*
Pavel Sorokin	*Kharkov State University*
Paul A. Souder	*Syracuse University*
Steffen Strauch	*University of South Carolina*
Ramesh Subedi	*Kent State University*
Riad Suleiman	*Massachusetts Institute of Technology*
Vincent Sulkovsky	*College of William and Mary*
Jeff Templon	*NIKHEF*
Tatsuo Terasawa	*Tohoku University*
Neil Thompson	*University of Glasgow*
H. Tsubota	*Tohoku University*
Jose Udias Moinelo	*Universidad Complutense, Madrid*
Hiroaki Ueno	*Yamagata University*
Paul E. Ulmer	*Old Dominion University*
Guido Urciuoli	*INFN/Sezione Sanità*
Antonin Vacheret	*DAPNIA/SPhN, CEA, Saclay*
Luc Van de Hoorebeke	*Ghent State University*
Robert Van de Vyver	*Ghent State University*
Pascal Vernin	*DAPNIA/SPhN, CEA, Saclay*
Javier Vignote	*Laboratoire de Physique Subatomique et de Cosmologie, Grenoble*
Branislav Vlahovic	*North Carolina Central University*
Hakob Voskanyan	*Yerevan Physics Institute*
Eric Voutier	*Laboratoire de Physique Subatomique et de Cosmologie, Grenoble*
Richard Walter	*Duke University*
Kebin Wang	*University of Virginia*
John Watson	*Kent State University*
Dan Watts	*University of Glasgow*
Larry Weinstein	*Old Dominion University*
Richard Wilson	*Harvard University*
Bogdan Wojtsekhowski	*Jefferson Laboratory*
Huan Yao	*Temple University*
Yunxiu Ye	*University of Science and Technology of China (USTC)*
Xiaohui Zhan	*Massachusetts Institute of Technology*

Xiaochao Zheng	*University of Virginia*
Shuhua Zhou	*China Institute of Atomic Energy (CIAE)*
Lingyan Zhu	*University of Illinois*
Xiaofeng Zhu	*Duke University*

6 Publications

- "*Polarization transfer in the* $^2H(e,e'p)n$ *reaction up to* $Q^2 = 1.61\ GeV^2$," B. Hu *et al.*, Phys. Rev. C **73**, 064004 (2006).
- "*Constraints on the nucleon strange form factors at* $Q^2 \sim 0.1\ GeV^2$," K. A. Aniol *et al.*, Phys. Lett. B **635**, 275 (2006).
- "*Parity-Violating electron scattering from* ^4He *and the strange electric form factor of the nucleon*," K. A. Aniol *et al.*, Phys. Rev. Lett. **96**, 022003 (2006).
- "*A Search for* Σ_5^0, N_5^0 *and* Θ^{++} *Pentaquark States*," Y. Qiang *et al.*, submitted to Phys. Rev. D.
- "*Precise Extraction of the Neutron Magnetic Form Factor from Quasi-elastic* $^3\vec{H}e(\vec{e},e')$ *at* $Q^2 = 0.1$–$0.6\ (GeV/c)^2$," B. Anderson *et al.*, nucl-ex/0605006, Accepted for publication in Phys. Rev. C.
- "*Precision Measurements of the Nucleon Strange Form Factors at* $Q^2 \sim 0.1\ GeV^2$," A. Acha *et al.*, Phys. Rev. Lett. **98**, 032301 (2007).
- "*Scaling Tests of the Cross Section for Deeply Virtual Compton Scattering*," C. Munoz Camacho *et al.*, Phys. Rev. Lett. **97**, 262002 (2006).

7 Theses

i. "*Measurements of Compton Scattering on the proton at 2 – 6 GeV*"
Areg Danagoulian, University of Illinois at Urbana-Champaign, March, 2006.

ii. "*Measurement of the* ^{3}*He Spin Structure Functions in the Resonance Region: A Test of Quark-Hadron Duality on the Neutron*"
Patricia Solvignon, Temple University, Aug. 2006.

iii. "*Elastic Scattering of Longitudinally Polarized Electrons From* ^{4}*He: A Measurement of* G_E^s *at* $Q^2 = 0.1\ GeV^2$"
Bryan Moffit, College of William and Mary, Oct. 2006.

iv. "*Extrapolation de la diffusion Compton profondement virtuelle sur le neutron dans le Hall A au Jefferson Laboratory*"
Malek Mazouz, Doctorat Thesis, Joseph Fourier University, Grenoble, Dec. 2006.

v. "*Precision Measurement of the Proton Neutral Weak Form Factors at* $Q^2 = 0.1\ GeV^2$"
Lisa Kaufman, University of Massachusetts, Dec. 2006.

vi. "*The* $^2H(e, e'p)n$ *reaction at high four-momentum transfer*"
Hassan Ibrahim, Old Dominion University, Dec. 2006.